

DISSERTATION

Characterization of a planetary  
system PTFO 8-8695 from the  
variability of its transit lightcurve  
induced by the nodal precession

主星-惑星歳差運動による  
トランジット光度曲線の時間変動を用いた  
系外惑星系PTFO 8-8695の  
パラメータ推定

Shoya Kamiaka

A thesis submitted to  
the graduate school of science,  
the University of Tokyo  
in partial fulfillment of  
the requirements for the degree  
of Master of Science in Physics

January, 2015



# Abstract

Since the first discovery of an exoplanet, a planet orbiting around a star other than the Sun, in 1995, a large number of exoplanets were detected with the dramatic development of the observational instruments. As of January 2015, the number of confirmed exoplanets is close to 2000, which have revealed the diversity of the architecture of the exoplanetary systems beyond our conventional perspective on the planetary systems. Some of them were found to harbour a gas giant planet at the vicinity of the central star (close-in planet), which configuration is totally different from that of the solar system. For the better understanding on the planet formation scenario, therefore, the characterization of these exoplanets is an important issue.

Transit is one of the most powerful methods to detect the exoplanets where the exoplanetary occultation in front of the stellar disk is detected as the reduction of the stellar flux. The extent of such reduction directly reflects the size ratio of the planet to the star, thus one can characterize the radius of the transiting planet.

PTFO 8-8695 is a transiting planetary system consisting of a pre-main-sequence star and a close-in planet. It shows unexpected shapes and variability of the transit light curves in 2009 and 2010 observations. One of the remarkable features of PTFO 8-8695 is that the rapid rotation of the central star causes it to be rotationally deformed, resulting in the dimmer equatorial region compared to the brighter polar regions (gravity darkening). Another feature is that the strong torque between the star and planet triggers the spin-orbit nodal precession, where the stellar spin and planetary orbital axes mutually precess around the total angular momentum vector. The observed features of the transit light curves in PTFO 8-8695 system can be attributed to these features; nodal precession accompanied by the gravity darkening. Since the stellar spin and planetary orbit change their directions in the sky plane with time, planet gets into the stellar disk with non-uniform brightness from various directions with time, leading to the unusual shapes and variability of the transit light curves.

The previous work on the characterization of this system estimated not only the planetary radius but also the planetary mass through the sensitivity of the precession state on the planetary mass. In that work, they assumed that the stellar spin period is synchronized to the planetary orbital period, which is unlikely to be achieved in PTFO 8-8695 system. This is why we re-analyzed this system without the spin-orbit synchronous condition. Indeed we found that a variety of the parameter sets are possible as the solutions to the current data. In order to distinguish them, we present the future prediction of the transit light curves for several solution candidates. We are now collaborating with

the researches in Kyoto Sangyo University (KSU), and they are performing an additional observation of PTFO 8-8695 from 2014 November and 2015 January during which the difference of the predicted light curves for possible solutions are large enough to be detectable with the Araki-telescope in KSU.

In addition to above achievement, we also formulated the general equations for the dynamical evolution of the system. Our equations can take into account the planetary spin effect and pursue the secular tidal evolution of the system, both of which the simpler equations in the previous work cannot cover. We showed that the effect of the planetary spin potentially alters the precession architecture of the system with this model. Serious investigation of this effect may make it possible to detect the planetary spin from the future observations. Moreover, we suggested that tidal evolution by assuming the standard stellar properties is inconsistent with the current configuration of PTFO 8-8695 system. This inconsistency between the theoretical prediction and observational picture provides the clue to assess the internal profiles of the pre-main-sequence stars.

# Contents

|   |           |
|---|-----------|
| <b>Chapter 1. Introduction</b>  | <b>1</b>  |
| <b>Chapter 2. Background and Motivations</b>  | <b>5</b>  |
| 2.1 Overview of a planetary system PTFO 8-8695 . . . . .  | 5         |
| 2.2 Gravity darkening effect and the nodal precession . . . . .                                 | 8         |
| 2.3 Strategy in Barnes et al. (2013) . . . . .  | 12        |
| 2.3.1 Individual fittings . . . . .   | 12        |
| 2.3.2 Extrapolation of the individual fittings . . . . .  | 17        |
| 2.3.3 Joint fittings . . . . .  | 19        |
| 2.4 Validity of the spin-orbit synchronous condition in Barnes et al. (2013) . .                | 22        |
| <b>Chapter 3. Basic Equations for the Star-Planet Nodal Precession</b>                          | <b>27</b> |
| 3.1 Lagrange’s planetary equations for the analytic formulae of the nodal precession . . . . .  | 27        |
| 3.2 Analytic expressions for the gravitational coefficients with core-mantle model              | 30        |
| 3.3 From single precession to mutual precession . . . . .                                       | 32        |
| 3.4 Relation of the angular momentum vectors in the invariant frame and the sky frame . . . . . | 33        |
| <b>Chapter 4. Light Curve modelling</b>   | <b>37</b> |
| 4.1 General formula for the normalized flux . . . . .   | 37        |
| 4.2 Effective oblateness $f_{\text{eff}}$ . . . . .   | 38        |
| 4.3 Flux from the oblate star . . . . .   | 40        |
| 4.4 Stellar intensity $I_{\lambda}(r', \theta')$ . . . . .                                      | 40        |
| 4.5 Effective temperature $T_{\text{eff}}(r', \theta')$ . . . . .                               | 42        |
| <b>Chapter 5. Results and Discussion</b>  | <b>43</b> |
| 5.1 Data reduction . . . . .  | 43        |
| 5.2 Individual fittings . . . . .   | 46        |
| 5.3 Extrapolation of the individual fittings . . . . .  | 47        |
| 5.4 Joint fittings with the synchronous condition . . . . .                                     | 47        |
| 5.4.1 $M_{\star} = 0.34M_{\odot}$ case . . . . .  | 49        |
| 5.4.2 $M_{\star} = 0.44M_{\odot}$ case . . . . .  | 50        |
| 5.5 Data analysis without the synchronous condition . . . . .                                   | 52        |

|  |  |           |
|--|--|-----------|
| 5.5.1  | Individual fittings . . . . .  | 52        |
| 5.5.2  | Joint fittings for $M_{\star} = 0.34M_{\odot}$ case . . . . .                | 54        |
| 5.5.3  | Joint fittings for $M_{\star} = 0.44M_{\odot}$ case . . . . .                | 55        |
| 5.6  | Discussion . . . . .   | 56        |
| 5.6.1  | Re-analysis of the current data without phase-fold . . . . .                 | 56        |
| 5.6.2  | Future prediction to distinguish the possible solutions . . . . .            | 59        |
| 5.6.3  | The possibility for the detection of the planetary spin . . . . .            | 63        |
| 5.6.4  | Tidal evolution of PTFO 8-8695 system . . . . .                              | 65        |
| <b>Chapter 6. Summary and Future Prospects</b> |  | <b>67</b> |
| <b>Acknowledgments</b>                         |  | <b>71</b> |
| <b>Appendix A. Planet Formation Theory</b>     |  | <b>73</b> |
| Appendix A.1                                   |  |           |
|  | Conventional theory . . . . .  | 73        |
| Appendix A.2                                   |  |           |
|  | Spin-orbit angle distribution and its implication to planet formation theory | 74        |
| <b>Appendix B. Keplerian Motion</b>            |  | <b>79</b> |
| Appendix B.1                                   |  |           |
|  | Planetary position and velocity in terms of true anomaly . . . . .           | 79        |
| Appendix B.2                                   |  |           |
|  | Planetary position in terms of time . . . . .                                | 83        |
| Appendix B.3                                   |  |           |
|  | Three dimensional representation of the planetary orbit . . . . .            | 84        |
| <b>Appendix C. Transits</b>                    |  | <b>87</b> |
| Appendix C.1                                   |  |           |
|  | General theory . . . . .   | 87        |
| Appendix C.1.1                                 |  |           |
|  | Geometry of the transits . . . . .   | 87        |
| Appendix C.1.2                                 |  |           |
|  | Phases of the transits . . . . .   | 88        |
| Appendix C.2                                   |  |           |
|  | Supplements to the light curve modelling . . . . .                           | 89        |
| Appendix C.2.1                                 |  |           |
|  | Integration scheme of $F_{\text{blocked}}(t)$ . . . . .                      | 89        |
| Appendix C.2.2                                 |  |           |
|  | Consistency relation for $T_{\text{pol}}$ . . . . .                          | 92        |
| Appendix C.2.3                                 |  |           |
|  | Absolute dimension of the system . . . . .                                   | 93        |

---

|   |           |
|---|-----------|
| <b>Appendix D. General Formulation of Equations of Motion</b>                     | <b>95</b> |
| Appendix D.1  |           |
| Gravitational potential energy . . . . .  | 95        |
| Appendix D.1.1  |           |
| Centrifugal forces . . . . .  | 95        |
| Appendix D.1.2  |           |
| Gravitational potential outside of the rotating body . . . . .                    | 95        |
| Appendix D.1.3  |           |
| Gravitational potential energy in the oblate star-planet system . . . . .         | 99        |
| Appendix D.2  |           |
| Hamiltonian and equations of motion for the spin-orbit nodal precession . . . . . | 102       |
| Appendix D.2.1  |           |
| Equations of motion in the oblate star-planet system . . . . .                    | 102       |
| Appendix D.2.2  |           |
| Laplace-Runge-Lenz vector . . . . .   | 103       |
| Appendix D.2.3  |           |
| Equations of motion after orbital averaging . . . . .                             | 103       |
| Appendix D.3  |           |
| Equilibrium tidal theory and equations of motion . . . . .                        | 104       |
| Appendix D.3.1  |           |
| Equilibrium tidal potential . . . . .   | 104       |
| Appendix D.3.2  |           |
| Equations of motion for the tidal evolution . . . . .                             | 105       |
| Appendix D.4  |           |
| From angular momentum vectors to rotational/orbital parameters . . . . .          | 106       |



# Chapter 1

## Introduction

The last twenty years since the first detection of an extrasolar planet (hereafter, exoplanet) by Mayor & Queloz (1995) were the particularly dramatic age among the long history of the astronomy lasting from the prehistoric ages of human beings. This is because the architectures of exoplanetary systems revealed by their and following works are found to be totally different from the configuration of our solar system. Since until that discovery the planet formation theory is established for the purpose of explaining the formation of our solar system alone, the unexpected properties of observed exoplanets completely altered our perspective on the planetary system. Based on the recent observations suggesting that our solar system might not show the common architecture of the planetary systems, the conventional theory of planet formation (known as the Hayashi model; see Appendix A) now needs to be improved so as to explain the observed diversity of exoplanets.

The specific features of the observed exoplanets are briefly introduced as follows. For example, the first detected exoplanet, 51 Pegasi b, orbits around the G dwarf similar to the Sun but has substantially large mass ( $>0.472M_{\text{Jupiter}}$ ) for its extreme short orbital semi-major axis (smaller than that of Mercury). This kind of planets with Jupiter-like mass at the vicinity of the central star is now called “hot Jupiter”. As more exoplanets were detected, other features of the planetary systems has become apparent (see Howard 2013 for introduction of the observed properties of exoplanets). Specifically, non-negligible portion of them are found to be hot Jupiters (top-left region in the left panel in Figure 1.1), hot Neptunes or super Earths (bottom-left region in the left panel in Figure 1.1), all of which are with significantly small semi-major axes ( $< \sim 0.1AU$ ). In addition, it is surprising that some exoplanets have the substantially eccentric orbits whose eccentricities are over 0.5 (Marcy & Butler 1996, Cochran et al. 1997) or even approaching unity (right panel in Figure 1.1). Furthermore, it is also worth emphasising that some exoplanets show highly inclined orbits with respect to the equatorial planes of their central stars, some of which have even retrograde orbits (Anderson et al. 2010, Winn et al. 2009 and Narita et al. 2009). Such unusual properties are beyond the scope of the conventional planet formation theory which predicts the circular and coplanar planetary systems with gas giants located at the outer orbits as that of Jupiter. In response to these unexpected discoveries, the statistical discussion and characterization of a variety of exoplanets are now required for the improvement of the conventional theory of the planet formation.

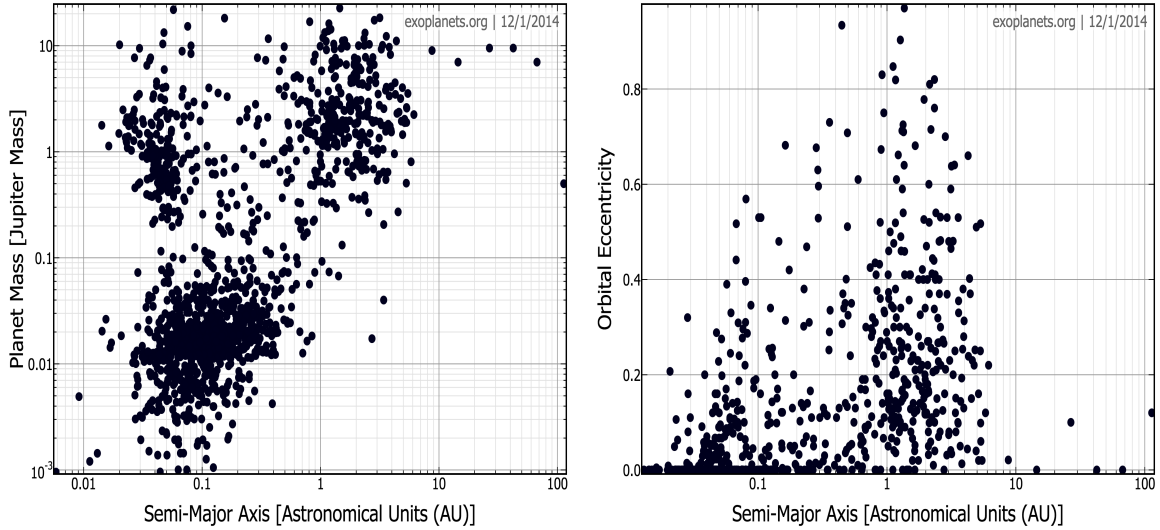


Figure 1.1: Mass (left) or orbital eccentricity (right) vs semi-major axis of exoplanets. Both figures taken from Exoplanet Orbit Database - Exoplanet Data Explorer <http://exoplanets.org/>.

Since the first detection, more and more exoplanets has been discovered, approaching 2000 in number for confirmed planets alone and 5000 for planet candidates (Figure 1.2). Among the various methods for the planet detection, the transit method is successful in discovering larger number of exoplanets than any other methods (Figure 1.2). This method makes use of the reduction of the flux from the star induced by the exoplanetary eclipse (see Appendix C for details), and directly provides the information on the size of transiting planets. Although there is a limitation that the planetary eclipse takes place only when the planetary system is seen from edge-on, the transit method is one of the most powerful ways for the detection of exoplanets. The spectroscopic radial velocity (RV) method is another powerful method for the planet detection. This method detects the reflex motion of the central star induced by the orbital motion of the exoplanet as the periodic Doppler shift of the stellar spectra. The amplitude of the Doppler shift depends on the planetary mass, which makes it possible to estimate the planetary mass through the analysis of the spectroscopic data.

In this thesis, we attempted the characterization of the planetary system PTFO 8-8695 through the analysis its transit light curves. The photometric transit observation for this system was performed in Palomar Observatory in 2009 and 2010 (van Eyken et al. 2012). By analyzing the observed transit light curves, Barnes et al. (2013) (hereafter, B13) estimated the system parameters such as the planetary mass, planetary radius and spin-orbit angle (the angle between the stellar spin axis and planetary orbital axis, and denoted as  $\phi$ ; see Appendix A for details). Again transit light curves does not provide the information on the planetary mass. Thereby, it is in general necessary for the estimation of the planetary mass to make use of the spectroscopic RV data. In the case of PTFO 8-8695, however, the variability of the transit light curve induced by the precession of the

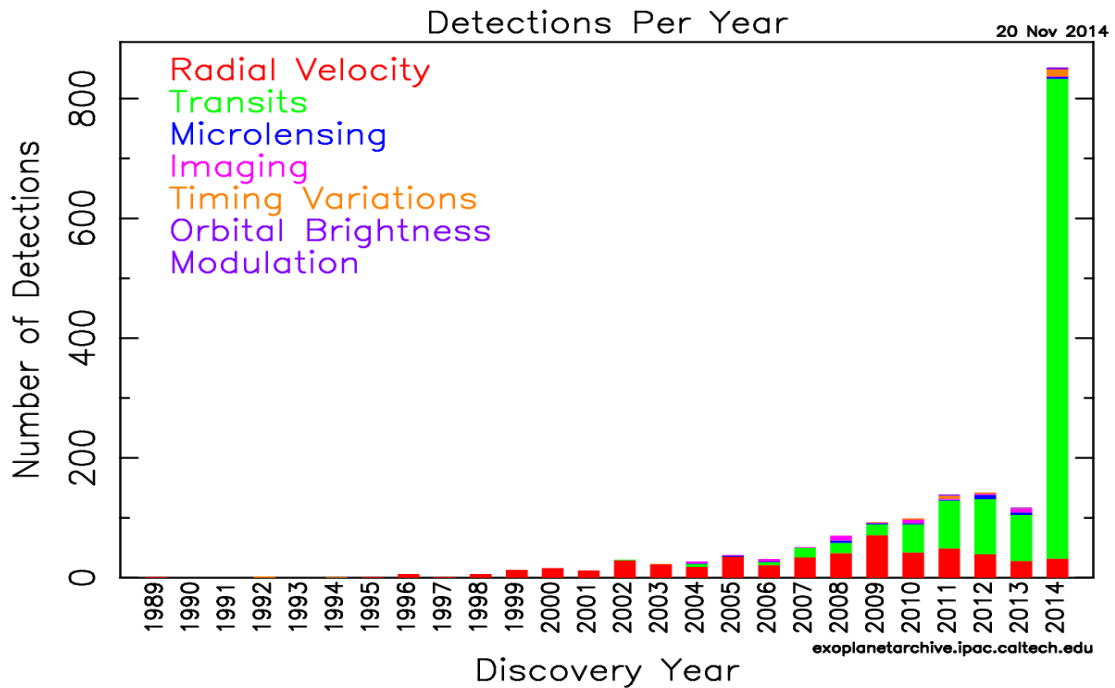


Figure 1.2: Number of exoplanets discovered each year. Different colors show the different detection methods. Figure taken from NASA Exoplanet Archive <http://exoplanetarchive.ipac.caltech.edu/index.html>.

stellar spin axis and planetary orbital axis makes it possible to estimate the planetary mass with the data of transit observation alone. This work is basically the reproduction of the achievements by B13. However, we re-analyzed PTFO 8-8695 system without the unphysical assumption employed in B13 and presents the future prediction of the transit light curves for the preparations of the future observations, both of which are the original points of this work. Since it is still possible that an exoplanet in PTFO 8-8695 system is false positive, to say further, the future observations guided by our prediction of the light curves do serve as the key to make a decisive judgement to this exoplanetary candidate. All observational data used in this thesis was provided by courtesy of Prof. Julian van Eyken, the main author of van Eyken et al. (2012).

The structure of this thesis is as follows. In chapter 2, we describe the planetary system PTFO 8-8695 consisting of T-Tauri star and one close-in planet by referring to the works devoted to the discovery (van Eyken et al. 2012) and analysis (Barnes et al. 2013, hereafter, B13) of this exoplanet. The mathematical formulation of the nodal precession of the system follows the way described in chapter 3. And then, the light curve modelling procedure with the formulae in chapter 3 is introduced in chapter 4. Based on the theoretical models in chapters 3 and 4, all results given by this work are summarized in chapter 5, supplemented with the future prediction of the transit light curves in order to see the accessibility of the future observations. Finally, chapter 6 summarizes the achievements in this work, and presents the future prospects for which this work can

serve as the groundwork.

# Chapter 2

## Background and Motivations

This chapter is the review part of an exoplanetary system PTFO 8-8695. We describe the achievements of the previous works on this system basically following van Eyken et al. (2012) (discovery of this exoplanetary candidate) and B13 (characterization of this exoplanetary system).

### 2.1 Overview of a planetary system PTFO 8-8695

PTFO 8-8695 is a pre-main-sequence star (weak-line T-Tauri star) at the Orion OB1a star forming region reported by Briceño et al. (2005). PTFO 8-8695 stellar properties are summarised in Table 2.1 (see van Eyken et al. 2012 for details). The stellar mass of  $0.44M_{\odot}$  and stellar age of 2.63 Myr are derived with the stellar model by Baraffe et al. (1998), while  $0.34M_{\odot}$  and 2.68 Myr are with the model by Siess et al. (2000).

Table 2.1: PTFO 8-8695 stellar properties

| Property                 | Value   |
|--------------------------|---|
| Alternative designations | CVSO30<br>2MASS J05250755+0134243<br>PTF1 J052507.55+013424.3 |
| RA                       | $05^{\text{h}}.25^{\text{m}}.07^{\text{s}}.55$                |
| Dec                      | $+01^{\circ}.34'.24.3''$                                      |
| V                        | 16.26 mag   |
| $T_{\text{eff}}$         | 3470 K  |
| $R_{\star}$              | $1.39 R_{\odot}$  |
| $M_{\star}$              | $0.44M_{\odot}/0.34M_{\odot}$                                 |
| $P_{\text{rot}}$         | $<0.671$ days   |
| Age                      | 2.63 Myr/ 2.68 Myr  |

From the subsequent photometric transit observation and spectroscopic radial velocity measurement after the first detection, PTFO 8-8695 is now supposed to harbour one close-in planet (PTFO 8-8695 b) with planetary mass  $M_{\text{p}} < 5.5M_{\text{Jupiter}}$  (van Eyken et al. 2012).

Planet detection around the pre-main-sequence stars is quite difficult partly because the observable targets around such young stars are fairly rare, and partly because the central star's drastic stellar activity inevitably leads to the large noises in the photometry. Thus the data analysis and estimation of the properties of the system are very difficult. In spite of such a difficulty, van Eyken et al. (2012) succeeded in discovering PTFO 8-8695 b as the first transiting exoplanet candidate orbiting around a pre-main-sequence star. Although the interpretation of photometric and spectroscopic observational data in terms of transiting exoplanet remains to be confirmed, this exoplanet candidate PTFO 8-8695 b is now gathering much attention for the characterization (Ciardi et al. 2014). Although it is still possible that the exoplanet PTFO 8-8695 b is actually false positive, this work is expected to do serve as the groundwork for the future confirmation and investigation of this prospective exoplanet.

The transits of PTFO 8-8695 were observed in Palomar Observatory from 2009 December 1 - 2010 January 15 (hereafter, 2009 observation), and 2010 December 8 - 17 (in the same way, 2010 observation) as part of the Palomar Transient Factory (PTF) that ran from 2009 - 2012. This PTF project is a fully-automated, wide-field survey for a systematic exploration of the optical transient sky. The former observation gives 11 reliable transit light curves, and the latter provides 6 reliable ones with transit period of 0.448413 days (see Figures 2.1 and 2.2, and van Eyken et al. 2012). The top panel of Figure 2.3 depicts the phase-folded (piled up for each transit event) transit light curves for 2009 observation, while the bottom panel of Figure 2.3 is for 2010 observation. It should be noted here that these phase-folded light curves are totally different with each other in their shapes, and such a variability is not common in the ordinary transits. In addition to the variability of light curve, each shape of 2009/2010 light curve also seems strange and unexpected. 2009 light curve shows the convex-like, double-horned structure, and 2010 light curve is highly left-right asymmetric (transit ingress is longer than egress.). Both light curves are very different from the conventional ones (see Appendix C).

Furthermore, their transit depth also imposes an additional puzzle to be reconciled. In general, stellar flux is the brightest at the center of the stellar disk and becomes dimmer towards the stellar limb. This tendency is known as the *limb darkening effect*, whose details are explained as follows based on Gray (2008). In principle, the temperature is higher in the stellar inner core and becomes lower as it approaches the stellar outer envelope. As for the Sun, the inner core is thought to be over  $10^7$  K but surface temperature is around 6000 K. And higher temperature produces larger flux. Based on the fact that stars are so optically thick that emitted light cannot penetrate them but will be immediately absorbed by the surrounding stellar materials, the light we actually observe should be emitted from the stellar photosphere whose optical depth measured from the stellar surface corresponds to the unity ( $\tau \sim 1$ ). The  $\tau \sim 1$  line lies closer to the stellar inner core at the center of the stellar disk than the limb of the stellar disk, then it turns out that the light we observe from the central region of the stellar disk is emitted from deeper stellar photosphere compared to the light from the limb of the stellar disk. This fact results in the non-uniformity of the stellar flux throughout the stellar disk with the central region brighter than the stellar limb (Figure 2.4). When a transiting planet passes the edge of the stellar disk, the total

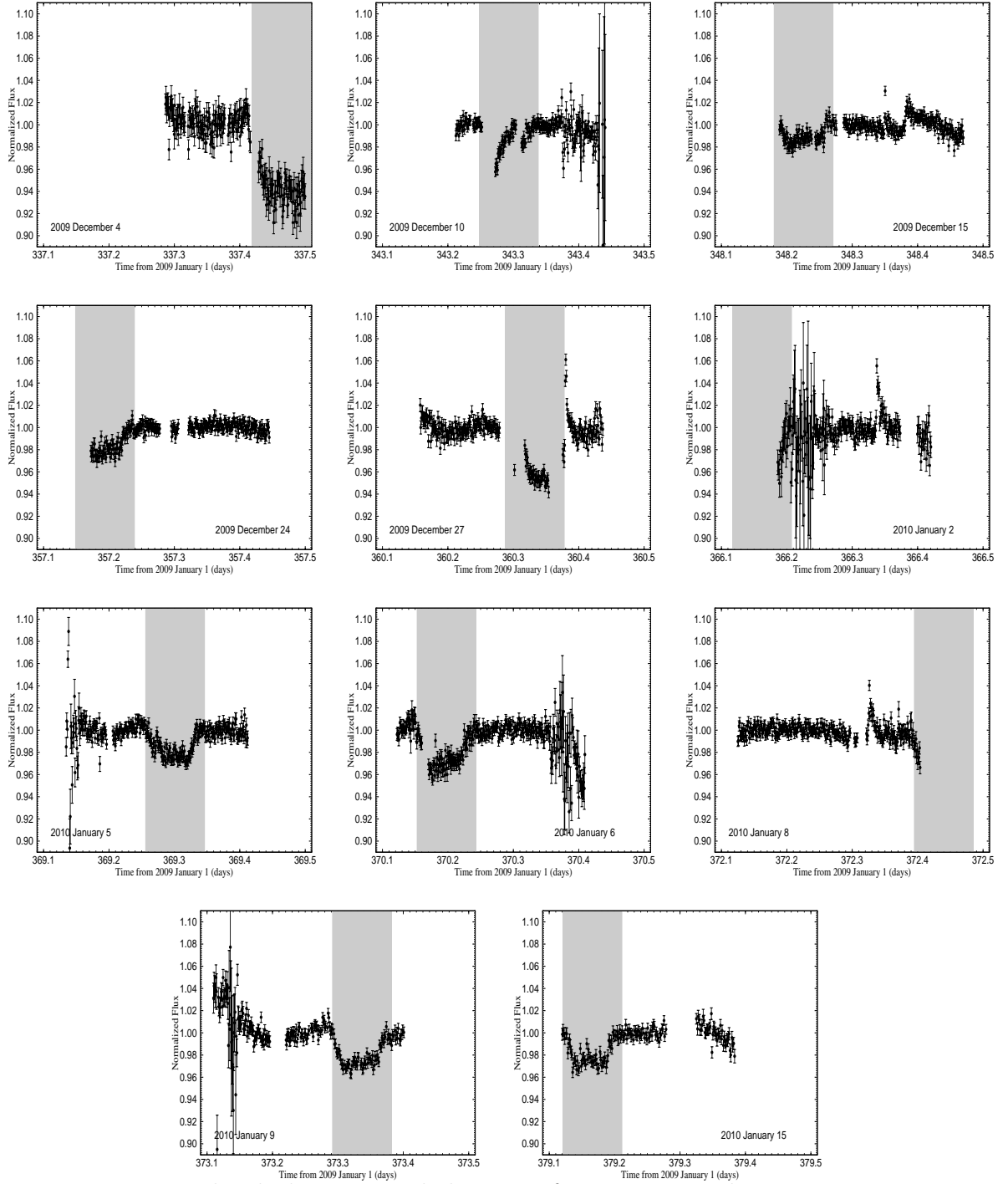


Figure 2.1: Normalized photometric light curve for 2009 December 4 - 2010 January 15. These observational data are identical with those used by B13. Light gray regions indicate the transit windows from ingress to egress with fixed transit period  $P = 0.448413$  days and epoch of transit center  $T_0 = 2455543.9402$  (HJD) following van Eyken et al. (2012).

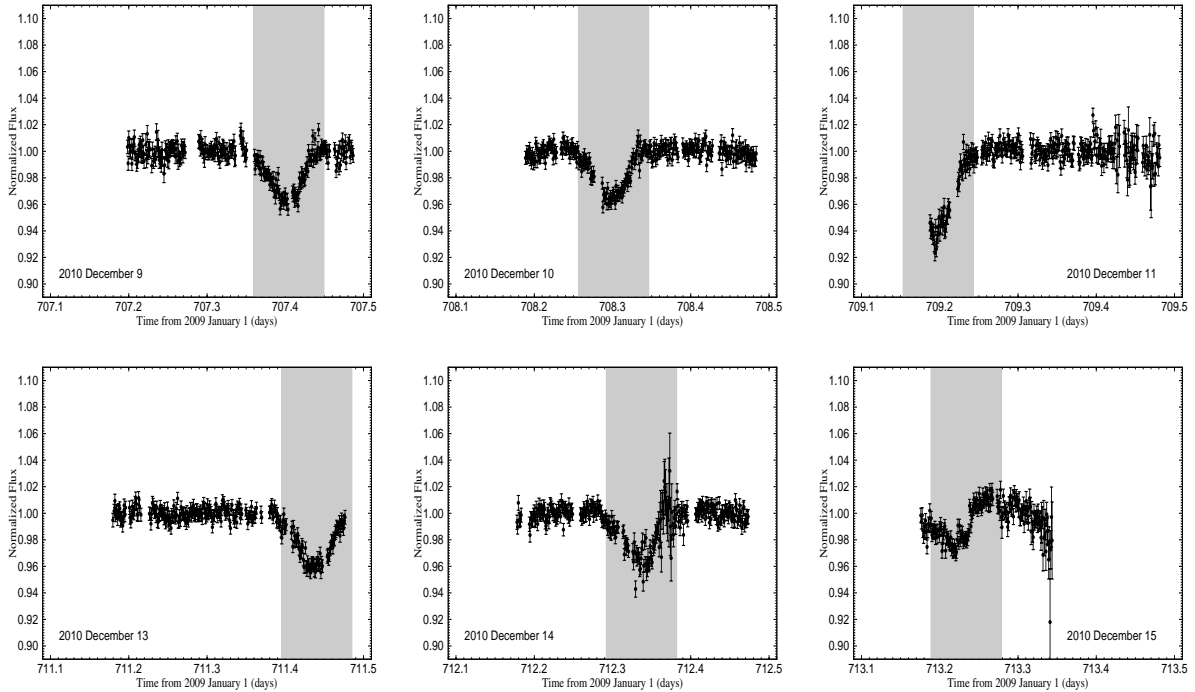


Figure 2.2: Same as Figure 2.1, but for 2010 December 9 - 2010 December 15 observations.

transit duration (from ingress to egress) becomes shorter than the duration when the planetary transit path resides near the stellar disk center. Combination of this tendency with the temperature distribution of the stellar disk gives a simple insight on the transit light curve shape that transit light curve shorter in duration tends to shallower in depth due to the limb darkening effect. However, 2009 light curve is longer in duration and *shallower* in depth, and 2010 light curve is shorter in duration and *deeper* in depth, both of which are inconsistent with the simple prediction of the limb darkening.

Up to this point, the problems on the transit light curve of PTFO 8-8695 are summarised into two; the significant difference between 2009/2010 light curves and unusual shape of the each transit light curve.

## 2.2 Gravity darkening effect and the nodal precession

The above two problems can be simultaneously solved by taking into account the stellar rapid rotation and short transit period (B13).

As shown in Table 2.1, spectroscopic radial velocity measurement suggested the upper limit on the stellar rotation period (equivalently, lower limit on the stellar spin frequency) as  $P_{\text{rot}} < 0.671$  days. Standard stellar evolution theory predicts that stars gradually lose their rotational angular momentum due to the magnetic braking during their evolution. Thus the pre-main-sequence stars are expected to rotate faster than main sequence stars. PTFO 8-8695 is the typical (or, even extreme) example of the rapid rotator, and its

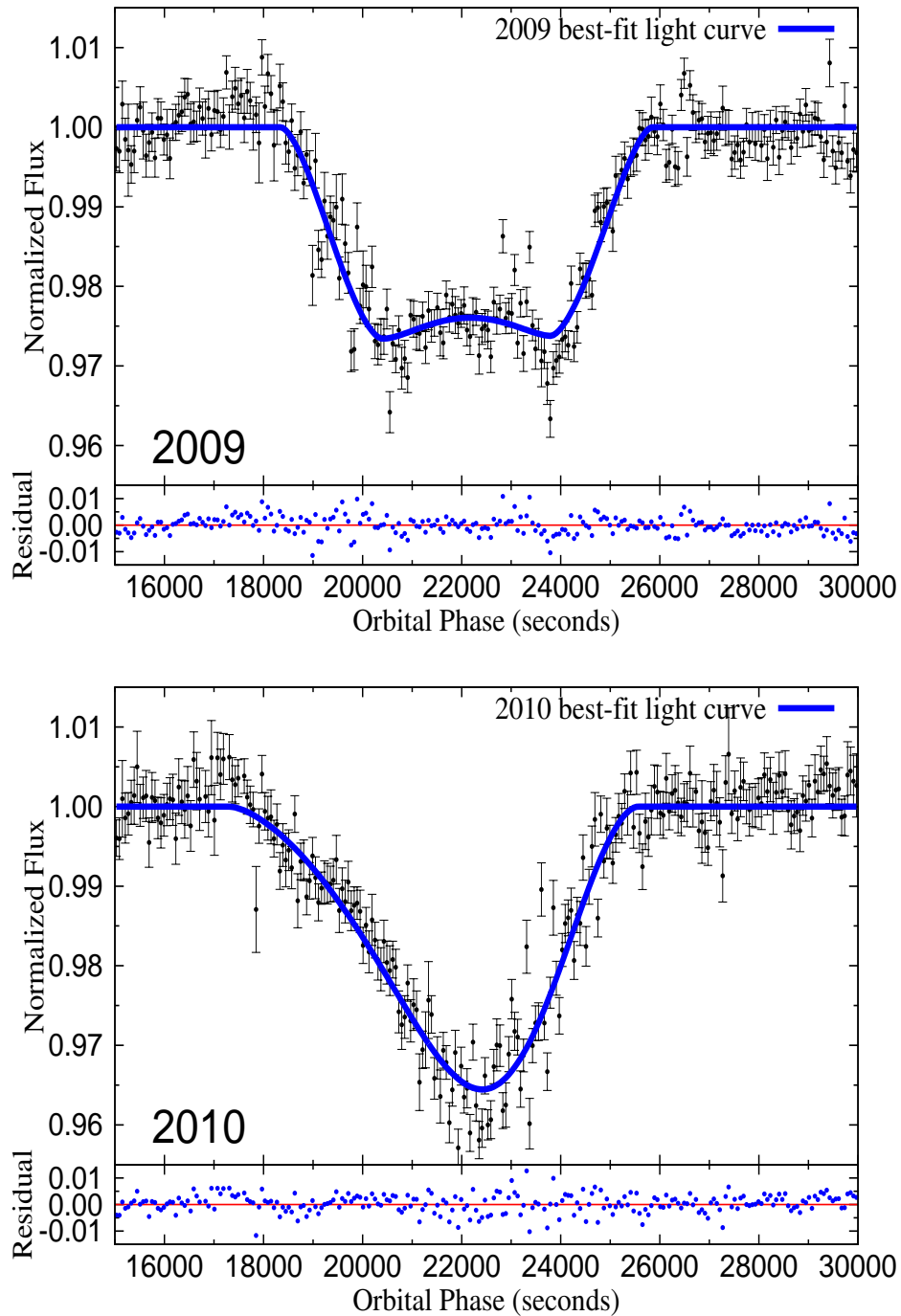


Figure 2.3: Phase-folded transit light curve of PTFO 8-8695 for 2009 (top) and 2010 (bottom) observation. The observed data is denoted as black points, and best-fit is as blue lines. The residuals from the fit are supplemented for each panel at the bottom.

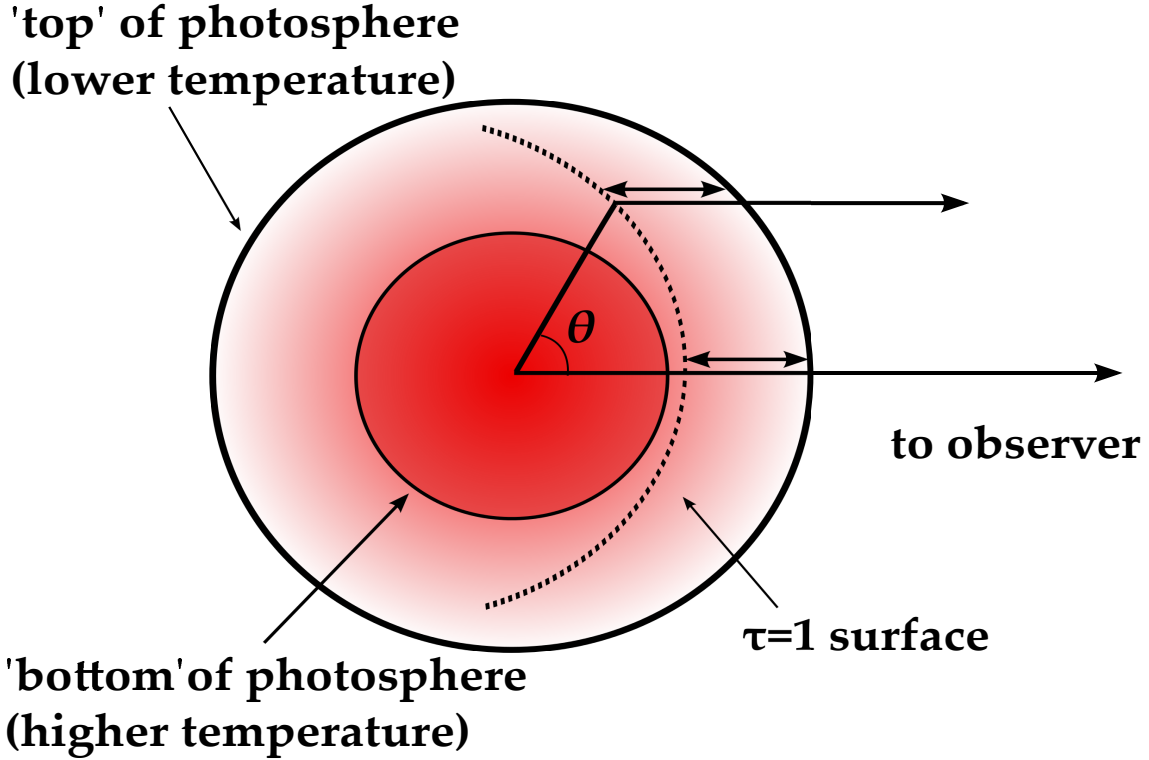


Figure 2.4: Schematic illustration of the limb darkening. The dashed curve indicates the surface of unit optical depth from the top of the photosphere. Unit optical depth into the photosphere corresponds to the different heights in the photosphere depending on  $\theta$ , the angle between line of sight and stellar surface normal. Figure modified from Gray (2008).

equator is expected to significantly expand compared to the polar radius due to its strong centrifugal force. The stellar oblateness  $f$ , which denotes the extent of the deformation from the spherical shape, is defined as

$$f = \frac{R_{\star,\text{eq}} - R_{\star,\text{pol}}}{R_{\star,\text{eq}}}, \quad (2.1)$$

where  $R_{\star,\text{eq}}$  and  $R_{\star,\text{pol}}$  are the stellar equatorial and polar radii, respectively.

This expanded stellar structure triggers an additional physical phenomenon, called *gravity darkening* (von Zeipel 1924). The expanded equatorial region result in the reduction of the pressure in that region compared to the polar region. Thus the surface temperature becomes lower at equator than at polar regions. Lower temperature corresponds to smaller stellar flux as mentioned above, then which induces additional surface temperature dependence on the latitude of the stellar surface with the equatorial region dimmer than the polar region. This gravity darkening is recently often used to measure the angular properties of the system including the spin-orbit angle  $\phi$  (Barnes 2013). Specifically, Barnes et al. (2011) and Szabó et al. (2012) characterized a planetary system KOI-13 that consists of rapidly rotating host star and exoplanet with gravity darkening model. Or, Zhou & Huang (2013) and Ahlers et al. (2014) applied gravity darkening

model to an eclipsing binary system with rapidly rotating A-dwarf and M-dwarf, KOI-368, and determined the spin-orbit angle  $\phi$ . This gravitational darkening effect plays an important role also in estimating the physical properties of PTFO 8-8695 system.

Another important process to explain PTFO 8-8695’s unusual transit light curves is the nodal precession of stellar spin axis and planetary orbital axis. As mentioned, the stellar rapid rotation ( $P_{\text{rot}} < 0.671$  days) makes its shape significantly deviate from a sphere. Furthermore, transit period (identical with planetary orbital period) of 0.448413 days is so short that Kepler’s third law indicates that planetary semi-major axis is smaller than 2 stellar radii, just on the verge of stellar Roche radius within which the planet would be tidally destroyed. When both central star and the orbiting planet can be assumed as point-masses, their gravitational interaction is described as the Keplerian force that obeys the simple inverse-square law. In the case of PTFO 8-8695, however, the central star is not spherical but has a rotational bulge and the planet around it has an extremely small orbit. Therefore both central star and planet are expected to suffer from not only the simple Keplerian force but also the mutual strong torque (non-Keplerian force acting on the stellar rotational bulge). Thereby this torque let both stellar rotational angular momentum vector (namely, stellar spin axis) and planetary orbital angular momentum vector (namely, planetary orbital axis) change their directions with time. Thus these vectors precess around the time-invariant total angular momentum vector with one vector being located always in the opposite side of the other (nodal precession, see Figure 2.5). It

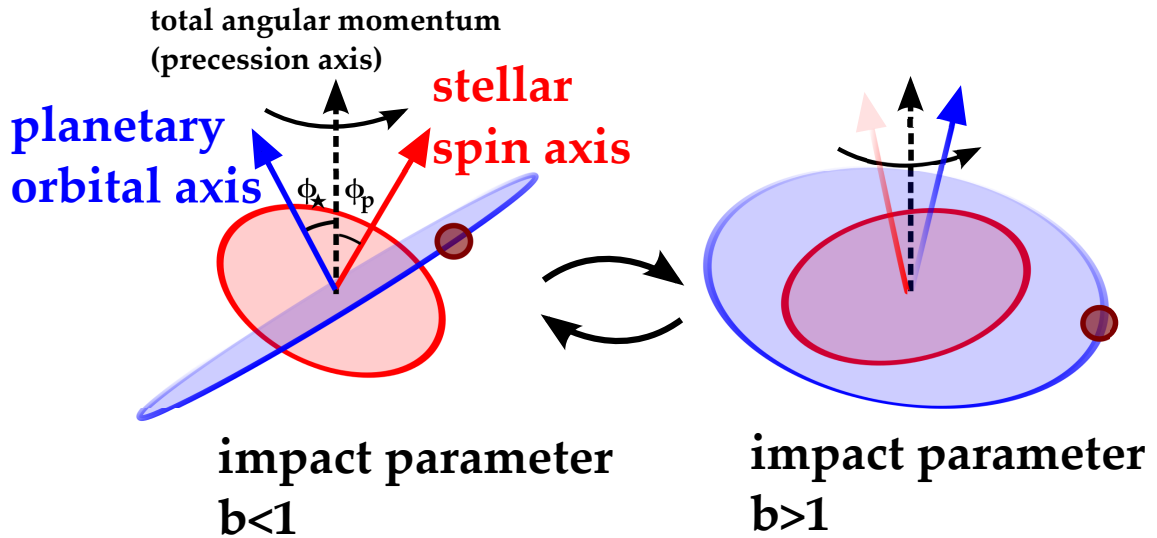


Figure 2.5: Schematic illustration of the nodal precession in PTFO 8-8695 system. Both stellar spin axis (red) and planetary orbital axis (blue) precess around their time-invariant total angular momentum vector (dashed vector).

is possible that the system gets into the phase during which the transits never take place since the transit impact parameter (see Appendix C) exceeds unity ( $b > 1$ , right panel in Figure 2.5). Note that the nodal precession itself is common in our solar system, for example the relation between Saturnian spin axis and its satellite’s orbital axis. In most

of those situations, however, one vector overwhelms the other in magnitude, resulting in the situation where the smaller one effectively precesses around the larger one such as the precession of the orbital axis of Saturnian satellite around its host planet. In the case of PTFO 8-8695, however, the stellar spin and planetary orbital angular momenta are comparable in magnitude. Thus they exhibit *mutual* precession around the time-invariant total angular momentum. When the nodal precession occurs, the central star changes its direction in the sky plane and accordingly the planetary orbit in the sky plane also varies with time. This explains the time variability of the transit light curves whose details are discussed in the next section.

In fact, the behavior of the precession is quite sensitive to the angle between the stellar spin axis and the planetary orbital axis (spin-orbit angle  $\phi$ ; see Appendix A for the introduction of  $\phi$  and to what areas the statistics on  $\phi$  can contribute). Thereby that dependence makes it possible to constrain the stellar spin direction and planetary orbital direction through the analysis of the precession. To say further, the detection ability of spin-orbit angle  $\phi$  by this model rises as the central star rotates rapidly. This is because larger extent of rotational deformation induced by more rapid rotation accelerates the nodal precession (see chapter 3 for the analytic expressions), which appears as more dramatic time-variability of the transit light curves. Here the Rossiter-McLaughlin effect (hereafter, the RM effect), the most popular method for the constraints on the projected spin-orbit angle  $\lambda$ , decreases its detection ability of  $\lambda$  when the central star is the rapid rotator (see Appendix A). Therefore the nodal precession accompanied by the gravity darkening effect compensates for the rapid rotators which the RM effect is hard to be applied to in context of the measurement of the spin-orbit angle  $\phi$  of the extrasolar planetary systems of interest. Namely, the RM effect is useful for the systems with non-rapid rotators (generally, matured stars), while gravity darkening effect is for those with rapid rotators (generally, younger stars). It is worthwhile to measure  $\phi$  for younger stars since it is more likely that the stellar spin and planetary orbit in those systems hold the primordial memories on  $\phi$ . This is because the stellar spin and/or planetary orbit are expected to be less affected by the tidal interaction (see chapter 5 and Appendix A) which could alter  $\phi$  with time since the age of the system itself is anyhow younger than those of main sequence stars.

## 2.3 Strategy in Barnes et al. (2013)

B13 first analyzed the 2009 and 2010 transit light curves individually with the gravity darkening model, and estimated the satisfactory system parameters with errors. After that, they performed 2009-2010 simultaneous fitting for the purpose of determining the system parameters in more self-consistent fashion.

### 2.3.1 Individual fittings

Based on the gravity darkening effect and the nodal precession, B13 determined the 6 system parameters (stellar radius  $R_*$ , planetary radius  $R_p$ , time of inferior conjunction

$t_0$ , orbital inclination  $i$ , projected spin-orbit angle  $\lambda$  and stellar obliquity  $\psi$ ) so as to reproduce the shape of the phase-folded transit light curve.  $t_0$  is measured in seconds past 2009 January at midnight UTC. Note that the derivation of the best-fit parameters here does not require the stellar and planetary masses ( $M_\star$  and  $M_p$ ). Another important point in their work is that they employed the spin-orbit synchronous condition under which the stellar rotational period is considered to be coincidental with the planetary orbital period. Namely, the stellar spin period is not a fitting but fixed parameter. The reason and validity of this assumption are discussed in the next section below. First this fitting was done against 2009/2010 observational data individually. Their results of the angular parameters from 2009 and 2010 individual fitting could be different with each other because nodal precession changes the angular configuration of the system in the sky plane with time. The mathematical treatment of the gravity gardening effect is described in Barnes (2009) and Barnes et al. (2011). We note that in general two angular parameters (polar and azimuthal angles) are required to represent the direction of the vector in the three dimensional coordinates. Since we have the one degree of freedom corresponding to the rotation of the sky plane with respect to the line of sight, the number of angular parameters necessary to denote the directions of both stellar spin and planetary orbit becomes three (orbital inclination  $i$ , projected spin-orbit angle  $\lambda$  and stellar obliquity  $\psi$ ), not four. One is to denote the stellar spin direction, and the other two are to denote the planetary orbital axis with respect to the stellar spin axis. In addition, it is worth emphasizing that each angular parameter in B13 is different from that conventionally used, and their correspondence is summarized in Table 2.1. Their geometric configurations and correspondence are explained in Figures 2.6 and 2.7.

Table 2.1: Relation between parameters in B13 and conventional ones

| term in B13                          | conventional term                        | relation                   |
|--------------------------------------|--|----------------------------|
| orbital inclination $i$              | orbital inclination $i_{\text{orb}}$     | $i_{\text{orb}} = \pi - i$ |
| projected spin-orbit angle $\lambda$ | longitude of the ascending node $\Omega$ | $\Omega = \pi - \lambda$   |
| stellar obliquity $\psi$             | stellar inclination $i_\star$            | $i_\star = \psi + \pi/2$   |

Angular parameters are defined as follows. The planetary orbital inclination,  $i$ , is measured toward the observer from the line of sight that penetrates the sky plane from the observer's side to the opposite side, while  $i_{\text{orb}} (= \pi - i)$  is measured from the line of sight pointing the observer (Figure 2.6). The projected spin-orbit angle,  $\lambda$ , is the angle between  $y$ -axis (parallel to the stellar spin axis projected onto the sky plane) and the planetary orbital axis projected onto the sky plane measured clockwise. The angle between  $x$ -axis and the direction pointing the ascending node is denoted by  $\Omega (= \pi - \lambda)$  (Figure 2.7). Finally,  $\psi$  is measured as the angle with which the north stellar pole is tilted away from the sky plane, and  $i_\star (= \psi + \pi/2)$  is measured in the same way as  $i_{\text{orb}}$  (Figure 2.6). With the help of the three angular parameters, the directions of angular momentum

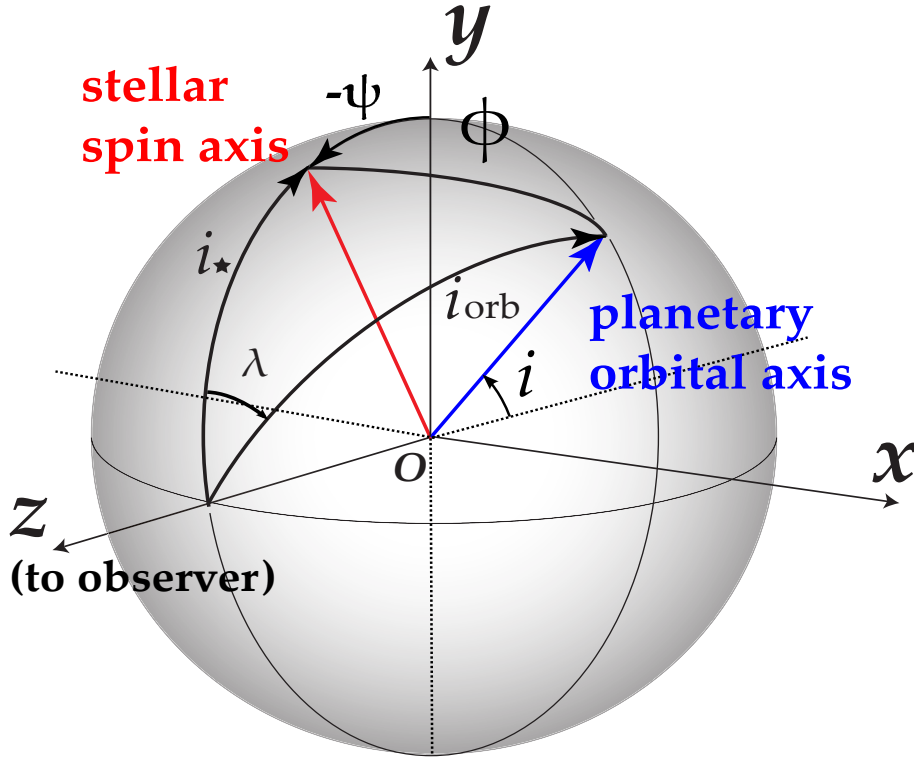


Figure 2.6: Schematic illustration of the geometric configurations of star-planet system. The coordinates are set with the origin centered on the star with  $x-y$  plane corresponding the sky plane and positive  $z$ -direction pointing toward the observer. Positive  $y$ -direction are determined so that stellar spin axis projected onto the sky plane coincides with it forming a right-handed triad with  $x$  and  $z$ -axes. Figure modified from Benomar et al. (2014).

vectors ( $\mathbf{S}_0$  and  $\mathbf{L}$ ) are written as

$$\hat{\mathbf{S}}_0 = \begin{pmatrix} 0 \\ \cos \psi \\ -\sin \psi \end{pmatrix} = \begin{pmatrix} 0 \\ \sin i_* \\ \cos i_* \end{pmatrix}, \quad (2.2)$$

$$\hat{\mathbf{L}} = \begin{pmatrix} \sin i \sin \lambda \\ \sin i \cos \lambda \\ -\cos i \end{pmatrix} = \begin{pmatrix} \sin i_{\text{orb}} \sin \Omega \\ -\sin i_{\text{orb}} \cos \Omega \\ \cos i_{\text{orb}} \end{pmatrix}, \quad (2.3)$$

which are related to the spin-orbit angle  $\phi$  as

$$\begin{aligned} \cos \phi &= \hat{\mathbf{S}}_0 \cdot \hat{\mathbf{L}} \\ &= \cos \psi \sin i \cos \lambda + \sin \psi \cos i = -\sin i_* \sin i_{\text{orb}} \cos \Omega + \cos i_* \cos i_{\text{orb}}. \end{aligned} \quad (2.4)$$

The results of the individual fits by B13 are summarized in Table 2.2. The difference

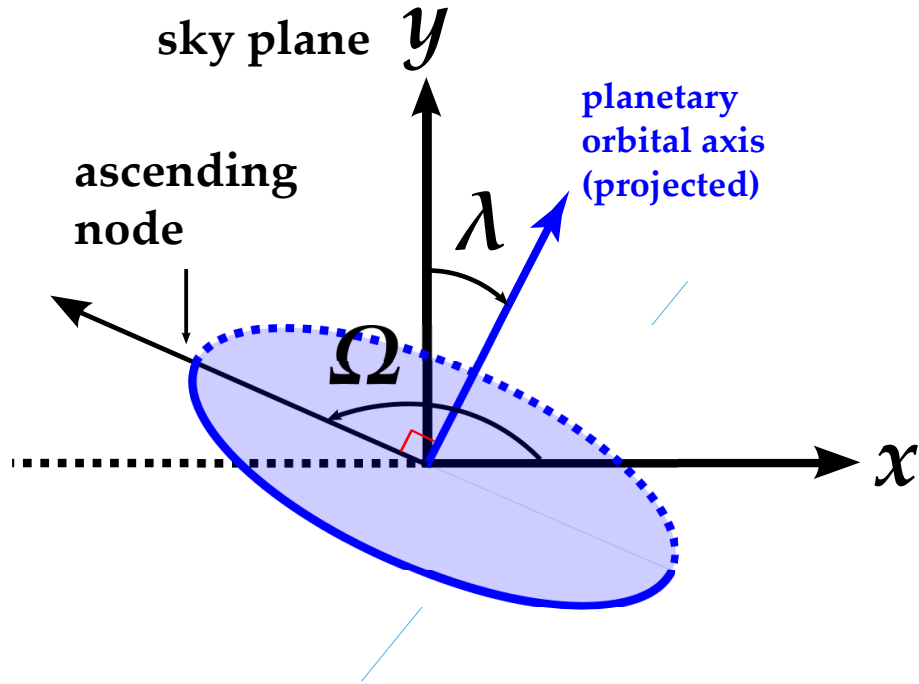


Figure 2.7: Schematic illustration for the projected spin-orbit angle ( $\lambda$ ) and longitude of the ascending node ( $\Omega$ ). The angle of planetary orbital axis projected onto the sky plane,  $\lambda$ , is defined to be measured clockwise from the positive  $y$ -axis. We define  $\Omega$  as the angle of the direction pointing the ascending node measured counter-clockwise from the positive  $x$ -axis, i.e.,  $\lambda + \Omega = \pi$ .

Table 2.2: Individual fits by B13

| parameter           | 2009               | 2010               |
|---------------------|--------------------|--------------------|
| $R_*(R_\odot)$      | $1.19 \pm 0.07$    | $1.39 \pm 0.11$    |
| $R_p(R_J)$          | $2.00 \pm 0.17$    | $1.80 \pm 0.20$    |
| $t_0(\text{s})$     | $30861700 \pm 200$ | $60848300 \pm 290$ |
| $i(^{\circ})$       | $64 \pm 3$         | $58 \pm 5$         |
| $\lambda(^{\circ})$ | $90 \pm 22$        | $136 \pm 33$       |
| $\psi(^{\circ})$    | $2 \pm 19$         | $31 \pm 25$        |
| $\phi(^{\circ})$    | 89.1               | 104.5              |
| $\chi_r^2$          | 2.11               | 1.54               |

of angular parameters between 2009 and 2010 could be attributed to the nodal precession. We present a detailed formulation of the nodal precession in the following chapter, but briefly review here the angular architecture of the system and resulting transit light curves in 2009 and 2010 observations. In 2009, the stellar spin axis is almost on the sky plane ( $\psi = 2^{\circ}$ ) so that we observed the star from edge-on. Then the planetary orbit is almost

polar ( $\lambda = 90^\circ$ ), letting the planet passing first polar region, next equator region and finally polar region, respectively (left panel of Figure 2.8). Consequently, planet moves from the brighter to dimmer and then brighter regions with time, resulting in the convex-like structure in the 2009 transit light curve as shown in Figure 2.3. In 2010 on the other hand, the stellar spin axis is significantly tilted away from the sky plane ( $\psi = 31^\circ$ ). So the star exposes its the equator and south pole but does not show north pole in the sky plane. The planet takes almost diagonal path in the sky plane ( $\lambda = 136^\circ$ ), letting the planet enter the stellar disk at the equator region and leaves at the polar region (right panel of Figure 2.8). Again the stellar disk is significantly oblate due to the rapid rotation with larger equatorial radius than polar radius. Thereby, the star experiences longer time occultation due to the planet in the equator region compared to the shorter occultation in the polar region. Thus the observed transit light curve becomes highly asymmetric (longer transit ingress and shorter transit egress) as shown in Figure 2.3.

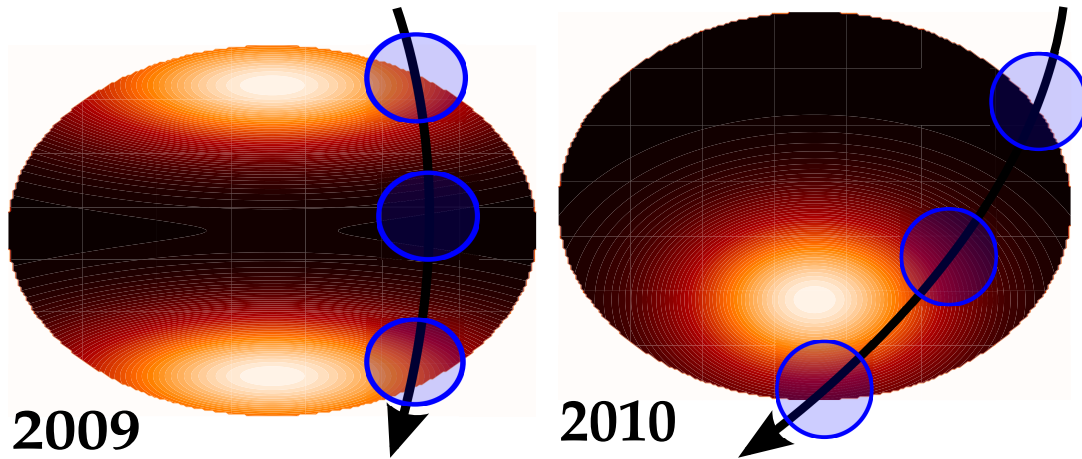


Figure 2.8: Transit geometry of PTFO 8-8695 for the best-fit parameter sets in 2009 (left) and 2010 (right). In each image the planetary transit path is shown as the black curve with a series of blue circles indicating the planetary disk. Note here that the transit path is not straight line but significantly curved since the planetary semi-major axis is so small that it is less than 2 stellar radii.

Among the three angular parameters, orbital inclination  $i$  is well constrained because a slight change in  $i$  sensitively affects the transit duration. For  $\lambda$  and  $\psi$ , however, their  $1\sigma$  constraints are not as strong as the one for  $i$  because their variance shows up only as a small modification of the shapes of transit light curves through gravity darkening effect.

Before proceeding to the next section, we should note the presence of four-fold degeneracy for the three angular parameters (see Barnes et al. 2011 for details), and this degeneracy should be taken into account in the following joint fitting. Specifically, the four different sets of angular parameters give the identical transit light curves for given angular parameters  $(i_{\text{orb}}, \Omega, i_\star)$ :

1.  $(i_{\text{orb}}, \Omega, i_\star)$
2.  $(\pi - i_{\text{orb}}, \pi - \Omega, i_\star)$

3.  $(\pi - i_{\text{orb}}, -\Omega, \pi - i_{\star})$
4.  $(i_{\text{orb}}, \Omega - \pi, \pi - i_{\star})$

Or equivalently, they are rewritten in terms of  $(i, \lambda, \psi)$ :

1.  $(\pi - i, \pi - \lambda, \psi)$
2.  $(i, \lambda, \psi)$
3.  $(i, \lambda - \pi, -\psi)$
4.  $(\pi - i, -\lambda, -\psi)$

Because of the above degeneracy, for example, the 2010 individual fits of B13 provide other three alternative sets of angular parameters for the solution as shown in Table 2.3 and Figure 2.9. We note that the first case and the third case express the identical

Table 2.3: Four-fold degeneracy in the angular parameters of the system with 2010 individual fits in B13

|                                      | $i(^{\circ})$ | $\lambda(^{\circ})$ | $\psi(^{\circ})$ | $\phi(^{\circ})$   |
|--------------------------------------|---------------|---------------------|------------------|--------------------|
| 1 (top-left panel in Figure 2.9)     | 58            | 136                 | 31               | 104.5 (retrograde) |
| 2 (top-right panel in Figure 2.9)    | 122           | 44                  | 31               | 75.5 (prograde)    |
| 3 (bottom-left panel in Figure 2.9)  | 122           | 224                 | -31              | 104.5 (retrograde) |
| 4 (bottom-right panel in Figure 2.9) | 58            | 316                 | -31              | 75.5 (prograde)    |

system configuration, the same transit just seen by the opposite side with each other. This relation is also true to the second case and the fourth case. The first case and second case, on the contrary, give different angular configuration letting the spin-orbit angle  $\phi$  form the supplementary angle with each other ( $\phi_{\text{case2}} = \pi - \phi_{\text{case1}}$ ). Again this is also the case for the third case and fourth case.

### 2.3.2 Extrapolation of the individual fittings

The nodal precession should be responsible for the difference of the system configuration in 2009 and 2010. Namely, the torque between the star and the planet should change their angular parameters in 2009 to those in 2010 in one year interval. Based on this hypothesis, B13 formulated the analytic equations that represent the nodal precession (see chapter 3 for details). Then they extrapolated 2009/2010 best-fit parameters forward/backward to 2010/2009 observation epoch in order to check to what extent the precession hypothesis can simultaneously explain the observed light curves. The magnitudes of the stellar spin and planetary orbital angular momenta ( $|\mathbf{S}_{\star}|$  and  $|\mathbf{L}|$ , respectively) are expressed as

$$|\mathbf{S}_{\star}| = \tilde{C}_{\star} M_{\star} R_{\star, \text{eq}}^2 \omega_{\star}, \tag{2.5}$$

$$|\mathbf{L}| = \beta \sqrt{\mu a (1 - e^2)}, \tag{2.6}$$

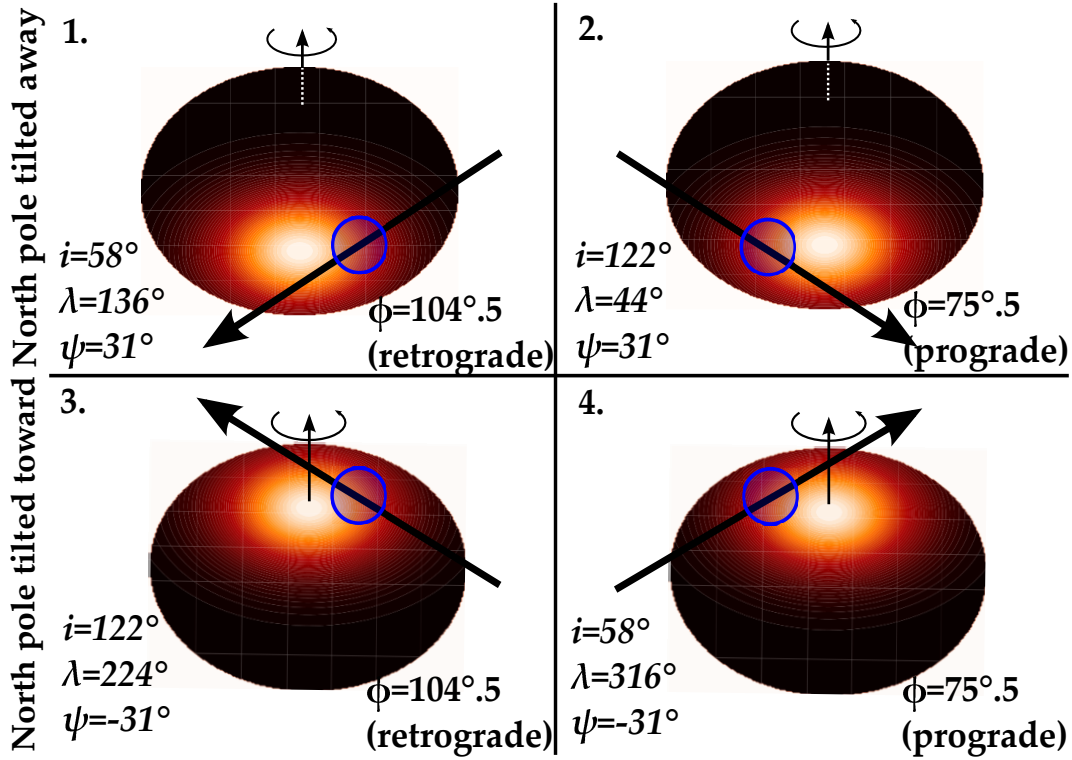


Figure 2.9: Four allowed geometries for the PTFO 8-8695 2010 transit event.

where  $\tilde{C}_*$  is the moment of inertia coefficient for the star,  $\beta = \frac{M_* M_p}{M_* + M_p}$  is the reduced mass and  $\mu = G(M_* + M_p)$  is the total mass of the star-planet system multiplied by the gravitational constant  $G$ . We note that the precession formulae include the additional information on the mass (stellar mass  $M_*$  and planetary mass  $M_p$ ) since the magnitudes of stellar spin and planetary orbital angular momenta directly depend on these masses. B13 assumed  $M_* = 0.44M_\odot$  and  $M_p = 1.0M_J$  in the extrapolation, but these values are just for simplicity then there is no need that the extrapolation is successful.

Results of both forward (from 2009 to 2010) and backward (from 2010 to 2009) extrapolations are illustrated in Figures 2.10 and 2.12, respectively. As expected above, the forward-extrapolated light curve from 2009 to 2010 turns out to completely fail to reproduce the 2010 transit light curve (Figure 2.10). In Figure 2.12, similarly, this failure is also true for the backward-extrapolated 2010 light curve. These results show the necessity to treat the masses as fitting parameters. Both figures are supplemented with the additional panels (Figures 2.11 and 2.13) that show the predicted evolutions of transit light curves during the interval between 2009 and 2010. The time span of the horizontal axis is so long that each transit light curve looks like a needle. Thereby these figures essentially illustrate the time evolution of the transit depth alone. The difference in the variability of transit depth between Figures 2.11 and 2.13 are discussed in the next chapter.

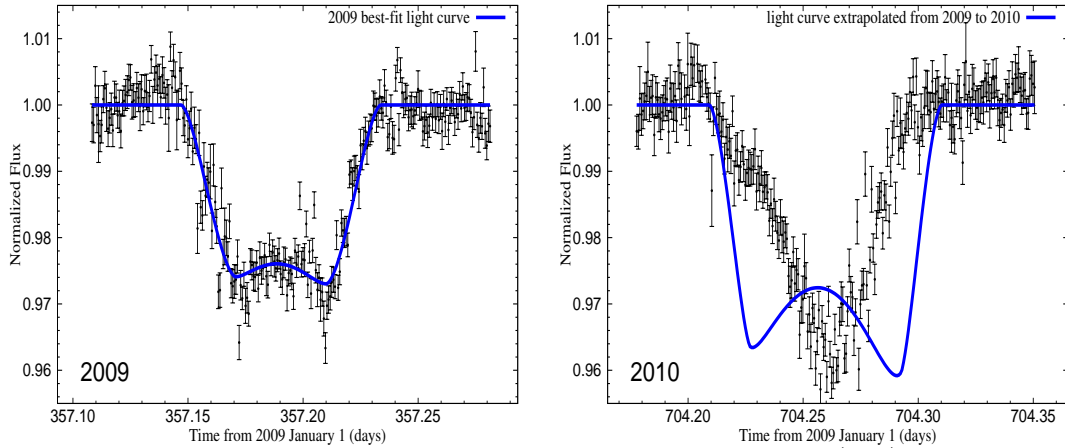


Figure 2.10: 2009 best-fit light curve by 2009 individual fit (left) and its forward-extrapolated light curve from 2009 to 2010 via the nodal precession for  $M_{\star} = 0.44M_{\odot}$  and  $M_{\text{p}} = 1.0M_{\text{J}}$  (right).

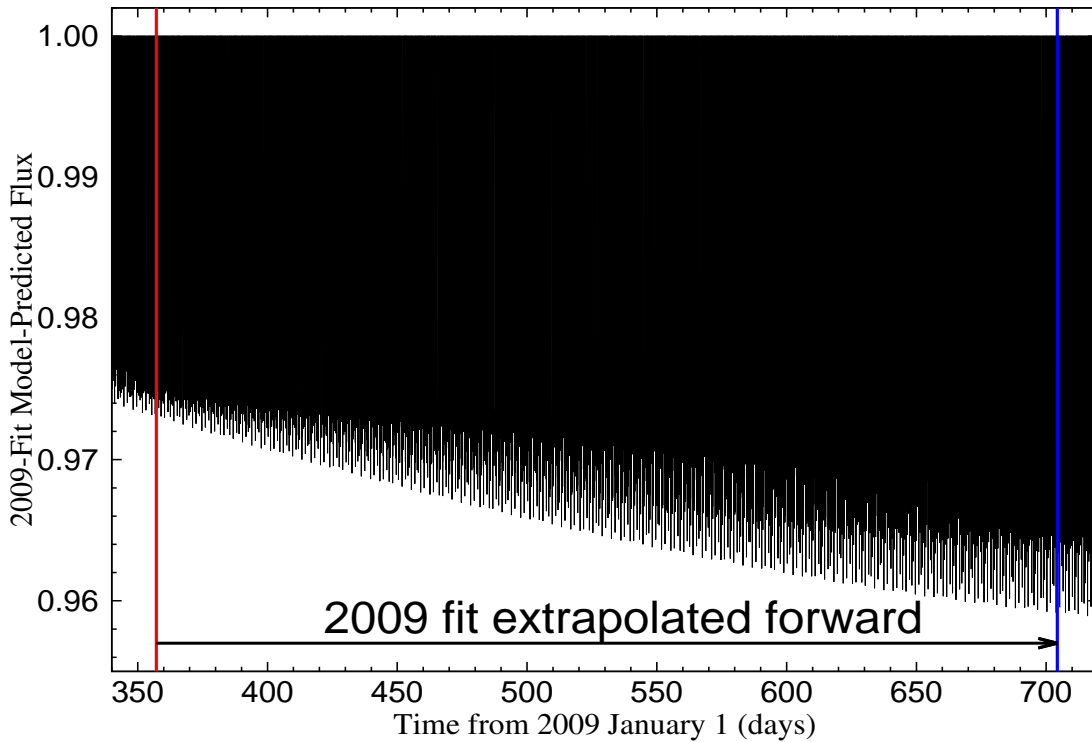


Figure 2.11: Forward-extrapolation from 2009 to 2010 with the results of 2009 individual fit in Table 2.2. The epochs of 2009 and 2010 observations correspond to the colored vertical lines, red and blue, respectively.

### 2.3.3 Joint fittings

In response to above results, B13 explored the best-fit parameters with which both 2009 and 2010 light curves can be reproduced simultaneously in the self-consistent way, letting

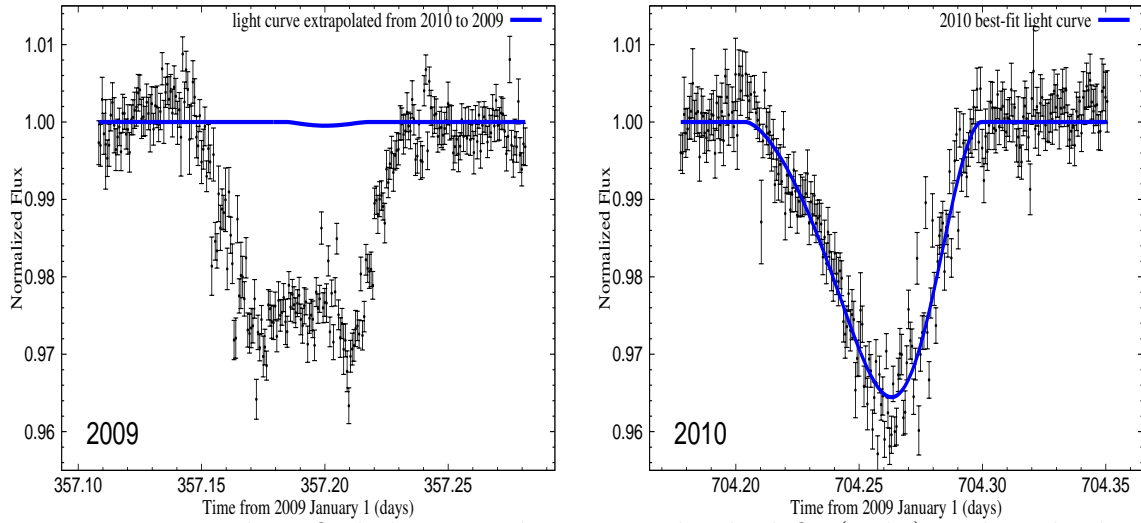


Figure 2.12: 2010 best-fit light curve by 2010 individual fit (right) and its backward-extrapolated light curve from 2010 to 2009 via the nodal precession for  $M_{\star} = 0.44M_{\odot}$  and  $M_{\text{p}} = 1.0M_{\text{J}}$  (left).

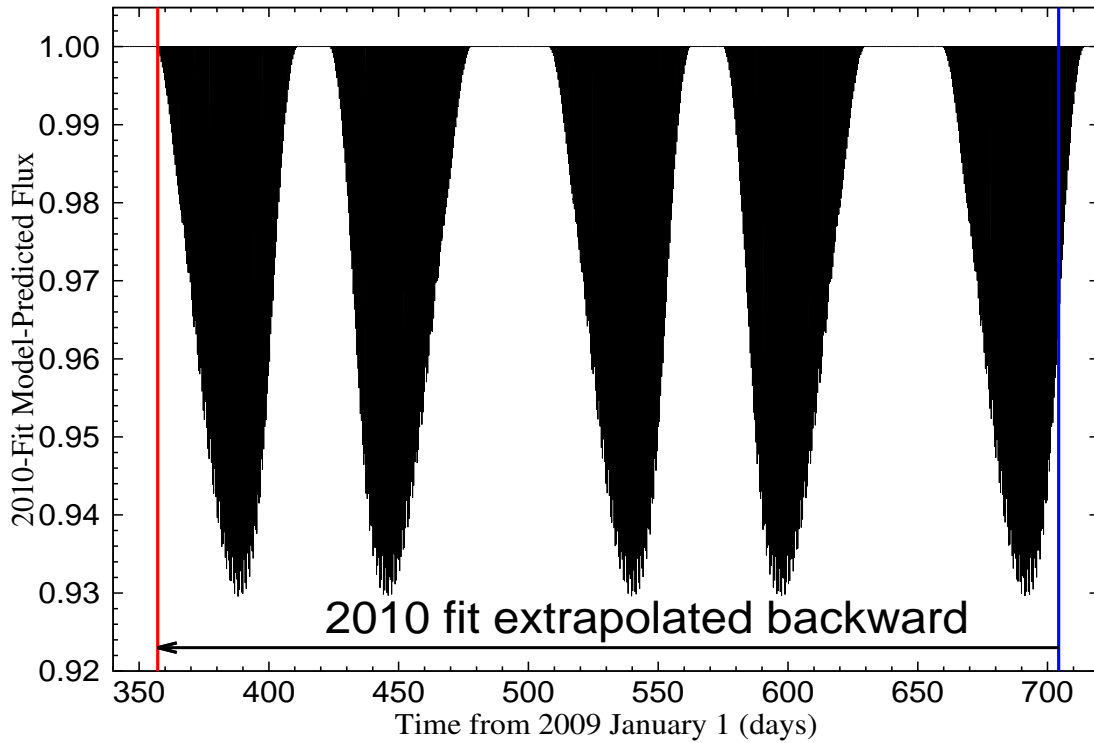


Figure 2.13: Backward-extrapolation from 2010 to 2009 with the results of 2010 individual fit in Table 2.2. The epochs of 2009 and 2010 observations correspond to the colored vertical lines, red and blue, respectively.

planetary mass  $M_p$  be the additional fitting parameter responsible for the magnitude of planetary orbital angular momentum. In this joint fitting the stellar mass was fixed to  $M_\star = 0.34M_\odot$  or  $M_\star = 0.44M_\odot$ , whose values are estimated in van Eyken et al. (2012) with different stellar models (Baraffe et al. 1998 and Siess et al. 2000). The reason why the stellar mass is not a fitting but a fixed parameter is as follows. In fact, the precession state and transit light curve depend not on the stellar mass ( $M_\star$ ) and stellar radius ( $R_\star$ ) separately, but only on the stellar mean density  $\rho_\star = M_\star / \frac{4}{3}\pi R_\star^3$  (see Appendix C.2.3). Since such a degeneracy makes it impossible to evaluate  $M_\star$  and  $R_\star$  separately, they fixed  $M_\star$  and vary only  $R_\star$ . Parameter ranges swept are  $0.8R_\odot < R_\star < 1.6R_\odot$ ,  $0 < M_p < 100M_J$  and within the bounds of 2010 individual fit for angular parameters ( $i, \lambda, \psi$ ).

Here we should recall that the system admits the four-fold degeneracy with respect to the three angular parameters, making the two out of them having the different spin-orbit angle ( $\phi_2$ ) from that of the remaining two ( $\phi_1$ ). Since they are in the relation of  $\phi_2 = \pi - \phi_1$ , one of them is always prograde solution and the other is correspondingly retrograde. The value of  $\phi$  is time-invariant (see chapter 3), therefore the 2010 prograde solution should correspond to the 2009 prograde solution. This is also the case for the retrograde solutions. Here the precession period is quite sensitive to  $\phi$  (see chapter 3 for details), which enables us to disentangle the degeneracy of the system configuration (prograde or retrograde) by conducting the 2009-2010 joint fitting through the calculation of the nodal precession. Therefore, there exist two patterns for the angular ranges to be surveyed, one is prograde and the other is retrograde.

B13 reported that they failed to identify the retrograde solution and gave only prograde solution summarized below, for two stellar mass cases. In Table 2.4,  $P_{\text{orb}}$  is the planetary orbital period,  $t_0$  is the epoch of inferior conjunction measured from 2009 January 1st 0:00 UTC,  $\phi_\star$  is the angle between the stellar spin axis and total angular momentum vector (see Figure 2.5),  $\phi_p$  is the angle between the planetary orbital axis and total angular momentum vector (again see Figure 2.5),  $P_\Omega$  is the precession period and  $f$  is the stellar oblateness defined in equation (2.1). Fitting parameters are  $R_\star, R_p, P_{\text{orb}}, t_0, i, \lambda, \psi, M_p$ , while other parameters in Table 2.4 are derived ones from the fitted parameters. B13 succeeded in not only estimating the planetary mass in addition to the parameters in the individual fits, but also constraining the three angular parameters much tighter down to the first decimal place. This is because there exists the long base-line in the joint fittings up to one year compared to the simple individual fittings. Since the backward calculation of the precession from 2010 to 2009 should be responsible to reproduce the 2009 individual fitting results, only smaller region within the wider bounds of the 2010 individual fitting is approved for the joint solutions.

Figures 2.14 and 2.16 show the theoretical calculation of the transit light curves with  $M_\star = 0.34$  and  $0.44M_\odot$  respectively. The best-fits in the individual and joint fitting are denoted as red and blue curves respectively showing good agreement with each other. From figures, it can be confirmed that these best-fit parameters can self-consistently reproduce the 2009 observation and 2010 observation simultaneously. Each figure is supplemented with the figure illustrating the long term variation of the transit light curve between 2009 and 2010 observation (Figures 2.15 and 2.17). Specifically, each black solid line corre-

Table 2.4: Best-fit parameters from the joint analysis of the 2009 and 2010 light curves in B13

| parameter                       | $M_\star = 0.34M_\odot$ | $M_\star = 0.44M_\odot$ |
|---------------------------------|-------------------------|-------------------------|
| $R_\star(R_\odot)$              | $1.04\pm 0.11$          | $1.03\pm 0.01$          |
| $R_p(R_J)$                      | $1.64\pm 0.07$          | $1.68\pm 0.07$          |
| $P_{\text{orb}}(\text{days})$   | $0.448410\pm 0.000004$  | $0.448413\pm 0.000001$  |
| $t_0(\text{s})$                 | $60848500\pm 100$       | $60848363\pm 38$        |
| $i(^{\circ})$                   | $114.8\pm 1.6$          | $110.7\pm 1.3$          |
| $\lambda(^{\circ})$             | $43.9\pm 5.2$           | $54.5\pm 0.5$           |
| $\psi(^{\circ})$                | $29.4\pm 0.3$           | $30.3\pm 1.3$           |
| $M_p(M_J)$                      | $3.0\pm 0.2$            | $3.6\pm 0.3$            |
| $\phi(^{\circ})$                | $69\pm 3$               | $73.1\pm 0.6$           |
| $\phi_\star(^{\circ})$          | 18                      | 20.2                    |
| $\phi_p(^{\circ})$              | 51                      | 52.9                    |
| $P_{\dot{\Omega}}(\text{days})$ | 292.6                   | 581.2                   |
| $f$                             | 0.109                   | 0.083                   |
| $\chi_r^2$                      | 2.17                    | 2.19                    |

sponds to the one transit light curve and from left to right this panel briefly depicts the transit depth variance with time. Note that in both figures transit light curves are predicted to disappear for several months during which the planet never crosses the stellar disk in the sky plane, which plays an important role in the future observation discussed in chapter 5.

We put emphasis here that the precession in  $0.34M_\odot$  case is much faster than that in  $0.44M_\odot$  case, as Figures 2.15 and 2.17 indicate. Moreover, the former precession is about twice faster than the latter (precession period is 292.6 and 581.2 days, respectively). Here assuming that the precession frequency in  $0.44M_\odot$  case is denoted as  $\dot{\Omega}$ , then the equivalent in  $0.34M_\odot$  case becomes around  $2\dot{\Omega}$ . This might suggest that other solutions with precession frequency  $3\dot{\Omega}$ ,  $4\dot{\Omega}$ ,  $5\dot{\Omega}$ ... could be also possible as solutions that satisfactorily reproduce both 2009 and 2010 observational data, as long as they can connect 2009 and 2010 observations in a self-consistent way through the precession. The only two-time transit observations are not enough to disentangle this degeneracy, thus the future observations are now necessary.

## 2.4 Validity of the spin-orbit synchronous condition in Barnes et al. (2013)

As shown in the first section of this chapter, the planetary orbital period is well constrained to be around 0.448413 days (van Eyken et al. 2012). On the other hand, the stellar rotational period is only weakly constrained ( $P_{\text{rot}} < 0.671$  days). In order for the star

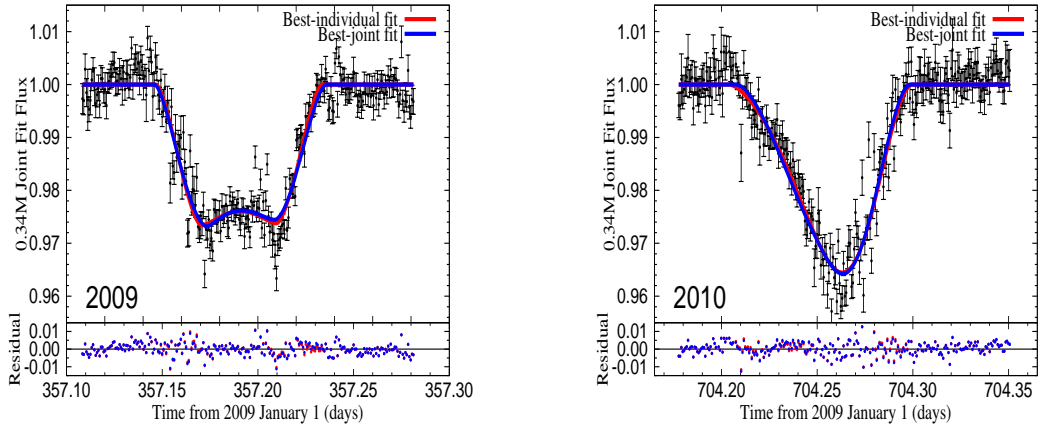


Figure 2.14: The best-fit 2009 (left) and 2010 (right) light curves from the 2009-2010 joint analysis for  $M_{\star} = 0.34M_{\odot}$  (blue lines). The best-fit from 2009 and 2010 individual fits are denoted as the red lines for comparison. Residuals for each plot are supplemented at the bottom panels.

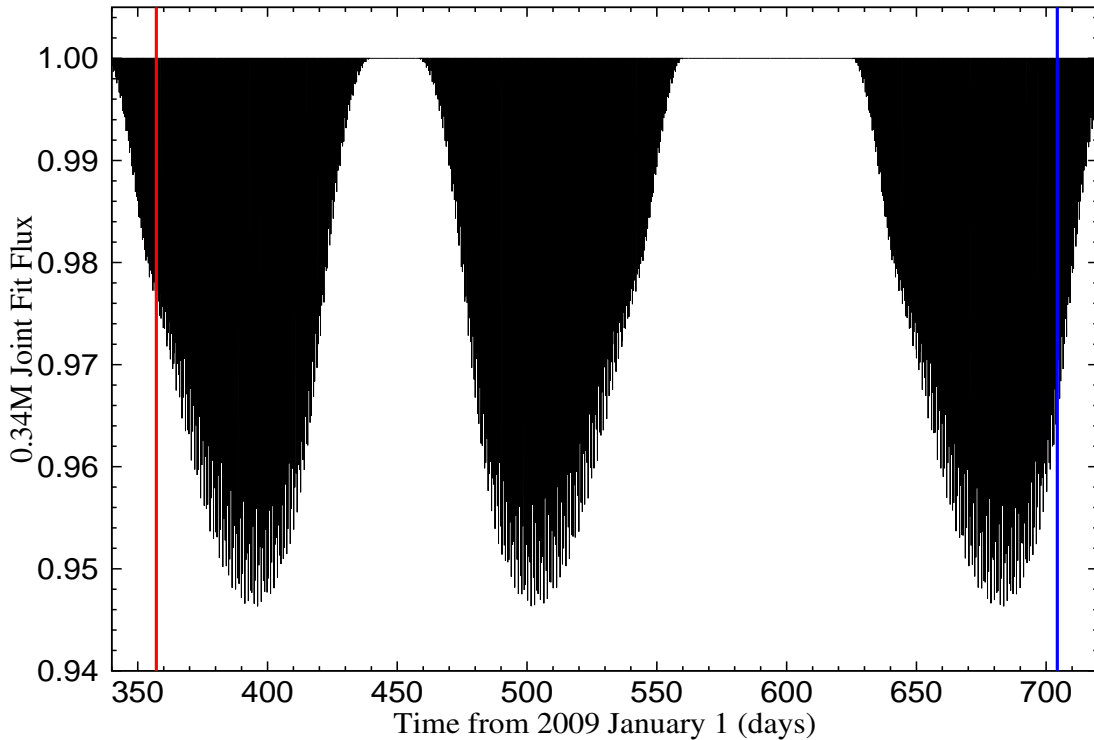


Figure 2.15: The predicted time evolution of the transit light curve from 2009 to 2010 with best-joint-fit parameters for  $M_{\star} = 0.34M_{\odot}$ . The epochs of 2009 and 2010 observation correspond to the colored vertical lines, red and blue, respectively.

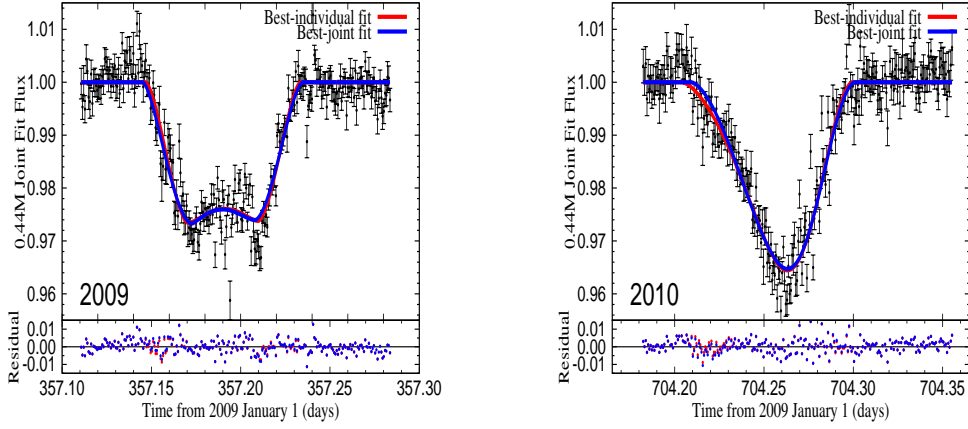


Figure 2.16: Same as Figure 2.14, but for  $M_{\star} = 0.44M_{\odot}$ .

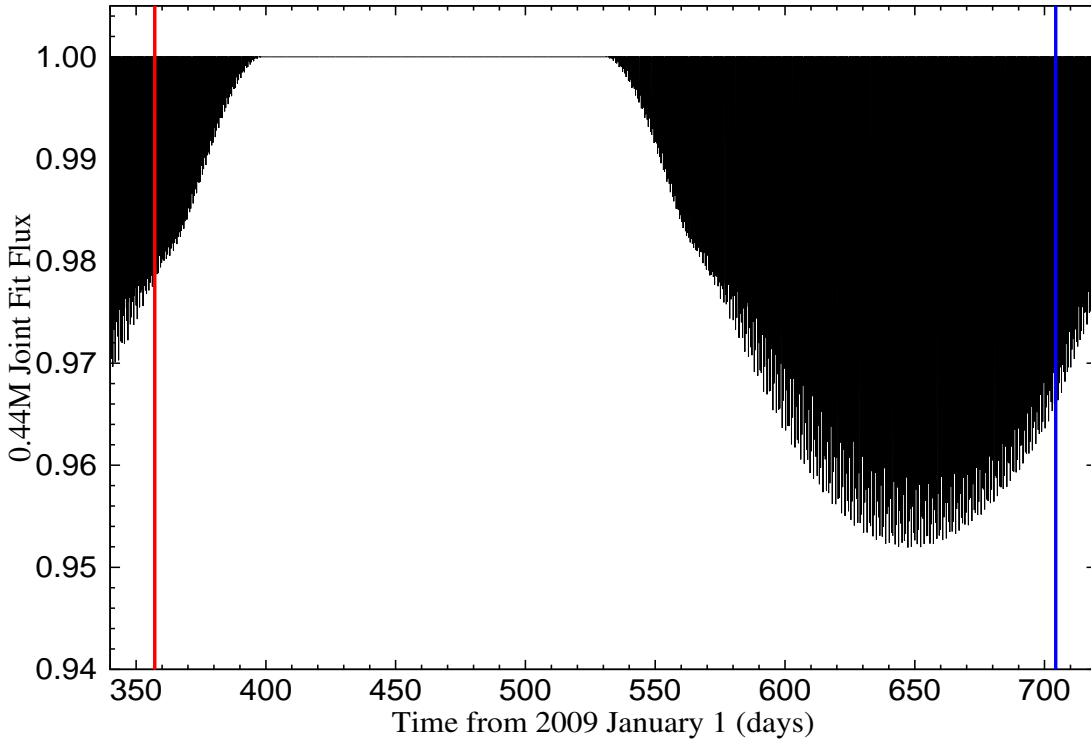


Figure 2.17: Same as Figure 2.15, but for  $M_{\star} = 0.44M_{\odot}$ .

to be gravitationally bounded,  $P_{\text{rot}}$  should be longer than  $\sim 0.2$  days. Instead of treating  $P_{\text{rot}}$  as a fitting parameter, B13 assumed that PTFO 8-8695 system is under the spin-orbit synchronized state, which implies that stellar rotational period is identical to the planetary orbital period.

The reason why they adopted the synchronous condition is attributed to the fact that

van Eyken et al. (2012) found  $P_{\text{rot}} \sim 0.4481$  days by analysing the original “un-whitened” light curve with the Lomb-Scargle periodogram. The Lomb-Scargle periodogram is designed for finding periodic features in the light curves, which is thought to be capable of picking up the stellar rotational signal and determining its period uniquely. High level of stellar noise and effect of changing spot features unfortunately inhibit them from deriving the definitive value of stellar rotation period, leaving two fundamental peaks which are considered to be the candidates for the actual rotation period ( $0.4481 \pm 0.0022$  days and  $0.9985 \pm 0.0061$  days). The latter one is beyond the upper limit of the rotational period (0.671 days) and could be attributed to an artefact resulting from observing cadence since its value is close to 1.0 days. For that reason, the 0.4481 day signal appears to be the only likely stellar rotational period indicating that the star is co-rotating or near co-rotating with the companion orbit.

The most probable mechanism for such a spin-orbit synchronization is the tidal effect between the central star and orbiting planet. As explained in chapter 1, tidal effect makes (i) planetary semi-major axis damp, (ii) orbital eccentricity damp, (iii) stellar/planetary rotational frequency and orbital frequency synchronized and (iv) stellar equatorial plane and planetary orbital plane coplanar. It is important when examining the validity of the spin-orbit synchronous condition that effective time scales for those mechanisms (defined as  $t_a$ ,  $t_e$ ,  $t_\omega$  and  $t_\phi$ , respectively) are different.

The equilibrium tide model is a conventional tidal model and widely accepted (Eggleton et al. 1998, Correia et al. 2011). It predicts that the eccentricity damping occurs the most rapidly whereas other three mechanisms take place on the comparable time scales longer than that for eccentricity damping ( $t_e < t_a \sim t_\omega \sim t_\phi$ ). However, this prediction is obviously inconsistent with the recent observations reporting the large number of planetary systems where close-in planets have significantly misaligned orbit without suffering from orbital decay that leads to the infall of the planet into the star (Figure A.3 in Appendix A). This discrepancy between theoretical prediction and observational data could be reconciled by considering the stellar inertial waves in the convective layers that will be excited by one component of the tidal potential (Lai 2012, Rogers & Lin 2013 and Xue et al. 2014). This additional mechanism can reinforce the efficiency of the spin-orbit alignment and synchronization without affecting the time scale of the orbital decay ( $t_e < t_\omega \sim t_\phi < t_a$ ). Thus this mechanism supports the observational picture where large number of close-in exoplanets keep their misaligned orbits at the vicinity of their central stars. The important suggestion from this model is that it makes no difference for the time scale of spin-orbit alignment and synchronization ( $t_\omega \sim t_\phi$ ). Thus this indicates that aligned planets are to be spin-orbit synchronized. Therefore, tidal model does not favor the spin-orbit synchronized assumption on PTFO 8-8695 system in B13 where the planetary orbit retains significantly (or, even highly) misaligned ( $\phi \sim 70^\circ$ ) in spite of their spin-orbit synchronised state. B13 also pointed out the possibility that truly synchronous rotation might be difficult to be achieved under the condition of  $\phi \sim 70^\circ$ . In addition, they left the interpretation in van Eyken et al. (2012) that a strong peak in the photometrical periodogram corresponds to the stellar rotational period open to question. However, re-analysis to this PTFO 8-8695 system without spin-orbit synchronous condition has never

been performed until today. Because the synchronous condition is unlikely to hold in reality, we drop it and repeat the fit of the 2009 and 2010 transit light curves of PTF0 8-8695.

In the following data analysis, planetary orbital eccentricity  $e$  is always assumed to be zero following B13. This assumption is supported by the tidal theory that predicts that a close-in planet acquires the circular orbit on faster time scale than those for any other dynamical rotational and/or orbital evolutions. The formulae in the following chapters include eccentricity  $e$  explicitly, but it is just for the the application of the precession model to other planetary systems which have the planets with eccentric orbits.

# Chapter 3

## Basic Equations for the Star-Planet Nodal Precession

### 3.1 Lagrange's planetary equations for the analytic formulae of the nodal precession

The nodal precession of the system is described by equation of motion (EOM) of the system which consists of the central star and orbiting planet with finite size (not point-mass). The EOM consists of four differential equations for (i) planetary position vector  $\mathbf{r}$  (equation D.50), (ii) planetary momentum vector  $\mathbf{p}$  (equation D.51), (iii) stellar spin angular momentum vector  $\mathbf{S}_\star$  (equation D.52) and (iv) planetary spin angular momentum vector  $\mathbf{S}_p$  (equation D.52). Along with the relation of  $\mathbf{L} = \mathbf{r} \times \mathbf{p}$ , we can pursue the time evolution of angular momentum vectors ( $\mathbf{S}_\star$  and  $\mathbf{L}$ ). The derivation and explicit form of EOM are all summarized in detail in Appendix D following Boué & Laskar (2006, 2009).

The calculation of the time evolution of  $\mathbf{S}_\star$  and  $\mathbf{L}$  accompanies the numerical integration of the differential vector equations. Although this is the most straightforward way to describe the behavior of the system, the following two assumptions make it possible to write down the analytic solutions for the nodal precession, which greatly reduces the computational cost.

1. Ignorance of the planetary spin angular momentum, which is smaller in magnitude than other two angular momentum vectors (stellar spin and planetary orbit) by several orders of magnitude. This procedure corresponds to the consideration of the planet as the point-mass.
2. Assumption that the stellar spin axis does not move with time.

While the second assumption is not always correct, one can generalize the result as we will show in section 3.3. So in this section, we assume just for simplicity that the stellar spin in practice does not move and only planetary orbital axis precess around the stellar spin axis. This kind of precession is the case for the system where the spin angular momentum of the central object is much greater in magnitude than the orbital angular momentum of

the surrounding body. Thus the spin of the central object almost stays constant and the orbital axis precesses around it. Such kind of the precession is known to occur within the solar system and its formulation are well established (for example, Murray & Dermott 1999). Popular examples include the precession of the Saturnian satellites around the Saturn (oblateness  $\sim 0.1$ ), and the precession of the International Space Station (ISS) around the Earth (oblateness  $\sim 0.003$ ).

The analytic formulation for such constant spin vector cases is well developed in the context of Lagrange's planetary equations (Murray & Dermott 1999):

$$\begin{aligned}
\frac{da}{dt} &= \frac{2}{na} \frac{\partial R}{\partial \sigma} \\
\frac{de}{dt} &= \frac{\eta^2}{na^2e} \frac{\partial R}{\partial \sigma} - \frac{\eta}{na^2e} \frac{\partial R}{\partial \omega} \\
\frac{di}{dt} &= \frac{\cot i}{na^2\eta} \frac{\partial R}{\partial \omega} - \frac{1}{na^2\eta \sin i} \frac{\partial R}{\partial \Omega} \\
\frac{d\sigma}{dt} &= -\frac{2}{na} \frac{\partial R}{\partial a} - \frac{\eta^2}{na^2e} \frac{\partial R}{\partial e} \\
\frac{d\omega}{dt} &= \frac{\eta}{na^2e} \frac{\partial R}{\partial e} - \frac{\cot i}{na^2\eta} \frac{\partial R}{\partial i} \\
\frac{d\Omega}{dt} &= \frac{1}{na^2\eta \sin i} \frac{\partial R}{\partial i},
\end{aligned} \tag{3.1}$$

where

$$\eta = \sqrt{1 - e^2}. \tag{3.2}$$

Here  $a$ ,  $e$ ,  $i$ ,  $\sigma$ ,  $\omega$  and  $\Omega$  is the orbital semi-major axis (the size of the orbit), orbital eccentricity (the shape of the orbit), orbital inclination (the direction of the orbit), initial mean anomaly (the planetary orbital phase at the fixed time), argument of periape (the direction of the orbit) and longitude of the ascending node (the direction of the orbit).  $a$  and  $e$  are easy to understand with Figure 3.1 and  $i$ ,  $\omega$  and  $\Omega$  are demonstrated in Figure 3.2. In Lagrange's planetary equations, planetary position is specified in terms of six orbital parameters. Careful investigation of the planetary equations reveals that all terms in the right hand sides take the form of  $R$  (called perturbation function) differentiated with respect to orbital parameters. Therefore, if  $R$  in the right hand side is constant (moreover, if  $R = 0$ ), all right hand side terms become zero, which means that all orbital parameters are time-invariant. This situation corresponds to the Keplerian motion in the Newtonian equation for the central star and the planet as point-masses. In general, however,  $R$  is a function of orbital parameters and orbital parameters necessarily evolve with time according to the planetary equations.

In the present case,  $R$  is given as a departure from the Newtonian potential due to the rotationally-induced bulge of the central star. Up to the fourth order of  $R_{\star, \text{eq}}/r$ , one can expand  $R$  (see Appendix D for details) as

$$R = -\frac{GM_{\star}}{r} \left[ J_2 \left( \frac{R_{\star, \text{eq}}}{r} \right)^2 P_2(\hat{\mathbf{r}} \cdot \hat{\mathbf{S}}_{\star}) + J_4 \left( \frac{R_{\star, \text{eq}}}{r} \right)^4 P_4(\hat{\mathbf{r}} \cdot \hat{\mathbf{S}}_{\star}) \right]. \tag{3.3}$$

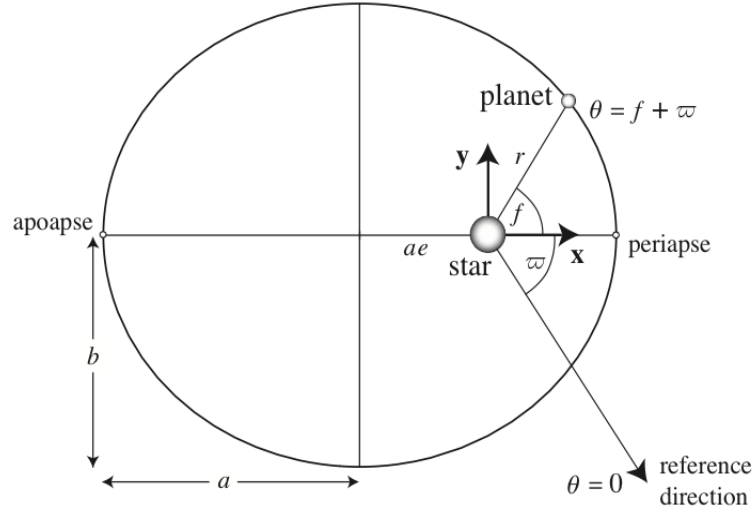


Figure 3.1: The geometry of the ellipse of semi-major axis  $a$  and eccentricity  $e$ . Figure taken from Murray & Correia (2011).

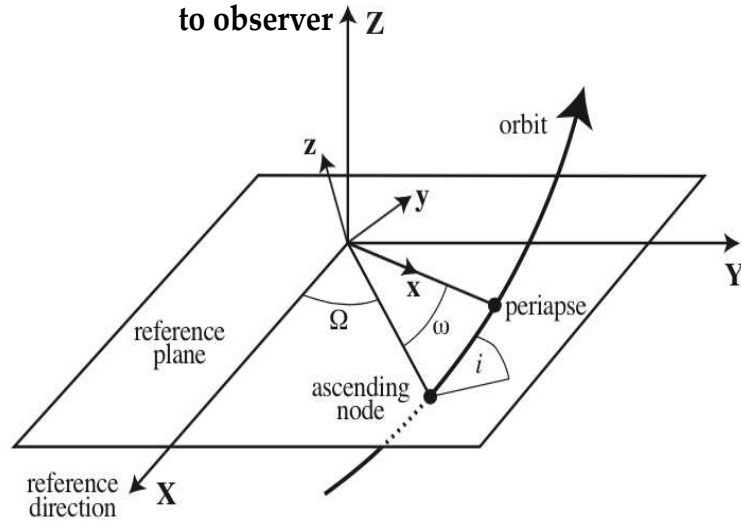


Figure 3.2: Three dimensional orbit of the planet. The star is located at the origin. The positive  $Z$ -direction is taken to point the observer and the  $X - Y$  plane is chosen as the sky plane. Figure modified from Murray & Correia (2011).

Here  $P_2$  and  $P_4$  are the second and fourth order Legendre polynomials, respectively (Table D.1), and  $J_n$  is the  $n$ -th order gravitational coefficient of the central star (equation D.39). The planetary position  $r$  is given as

$$r = \frac{a(1 - e^2)}{1 + e \cos(f + \omega)} \quad (3.4)$$

with the help of orbital parameters and true anomaly  $f$  (see Appendix B). The argument

$\hat{\mathbf{r}} \cdot \hat{\mathbf{S}}_\star$  is written as

$$\hat{\mathbf{r}} \cdot \hat{\mathbf{S}}_\star = \sin i \sin (f + \omega) \quad (3.5)$$

in the coordinates of Figure 3.2, where we choose the stellar spin vector ( $\hat{\mathbf{S}}_\star$ ) as the positive  $z$ -direction. It is possible to use stellar polar radius ( $R_{\star,\text{pol}}$ ) or stellar effective radius ( $R_{\star,\text{eff}}$ ; see chapter 5 for definition) instead of stellar equatorial radius ( $R_{\star,\text{eq}}$ ) in equation (3.3). Since the difference in the resulting values of  $R$  is at best the order of  $f^2$  (see next section) and usually negligible, however, B13 dropped  $\mathcal{O}(f^2)$  and higher order terms, and we follow them in this work. Therefore the consequent architecture of the precession with  $R_{\star,\text{eq}}$  in equation (3.3) is considered to be identical to those by  $R_{\star,\text{pol}}$  or  $R_{\star,\text{eff}}$  in equation (3.3) within the precision of the order of  $f$ . When considering the secular evolution of the system, it is convenient to use the orbital average of  $R$  instead of the form above:

$$\begin{aligned} \langle R \rangle &\equiv \int_0^{2\pi} R df \\ &= \frac{1}{2} n^2 a^2 \left[ \frac{3}{2} J_2 \left( \frac{R_{\star,\text{eq}}}{a} \right)^2 - \frac{9}{8} J_2^2 \left( \frac{R_{\star,\text{eq}}}{a} \right)^4 - \frac{15}{4} J_4 \left( \frac{R_{\star,\text{eq}}}{a} \right)^4 \right] e^2 \\ &\quad - \frac{1}{2} n^2 a^2 \left[ \frac{3}{2} J_2 \left( \frac{R_{\star,\text{eq}}}{a} \right)^2 - \frac{27}{8} J_2^2 \left( \frac{R_{\star,\text{eq}}}{a} \right)^4 - \frac{15}{4} J_4 \left( \frac{R_{\star,\text{eq}}}{a} \right)^4 \right] \sin^2 i. \end{aligned} \quad (3.6)$$

For the analytic expression of the precession in section 3.3, one needs the time derivative of the longitude of the ascending node ( $\dot{\Omega}$  in equation 3.1) which is specified as

$$\dot{\Omega} = -\frac{n}{\sqrt{1-e^2}} \cos i \left[ \frac{3}{2} J_2 \left( \frac{R_{\star,\text{eq}}}{a} \right)^2 - \frac{27}{8} J_2^2 \left( \frac{R_{\star,\text{eq}}}{a} \right)^4 - \frac{15}{4} J_4 \left( \frac{R_{\star,\text{eq}}}{a} \right)^4 \right]. \quad (3.7)$$

This physical quantity corresponds to the precession frequency with which the planetary orbital axis precesses around the stellar spin axis. Namely, it is the frequency with which the precessing axis is to sweep the cone around the precession central axis.

## 3.2 Analytic expressions for the gravitational coefficients with core-mantle model

Equation (3.7) requires explicit forms for  $J_2$  and  $J_4$ , which are generally given as equation (D.39). Hereafter, we neglect  $J_2^2$  and  $J_4$  terms following B13.  $J_2$  is given in terms of moments of inertia along with stellar principal axes,  $A_\star$  for the polar direction and  $C_\star$  for equatorial direction ( $C_\star > A_\star$ ), as

$$J_2 = \frac{C_\star - A_\star}{M_\star R_{\star,\text{eq}}^2}. \quad (3.8)$$

Here, the second Love number  $k_2$  (Love 1909) is defined so that  $J_2$  is written in terms of  $k_2$  as

$$J_2 = k_2 \frac{\omega_\star^2 R_{\star,\text{eq}}^3}{3GM_\star}, \quad (3.9)$$

which gives

$$k_2 = \frac{3G(C_\star - A_\star)}{\omega_\star^2 R_{\star,\text{eq}}^5}. \quad (3.10)$$

To evaluate them we have to know the internal mass profile of the central star (particularly, whether the central core exists or not), but the internal structure of the pre-main-sequence star such as PTFO 8-8695 is not well known today.

An alternative expression for  $J_2$  is available by assuming that the star has the internal core and surrounding convective envelope. By considering the extents of deformation of the core and envelope, and taking into account their mutual frictional force, an analytic form of  $J_2$  is obtained in terms of oblateness  $f$ , momentum of inertia coefficient  $\tilde{C}_\star$  and the radius ratio of the core to that of the envelope ( $R_{\text{core}}/R_{\text{env}}$ ) as

$$\begin{aligned} \frac{J_2}{f} = & \frac{2}{3} + \frac{\tilde{C}_\star - \frac{2}{5}(R_{\text{core}}/R_{\text{env}})^2}{1 - (R_{\text{core}}/R_{\text{env}})^2} \\ & + \frac{8 - 20(R_{\text{core}}/R_{\text{env}})^2 + 10\tilde{C}_\star[5(R_{\text{core}}/R_{\text{env}})^3 - 2]}{12[(R_{\text{core}}/R_{\text{env}})^5 - 1] + 15\tilde{C}_\star[2 - 5(R_{\text{core}}/R_{\text{env}})^3 + 3(R_{\text{core}}/R_{\text{env}})^5]}, \end{aligned} \quad (3.11)$$

which is known as the Darwin-Radau relation (Dermott 1979a,b).

The standard stellar evolution theory suggests that the T-Tauri star is at the stage before the development of the internal radiative core and then the PTFO 8-8695 is expected to be fully convective. If  $R_{\text{core}}/R_{\text{env}}$  is negligibly small (core-less assumption), the Darwin-Radau relation simply reduces to

$$J_2 = \tilde{C}_\star f. \quad (3.12)$$

In our analysis we employ moment of inertia coefficient of  $\tilde{C}_\star = 0.059$  which is the value estimated for the Sun following B13. However, the validity of employing this value is arguable because PTFO 8-8695 is a pre-main-sequence star whose internal structure is predicted to highly differ from that of the main-sequence star. Since the moment of inertia coefficient  $\tilde{C}_\star$  linearly affects the precession frequency (equation 3.15), it is possible for inaccurately-estimated  $\tilde{C}_\star$  to wholly alter the architecture of the precession and prevent us from characterizing PTFO 8-8695 system correctly.

In order to derive an analytic form of the oblateness  $f$ , we assume that the shape of the stellar surface is given by the equipotential surface. In this case,  $f$  is given in terms of the stellar mass  $M_\star$ , stellar equatorial radius  $R_{\star,\text{eq}}$  and angular frequency of the stellar rotation  $\omega_\star = 2\pi/P_{\text{rot}}$ . From the condition that the effective potential at the equator and that at the pole should be identical:

$$-\frac{GM_\star}{R_{\star,\text{pol}}} = -\frac{GM_\star}{R_{\star,\text{eq}}} - \frac{1}{2}\omega_\star^2 R_{\star,\text{eq}}^2, \quad (3.13)$$

the oblateness  $f$  is estimated as

$$f = \frac{R_{\star,\text{eq}} - R_{\star,\text{pol}}}{R_{\star,\text{eq}}} = \frac{\omega_{\star}^2 R_{\star,\text{eq}}^2 R_{\star,\text{pol}}}{2GM_{\star}} \xrightarrow{f^2 \rightarrow 0} \frac{\omega_{\star}^2 R_{\star,\text{eq}}^3}{2GM_{\star}}. \quad (3.14)$$

Both equations (3.9) and (3.12) are derived analytically but from different points of view. The former assumes that the rotating body is a perfect fluid body, while the latter assumes that the rotating body is fully convective and does not have a radiative core. With the conventional values of  $k_2 = 0.028$  and  $\tilde{C}_{\star} = 0.059$  for the main-sequence stars, equations (3.9) and (3.12) indicate that the latter one is three times larger than the former one, which imposes an additional puzzle. This inconsistency is quite influential in analyzing the data because  $J_2$  value linearly affects the precession frequency (equation 3.15). Due to the scarcity of the data and knowledge on the stellar internal profiles, however, we do not try to reconcile that inconsistency in this work but simply employ equation (3.12) instead of equation (3.9) following B13.

### 3.3 From single precession to mutual precession

The discussion above is focused on the precession of the planetary orbit around the fixed stellar spin axis. In the case of PTFO 8-8695, however, this fixed star assumption is far from appropriate since in that system the stellar rotational angular momentum ( $|\mathbf{S}_{\star}| = \tilde{C}_{\star} M_{\star} R_{\star,\text{eq}}^2 \omega_{\star}$ ) and planetary orbital angular momentum ( $|\mathbf{L}| = \beta \sqrt{\mu a (1 - e^2)}$ ) are comparable in magnitude within a factor of three. Thus both stellar spin axis and planetary orbital axis mutually precess around the total angular momentum vector ( $\mathbf{S}_{\star} + \mathbf{L}$ ). In this section we present the procedure necessary in order to apply the precession model derived above to this mutual precession state.

The qualitative explanation for the analytic form of the mutual precession frequency is as follows. The test calculations of the precession by equation (3.15) and by numerical integrations of EOM (see Appendix D) provide the identical time evolution of the spin and orbital axes, which validates the equation (3.15) quantitatively. To specify the mutual precession, we introduce not only the spin-orbit angle  $\phi$  but also  $\phi_{\star}$  and  $\phi_{\text{p}}$  as angles between the stellar spin axis and planetary orbital axis measured from the total angular momentum vector, respectively (of course, they satisfy  $\phi = \phi_{\star} + \phi_{\text{p}}$ ). Since the Lagrange's planetary equations neither accelerate nor decelerate the stellar spin and planetary orbital motion,  $\phi$ ,  $\phi_{\star}$  and  $\phi_{\text{p}}$  are all time-invariant otherwise the total angular momentum conservation law breaks.

When  $|\mathbf{S}_{\star}| \gg |\mathbf{L}|$ , the precessing  $\mathbf{L}$  traces a circle with a total circumference of  $2\pi |\mathbf{L}| \sin \phi$ . When  $|\mathbf{S}_{\star}| \sim |\mathbf{L}|$ , however,  $|\mathbf{L}|$  traverse a distance of  $2\pi |\mathbf{L}| \sin \phi_{\text{p}}$ . Thus the precession frequency changes by a factor of  $\frac{\sin \phi}{\sin \phi_{\text{p}}}$ . By renaming the precession frequency derived above as  $\dot{\Omega}_{\text{p}}$ , therefore, the frequency of the mutual precession  $\dot{\Omega}$  is written as

$$\dot{\Omega} = \dot{\Omega}_{\text{p}} \frac{\sin \phi}{\sin \phi_{\text{p}}} = -\frac{n}{\sqrt{1 - e^2}} \cos \phi \left[ \frac{3}{2} J_2 \left( \frac{R_{\star,\text{eq}}}{a} \right)^2 \right] \frac{\sin \phi}{\sin \phi_{\text{p}}}. \quad (3.15)$$

If  $\phi < 90^\circ$ , the factor  $\frac{\sin \phi}{\sin \phi_p}$  increases the frequency of the precession. In the case of retrograde orbit ( $90^\circ < \phi < 180^\circ$ ), on the other hand, it is possible to have  $\sin \phi_p > \sin \phi$ , which decreases the mutual precession frequency.

One can analytic estimate a precession period ( $P_{\dot{\Omega}}$ ) from equation (3.15):

$$P_{\dot{\Omega}} = \left| \frac{2\pi}{\dot{\Omega}} \right| = \left| \frac{4\pi}{3} \frac{1}{J_2} \frac{\sqrt{1-e^2}}{n} \left( \frac{a}{R_{\star,eq}} \right)^2 \frac{\sin \phi_p}{\sin \phi \cos \phi} \right| \quad (3.16)$$

$$\propto M_{\star}^{5/3} R_{\star,eq}^{-5} \omega_{\star}^{-2} n^{-7/3} \sin \phi_p (\sin 2\phi)^{-1}. \quad (3.17)$$

This formula enables us to give a simple estimation for the dependence of the precession period on the system parameters. For example, precession period is inversely proportional to the gravitational coefficient  $J_2$ , which indicates that larger extent of the rotational deformation triggers the faster precession. The dependence of  $(a/R_{\star,eq})^2$  implies that a more distant planet leads to slower precession because the mutual torque between star and planet becomes weaker as the planet is located in a distant orbit. In addition, the dependence on the spin-orbit angle  $\phi$  ( $P_{\dot{\Omega}} \propto (\sin 2\phi)^{-1}$ ) provides fairly interesting results. When anything else being the same, the precession becomes fastest for  $\phi = 45^\circ$ . Moreover, the precession is found to take infinite period when  $\phi = 90^\circ$ , which points out that the precession never takes place in such a polar orbit. In the case of polar orbit, therefore, the mutual torque between the star and planet is unable to alter the directions of stellar spin axis and planetary orbital axis. This is why the precession with angular parameters from the 2009 individual fitting by B13 was extremely slow since it has  $\phi = 89^\circ.1$  (Figures 2.11 and 2.13 for comparison).

### 3.4 Relation of the angular momentum vectors in the invariant frame and the sky frame

With the analytic formulae for precession frequency in equation (3.15), we write down the full-analytic form of the nodal precession, both in the invariant frame and in the sky frame.

First, we adopt the invariant frame (Figure 3.3) with total angular momentum vector along with the positive direction of  $y$ -axis and estimate the analytic form of  $\mathbf{S}_{\star}$  and  $\mathbf{L}$ :

$$\hat{\mathbf{S}}_{\star} = \begin{pmatrix} \sin \phi_{\star} \sin (\dot{\Omega}t + \alpha) \\ \cos \phi_{\star} \\ \sin \phi_{\star} \cos (\dot{\Omega}t + \alpha) \end{pmatrix}, \hat{\mathbf{L}} = \begin{pmatrix} \sin \phi_p \sin (\dot{\Omega}t + \alpha + \pi) \\ \cos \phi_p \\ \sin \phi_p \cos (\dot{\Omega}t + \alpha + \pi) \end{pmatrix}, \quad (3.18)$$

where  $\alpha$  is the initial azimuthal phase to be determined later. Note that  $\hat{\mathbf{S}}_{\star}$  always resides at the opposite side of  $\hat{\mathbf{L}}$  with respect to the total angular momentum vector.

The calculation of the stellar flux in chapter 4 is easier in the sky frame. The sky frame here is defined as the time-invariant frame where the observer resides the positive  $z$ -direction and the stellar spin axis projected onto the sky plane ( $x$ - $y$  plane) is along with

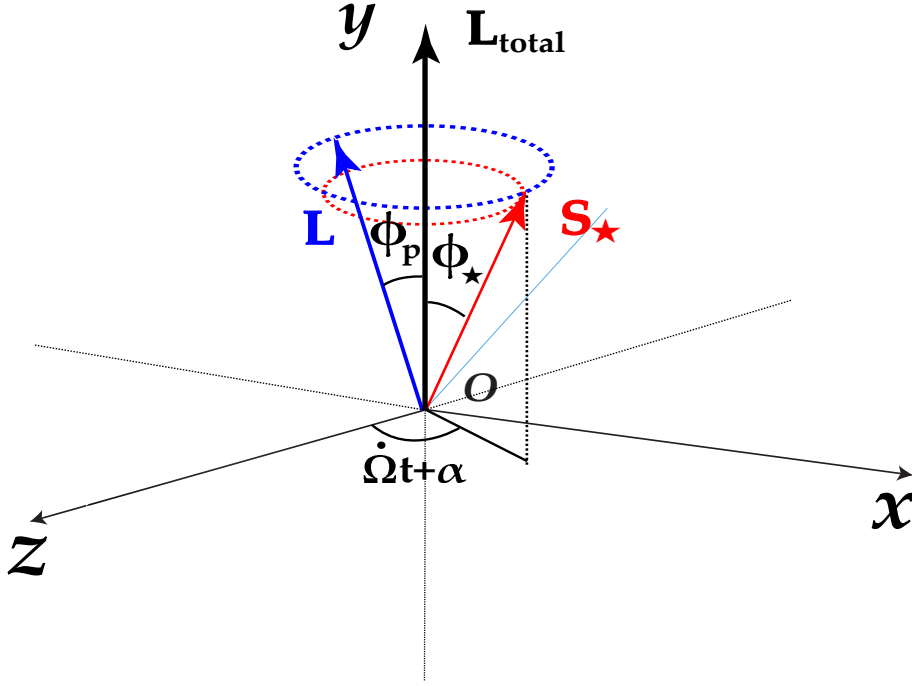


Figure 3.3: The geometrical configuration of stellar spin axis  $\mathbf{S}_*$  and planetary orbital axis  $\mathbf{L}$  in the invariant frame with total angular momentum vector  $\mathbf{L}_{\text{total}}$  along with the positive  $y$ -axis. Both precessing axes are specified with  $\phi_*$ ,  $\phi_p$  and  $\alpha$ .

the positive  $y$ -direction at initial time ( $\hat{\mathbf{S}}_{*,x} = 0$  at initial time). Since the total angular momentum vector is time-invariant in this frame, the stellar spin axis deviates from the  $y$ -axis as time proceeds (Figure 3.4). We begin with the derivation of the analytic form of total angular momentum vector in the sky frame. With the aid of three orbital parameters ( $i_{\text{orb}}$ ,  $\Omega$ ,  $i_*$ ) introduced in chapter 2,  $\mathbf{L}_{\text{total}}$  is given in the sky frame as

$$\begin{aligned}
 \mathbf{L}_{\text{total}} &= \mathbf{S}_* + \mathbf{L} \\
 &= |\mathbf{S}_*| \begin{pmatrix} 0 \\ \sin i_* \\ \cos i_* \end{pmatrix} + |\mathbf{L}| \begin{pmatrix} \sin i_{\text{orb}} \sin \Omega \\ -\sin i_{\text{orb}} \cos \Omega \\ \cos i_{\text{orb}} \end{pmatrix} \\
 &\equiv |\mathbf{L}_{\text{total}}| \begin{pmatrix} \sin \beta \sin \gamma \\ \cos \beta \\ \sin \beta \cos \gamma \end{pmatrix}, \tag{3.19}
 \end{aligned}$$

where  $\beta$  and  $\gamma$  are the polar and azimuthal angle measured in the sky frame, respectively (Figure 3.4), and are time-invariant because total angular momentum vector is time-invariant. Therefore they are written in terms of  $(i_{\text{orb}}, \Omega, i_*)$  as

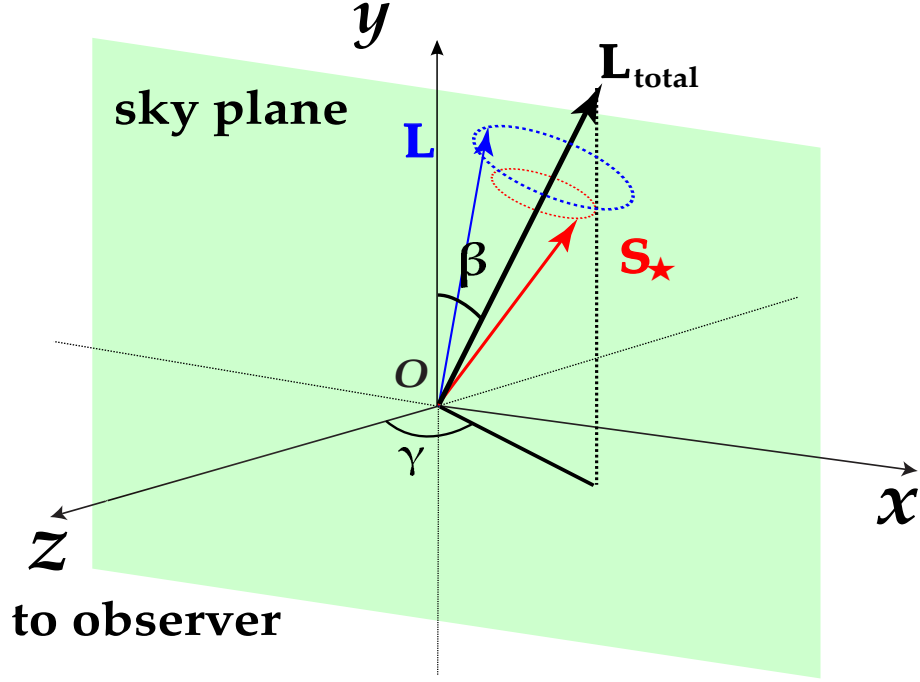


Figure 3.4: The geometrical configuration of stellar spin axis  $\mathbf{S}_\star$  and planetary orbital axis  $\mathbf{L}$  in the sky frame with positive  $z$ -direction pointing toward the observer. The precessing axis ( $\mathbf{L}_{\text{total}}$ ) is specified with  $\beta$  and  $\gamma$ .

$$\beta = \cos^{-1}(\hat{\mathbf{L}}_{\text{total},y}) = \cos^{-1}\left(\frac{|\mathbf{S}_\star| \sin i_\star - |\mathbf{L}| \sin i_{\text{orb}} \cos \Omega}{|\mathbf{L}_{\text{total}}|}\right) \quad (3.20)$$

$$\gamma = \tan^{-1}\left(\frac{\hat{\mathbf{L}}_{\text{total},x}}{\hat{\mathbf{L}}_{\text{total},z}}\right) = \tan^{-1}\left(\frac{|\mathbf{L}| \sin i_{\text{orb}} \sin \Omega}{|\mathbf{S}_\star| \cos i_\star + |\mathbf{L}| \cos i_\star}\right). \quad (3.21)$$

The rotation of the system about  $x$ -axis in the invariant frame by  $\beta$ , followed by the rotation about  $y$ -axis by  $\gamma$  can convert the analytic expression (3.18) into those represented in the sky frame as

$$\begin{pmatrix} \mathbf{S}_\star \\ \mathbf{L} \end{pmatrix}_{\text{sky frame}} = R_y(\gamma)R_x(\beta) \begin{pmatrix} \mathbf{S}_\star \\ \mathbf{L} \end{pmatrix}_{\text{invariant frame}}, \quad (3.22)$$

where  $R_x$  and  $R_y$  are rotation matrices about  $x$  and  $y$ -axis, respectively; see equations (B.42) and (B.43).

It remains to determine the initial azimuthal phase  $\alpha$  in equation (3.18). Since the expression in the invariant frame and that in the sky frame should have a one-to-one correspondence,  $\alpha$  can be uniquely specified once  $i_{\text{orb}}$ ,  $\Omega$  and  $i_\star$  are given at the particular epoch  $t = t_0$ . Therefore, we should take  $\alpha$  which satisfies

$$\begin{pmatrix} \mathbf{S}_\star \\ \mathbf{L} \end{pmatrix}_{\text{invariant frame at } t=t_0} = R_x^{-1}(\beta)R_y^{-1}(\gamma) \begin{pmatrix} \mathbf{S}_\star \\ \mathbf{L} \end{pmatrix}_{\text{sky frame at } t=t_0}. \quad (3.23)$$

With  $\alpha$  determined by equation (3.23), equation (3.22) provides the directions of  $\mathbf{S}_\star$  and  $\mathbf{L}$  at any given time  $t$ .

Finally, we need to convert the analytically-formulated angular momentum vectors in the sky plane (equation 3.22) into the angular parameters  $(i, \lambda, \psi)$  which are required for light curve model (see chapter 4 and 5) at any given epoch of the precession. From equations (2.2) and (2.3),  $i$  and  $\psi$  are evaluated as

$$\begin{aligned}\psi &= \sin^{-1}(-\hat{\mathbf{S}}_{\star,z}) \\ i &= \cos^{-1}(-\hat{\mathbf{L}}_z).\end{aligned}\tag{3.24}$$

Note that the angle measured from the spin axis,  $\lambda$ , is not given by  $\lambda = \tan^{-1}(\hat{\mathbf{L}}_x/\hat{\mathbf{L}}_y)$  because the precession let  $\mathbf{S}_\star$  deviate from  $y$ -axis in the sky plane with time. Instead,  $\lambda$  is evaluated as the angle between the stellar spin axis and the planetary orbital axis projected onto the sky plane ( $\hat{\mathbf{S}}_{\star,\text{sp}}$  and  $\hat{\mathbf{L}}_{\text{sp}}$ ), as

$$\lambda = \cos^{-1}(\hat{\mathbf{S}}_{\star,\text{sp}} \cdot \hat{\mathbf{L}}_{\text{sp}}).\tag{3.25}$$

In conclusion, we obtain  $(i, \lambda, \psi)$  at any given time  $t$  as follows.

1. Calculate the stellar spin axis and planetary orbital axis in the invariant frame at the given time  $t$  following equation (3.18).
2. Convert them into the sky frame with equation (3.22).
3. Evaluate the angular parameters  $(i, \lambda, \psi)$  following equations (3.24) and (3.25).

# Chapter 4

## Light Curve modelling

### 4.1 General formula for the normalized flux

In this chapter, we explain the method to illustrate the transit light curve of the rotationally deformed and gravity darkened star, basically following Barnes (2009) with the help of Mandel & Agol (2002). The formulation and coding of the following models in this chapter were completed by Kento Masuda, who is one of the collaborators of this work. The rapid stellar rotation distorts the stellar disk in the sky plane from a circle, and the gravity darkening effect causes its surface temperature to exhibit the additional dependence on the stellar latitude. As for the orbiting planet, we here neglect its oblateness induced by the planetary rotation, which means that the planet is assumed to be spherical body and complete circle in the sky plane. The stellar flux  $F(t)$  is described as the polar and azimuthal integrations of the stellar intensity  $I_\lambda(r, \theta)$  over the whole stellar disk as,

$$\begin{aligned} F(t) &= \frac{F_0 - F_{\text{blocked}}(t)}{F_0} \\ F_0 &= \int_{\text{stellar disk}} I_\lambda(x, y) dx dy = \int_{\left(\frac{x}{R_{\star, \text{eq}}}\right)^2 + \left(\frac{y}{R_{\star, \text{pol}}}\right)^2 = 1} I_\lambda(r, \theta) r dr d\theta \\ F_{\text{blocked}}(t) &= \int_{\text{stellar disk}} \Gamma(x, y, t) I_\lambda(x, y) dx dy = \int_{\left(\frac{x}{R_{\star, \text{eq}}}\right)^2 + \left(\frac{y}{R_{\star, \text{pol}}}\right)^2 = 1} \Gamma(r, \theta, t) I_\lambda(r, \theta) r dr d\theta, \end{aligned} \tag{4.1}$$

where  $F_0$  is the out-of-transit stellar flux and  $F_{\text{blocked}}(t)$  is the stellar flux from the portion of the stellar disk where transiting planet occults (Figure 4.1). Here  $R_{\star, \text{eq}}$  is the stellar equatorial radius,  $r$  is the radius measured from the center of the stellar disk and  $\theta$  is measured counterclockwise from the  $x$ -axis in the sky plane.  $y$ -axis is defined so that the stellar spin axis projected onto the sky plane is to coincide with the positive  $y$ -axis and  $x$ -axis is given by the rotation of  $y$ -axis about the line of sight by  $90^\circ$ .  $I_\lambda(r, \theta)$  is the stellar intensity at the wavelength of  $\lambda$  at the point  $(r, \theta)$  and  $\Gamma(r, \theta, t) = 1$  when the planet is positioned at  $(r, \theta)$  at time  $t$ , otherwise  $\Gamma(r, \theta, t) = 0$ . Then time-variable stellar flux  $F(t)$  is given by the subtraction of the  $F_{\text{blocked}}$  from  $F_0$ , followed by the normalization with  $F_0$ .

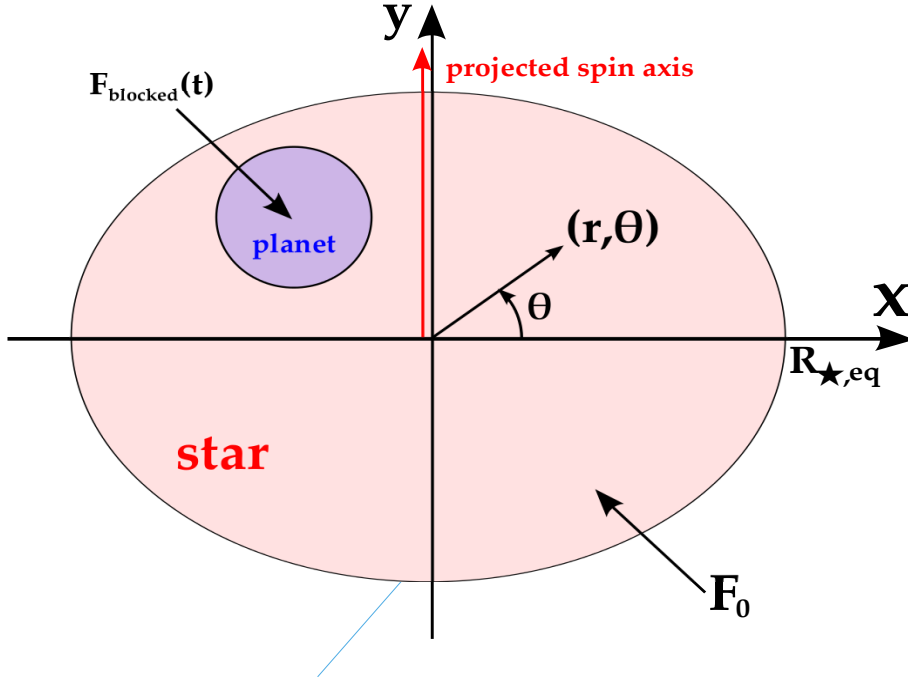


Figure 4.1: Schematic illustration of  $F_0$  and  $F_{\text{blocked}}(t)$ . The stellar disk is denoted as the red region, and the planetary disk is blue.  $y$ -axis is chosen to be parallel with the projected stellar spin axis.  $\theta$  is measured counter-clockwise from the positive  $x$ -direction.

## 4.2 Effective oblateness $f_{\text{eff}}$

In fact, the radial and angular integrations in equations (4.1) require the *effective* oblateness ( $f_{\text{eff}}$ ), the oblateness of the stellar disk in the sky plane, rather than the *true* oblateness  $f$ . And the effective oblateness  $f_{\text{eff}}$  depends on the direction of the stellar spin axis. Thus assuming the rotationally deformed star as a MacLaurin spheroid whose elongated two principal axes (equatorial radius) are longer than the remaining one (polar radius), the effective oblateness  $f_{\text{eff}}$  is given in terms of stellar obliquity  $\psi$  as

$$f_{\text{eff}} = 1 - \sqrt{(1 - f)^2 \cos^2 \psi + \sin^2 \psi}. \quad (4.2)$$

For example, when seen by edge-on ( $\psi = 0^\circ$ ), effective oblateness  $f_{\text{eff}}$  coincides with true oblateness  $f$ . When seen by pole-on ( $\psi = \pm 90^\circ$ ), however, the star looks like a circle form in the sky plane ( $f_{\text{eff}} = 0$ ) even if it is rotationally deformed.

The derivation of equation (4.2) is not simple. For the given  $x$  and  $y$  values in the stellar disk in the sky plane,  $z$  coordinate, the departure from the sky plane is to be uniquely estimated. This is because there is the geometrical constraint that  $z$  value should confirm the surface of the oblate star with given  $x$ ,  $y$ ,  $R_{\star, \text{eq}}$  (stellar equatorial radius) and  $f$ . In the case of the spherical star, this relation is  $x^2 + y^2 + z^2 = R^2$ . Here it is useful to prepare the new Cartesian coordinates ( $x_0, y_0, z_0$  system) which have the same origin with  $x, y, z$  system, at the center of the star (see Figure 4.2). This new coordinates are designed from

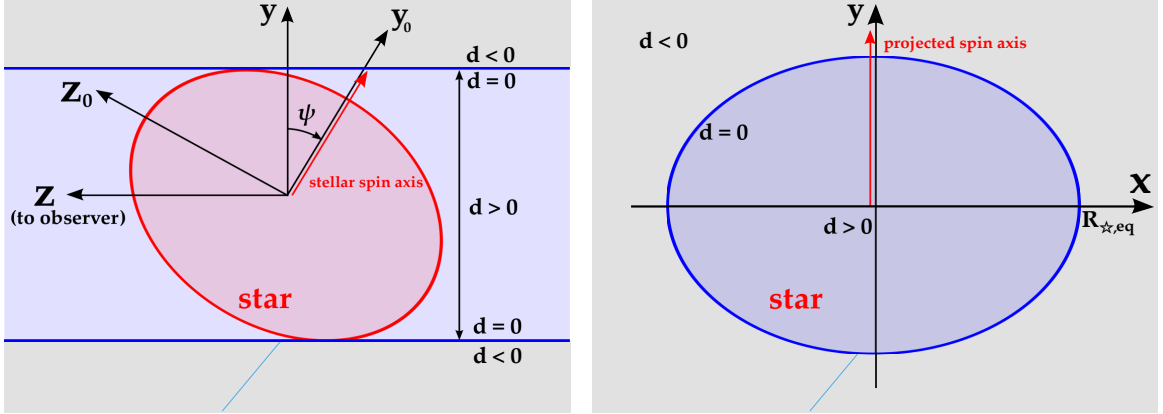


Figure 4.2: Schematic illustration of  $(x_0, y_0, z_0)$  coordinates and the meaning of the discriminant  $d$  in  $y - z$  plane (left) and in  $x - y$  plane (right).  $y_0$ -axis is chosen to be aligned with the stellar spin axis. When  $d > 0$ , the line of sight has two intersections with the star (light blue region) while only one intersection for  $d = 0$  (blue lines). When  $d < 0$ , the line of sight never crosses with the star (light gray region).

the rotation of  $x, y, z$  coordinates about  $x$ -axis by the angle  $\psi$  so that  $y_0$ -axis coincides with the stellar rotational axis, which gives

$$\begin{aligned} x_0 &= x \\ y_0 &= y \cos \psi - z \sin \psi \\ z_0 &= y \sin \psi + z \cos \psi \end{aligned} \quad (4.3)$$

and

$$x_0^2 + \frac{y_0^2}{(1-f)^2} + z_0^2 = R_{*,\text{eq}}^2. \quad (4.4)$$

The combining of equations (4.3) and (4.4) gives the analytic expression:

$$z_{\pm} = \frac{2y(1 - (1-f)^2) \sin \psi \cos \psi \pm \sqrt{d}}{2((1-f)^2 \cos^2 \psi + \sin^2 \psi)}, \quad (4.5)$$

where the “discriminant”  $d$  is specified as

$$\begin{aligned} d \equiv & 4y^2(1 - (1-f)^2)^2 \sin^2 \psi \cos^2 \psi \\ & - 4((\cos^2 \psi(1-f)^2 + \sin^2 \psi)((y^2 \sin^2 \psi - R_{*,\text{eq}}^2 + x^2)(1-f)^2 + y^2 \cos^2 \psi)). \end{aligned} \quad (4.6)$$

In equation (4.5),  $z_+$  corresponds to the stellar surface with positive  $z$  value (first interception of the line of sight with the photosphere). Then  $z_-$  denotes the stellar surface with negative  $z$  value, representing the second interception of the line of sight with the photosphere which is invisible from the observer. Then, the relation among effective oblateness, true oblateness and  $\psi$  (equation 4.2) is derived by selecting the discriminant  $d$  equal to

zero. In that case the line of sight intersects the star just once, which directly traces the contour of the stellar disk in the sky plane (right panel in Figure 4.2).

In order to make the analytic forms for the integrations simpler, the following formulation is performed in the “primed” coordinates:

$$x' = x \quad (4.7)$$

$$y' = \frac{y}{1 - f_{\text{eff}}}, \quad (4.8)$$

where the stellar disk is reduced to the circle in the sky plane. Instead, the planet gets to deviate from the circle and take elongated form to the  $y$ -direction, namely, an ellipse. In this coordinates  $r'$  and  $\theta'$  are defined as  $r' = \sqrt{x'^2 + y'^2}$  and  $\theta' = \tan^{-1}(y'/x')$ , respectively.

### 4.3 Flux from the oblate star

With the help of the primed coordinates, equations (4.1) can be rewritten as

$$\begin{aligned} F_0 &= \int_{-R_{\star,\text{eq}}}^{+R_{\star,\text{eq}}} dx \int_{-(1-f_{\text{eff}})\sqrt{R_{\star,\text{eq}}^2-x^2}}^{+(1-f_{\text{eff}})\sqrt{R_{\star,\text{eq}}^2-x^2}} dy I_{\lambda}(x, y) \\ &= (1 - f_{\text{eff}}) \int_{-R_{\star,\text{eq}}}^{+R_{\star,\text{eq}}} dx' \int_{-\sqrt{R_{\star,\text{eq}}^2-x'^2}}^{+\sqrt{R_{\star,\text{eq}}^2-x'^2}} dy' I_{\lambda}(x', (1 - f_{\text{eff}})y') \\ &= (1 - f_{\text{eff}}) \int_0^{R_{\star,\text{eq}}} \int_0^{2\pi} I_{\lambda}(r', \theta') r' dr' d\theta', \end{aligned} \quad (4.9)$$

and similarly,

$$F_{\text{blocked}}(t) = (1 - f_{\text{eff}}) \int_0^{R_{\star,\text{eq}}} \int_0^{2\pi} \Gamma(r', \theta', t) I_{\lambda}(r', \theta') r' dr' d\theta', \quad (4.10)$$

where  $r' = \sqrt{x'^2 + (1 - f_{\text{eff}})^2 y'^2}$  and  $\theta' = \tan^{-1}((1 - f_{\text{eff}})y'/x')$ . The  $(1 - f_{\text{eff}})$  factor in above expressions eventually drops when calculating the normalized flux  $F(t) = (F_0 - F_{\text{blocked}}(t))/F_0$  since it appears on both numerator and denominator.

### 4.4 Stellar intensity $I_{\lambda}(r', \theta')$

This section is devoted to specify the explicit form of the stellar intensity  $I_{\lambda}(r', \theta')$  by taking into account the physical phenomena that are expected to take place in the actual stars. We assume that the stellar disk is blackbody  $B_{\lambda}(T)$  but with the limb darkening factor  $L(r', \theta')$ :

$$I_{\lambda}(r', \theta') = B_{\lambda}(T(r', \theta'))L(r', \theta'), \quad (4.11)$$

with

$$B_\lambda(T(r', \theta')) = \frac{2hc^2}{\lambda^5} \frac{1}{\exp(\frac{hc}{\lambda k_B T}) - 1} \quad (4.12)$$

and

$$L(r', \theta') = 1 - u_1(1 - \mu) - u_2(1 - \mu)^2. \quad (4.13)$$

Here  $\mu$  is the cosine of the angle between the stellar surface gravity  $\hat{\mathbf{g}}$  and the line of sight  $\hat{\mathbf{z}}$ . In  $(x_0, y_0, z_0)$  coordinates, the line of sight vector  $\hat{\mathbf{z}}$  is given by

$$\hat{\mathbf{z}} = (0, -\sin \psi, \cos \psi). \quad (4.14)$$

For the purpose of specifying  $\hat{\mathbf{g}}$ , we start with the potential  $\Psi$  outside the star with the rotational frequency  $\omega_\star$  as

$$\Psi = -\frac{GM_\star}{r} - \frac{1}{2}\omega_\star^2 r^2 \cos^2 \theta, \quad (4.15)$$

where  $r$  is the distance measured from the stellar center and  $\theta$  is the stellar latitude. Note here that although the centrifugal force causes the star to be deformed, the gravitational potential (the first term in the right-hand side in equation 4.15) is assumed to be the spherical one. Namely, the effect of rotation appears only through the centrifugal potential, the second term in the right-hand side in equation (4.15). The more general expressions for the gravitational potential outside the rotationally-deformed star are summarized in Appendix D. In the  $(x_0, y_0, z_0)$  coordinates, equation (4.15) becomes

$$\Psi = -\frac{GM_\star}{\sqrt{x_0^2 + y_0^2 + z_0^2}} - \frac{1}{2}\omega_\star^2(x_0^2 + z_0^2). \quad (4.16)$$

Therefore, the effective force at the stellar surface  $(x_0, y_0, z_0)$  becomes

$$\mathbf{g} = -\frac{GM_\star}{R^2}\hat{\mathbf{r}} + \omega_\star^2 R_\perp \hat{\mathbf{r}}_\perp = -\frac{GM_\star}{R^2} \left( \hat{\mathbf{r}} - \frac{\omega_\star^2 R^2 R_\perp}{GM_\star} \hat{\mathbf{r}}_\perp \right), \quad (4.17)$$

where  $R = \sqrt{x_0^2 + y_0^2 + z_0^2}$ ,  $\hat{\mathbf{r}} = (x_0, y_0, z_0)/R$ ,  $R_\perp = \sqrt{x_0^2 + z_0^2}$  (distance from the stellar rotational axis) and  $\hat{\mathbf{r}}_\perp = (x_0, 0, z_0)/R_\perp$  (unit vector from the stellar rotational axis). Since  $\hat{\mathbf{r}} \cdot \hat{\mathbf{r}}_\perp = R_\perp/R$ , the norm of equation (4.17) becomes

$$\begin{aligned} g(r', \theta') &= \frac{GM_\star}{R^2} \sqrt{1 + \left( \frac{\omega_\star^2 R^2 R_\perp}{GM_\star} \right)^2 - \frac{2\omega_\star^2 R^2 R_\perp}{GM_\star} (\hat{\mathbf{r}} \cdot \hat{\mathbf{r}}_\perp)} \\ &= \frac{GM_\star}{R^2} \sqrt{1 + 4f\tilde{R}\tilde{R}_\perp^2 (f\tilde{R}^3 - 1)}, \end{aligned} \quad (4.18)$$

where  $f = \omega_\star^2 R_{\star, \text{eq}}^3 / 2GM_\star$  (equation 3.14),  $\tilde{R} \equiv R/R_{\star, \text{eq}}$  and  $\tilde{R}_\perp \equiv R_\perp/R_{\star, \text{eq}}$ . Finally, we find  $\mu$  as

$$\mu = -\hat{\mathbf{g}} \cdot \hat{\mathbf{z}} = \frac{1}{R\sqrt{1 + 4f\tilde{R}\tilde{R}_\perp^2 (f\tilde{R}^3 - 1)}} (-y_0 \sin \psi + z_0(1 - 2f\tilde{R}^3) \cos \psi). \quad (4.19)$$

Specifying equation (4.19) requires  $(x_0, y_0, z_0)$  which are related with  $(x, y, z)$  through equation (4.3). Further,  $(x, y, z)$  can be translated from  $(x, y) = (r' \cos \theta', (1 - f_{\text{eff}})r' \sin \theta')$  and equation (4.5). Therefore, one can evaluate equation (4.3) by  $r', \theta', \psi$  and  $f$ .

In addition to  $\mu$ ,  $u_1$  and  $u_2$  are also necessary to evaluate the equation (4.13). In general  $u_1$  and  $u_2$  are used in terms of the limb-darkening parameters  $c_1 = u_1 + u_2$  and  $c_2 = u_1 - u_2$  (see section 5.2 for the assumed values of  $c_1$  and  $c_2$ ).

As for the planck function (equation 4.12), simple manipulation below can translate it into more tractable form as

$$B_\lambda(T) = \frac{2hc^2}{\lambda^5} \frac{1}{\exp\left(\frac{hc}{\lambda k_B T}\right) - 1} = B_\lambda(T_{\text{pol}}) \frac{\exp(x(\lambda, T_{\text{pole}})) - 1}{\exp(x(\lambda, T)) - 1}, \quad (4.20)$$

where

$$x(\lambda, T) \equiv \frac{hc}{\lambda k_B T} = 2.397958702 \times \left(\frac{\lambda}{\mu\text{m}}\right)^{-1} \times \left(\frac{T}{6000\text{K}}\right)^{-1}. \quad (4.21)$$

## 4.5 Effective temperature $T_{\text{eff}}(r', \theta')$

The temperature profile on the stellar disk is required to calculate the total stellar flux. In this analysis, we adopt the von Zeipel model (see for example von Zeipel 1924, Maeder 1999 and Maeder 2009) following B13:

$$\frac{T_{\text{eff}}(r', \theta')}{T_{\text{pol}}} = \left(\frac{g(r', \theta')}{g_{\text{pol}}}\right)^{\beta_{\text{GD}}}, \quad (4.22)$$

where  $T_{\text{pol}}$  and  $g_{\text{pol}}$  are the polar effective temperature and polar surface gravity, and  $\beta_{\text{GD}}$  is the gravity darkening parameter (fixed to the theoretical value of 0.25 in this work).  $g_{\text{pol}}$  is given by equation (4.18) with  $R_\perp = 0$  and  $R_{\star, \text{pol}} = (1 - f)R_{\star, \text{eq}}$ .  $(r', \theta')$  is related to  $(x, y, z)$  with  $(x, y) = (r' \cos \theta', (1 - f_{\text{eff}})r' \sin \theta')$  and equation (4.5), which in turn is converted to  $(x_0, y_0, z_0)$  with equation (4.3).

# Chapter 5

## Results and Discussion

### 5.1 Data reduction

The observational data are kindly provided by Prof. Julian van Eyken, one of the authors of B13, and identical to those used by B13; 11 reliable transits for 2009 observation and 6 reliable ones for 2010 observation as introduced in chapter 2. The effects of stellar activity, long term periodical fluctuation (for instance, due to spot modulation) and background noise are already removed and whitened (see Figures 2.1 and 2.2). In this section we describe procedures to construct the template light curves basically following B13. We use these template light curves to compare with the model light curves following the procedure in chapter 4. Since the 2009 and 2010 transits were taken monochromatically with wavelength of  $0.658\mu m$ , we fix the wavelength in equation (4.12) to  $0.658\mu m$  in all the following analyses. The data analysis proceeds as follows:

1. Phase-fold. Phase-fold is to make all transit light curves be piled up with the same orbital phase being located at the same position. The single light curve is left after this procedure. Figures 5.1 and 5.2 present the phase-folded transit light curves for 2009 and 2010 observation, respectively.
2. Clipping. During the orbital period of  $\sim 0.448413$  days (van Eyken et al. 2012), the transit actually lasts only for  $\sim 0.1$  days. Thus a major part of the phase-folded light curve corresponds to the out-of-transit phase. In order to reduce the number of the data points and following computational cost, we focus on the range of orbital phase from 15,000 s to 30,000 s (light gray regions in Figures 5.1 and 5.2).
3. Binning. All data points are combined into one-minute bins (Figure 5.3). All individual fits in the remaining of this thesis are performed with these 2009 and 2010 template light curves.
4. Positioning the 2009 and 2010 template light curves. The procedures 1 - 3 correspond to the long term averaging over 1.5 months for 2009 observation and 1 week for 2010 observation. Therefore, it is ambiguous to which transit the phase-folded, clipped, binned light curves correspond during the 2009 and 2010 observations. Thus

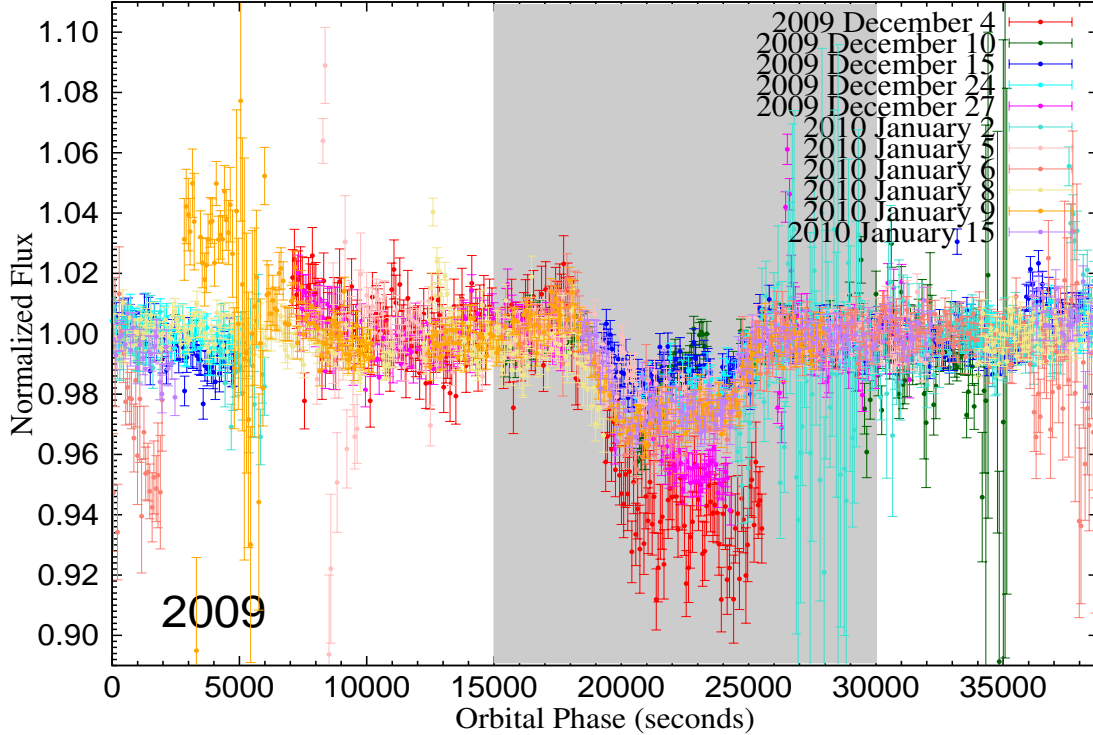


Figure 5.1: Phase-folded transit light curve for 11 reliable light curves in 2009 observation. Different colors show different days when transit was observed. We did not use all data points in the phase-folded data in this work, and light gray region denotes the clipped range for the following procedures.

we need to specify where both transit light curves should be placed, particularly with how long separation. Where both light curves should be placed, particularly with how long separation they should be placed, is one of the most important ambiguities in the current modelling. A difference in their mutual separation will be linearly reflected into the difference in the precession period (equation 3.17) that is sensitive on a variety of system parameters ( $n$ ,  $a$ ,  $R_*$ ,  $\phi$ ,  $\phi_p$ ,  $J_2$  and all variables included in  $J_2$ ). As shown in chapter 2, the individual fitting for 2009 and 2010 transit light curves in B13 provided the epochs of inferior conjunction (the epoch  $t_0$  which satisfies  $\omega + f = \pi/2$ ) of 30861700 s and 60848300 s, respectively. Their mutual separation turns out to correspond to 774-times transit period given that orbital period  $P$  is 0.448413 days as estimated in van Eyken et al. (2012). We follow them and place our 2009 and 2010 phase-folded, clipped, binned light curves so that they have a mutual separation of 774-times orbital period  $P$  (see Table 2.4; 0.448410 days for  $M_* = 0.34M_\odot$ , and 0.448413 days for  $M_* = 0.44M_\odot$ ). All joint fits in the remaining of this thesis are performed with this 2009-2010 combined template light curves.

The parameter fits are performed in the following way with the aid of the Levenberg-Marquardt algorithm. In this scheme, the values of parameters are modified repeatedly

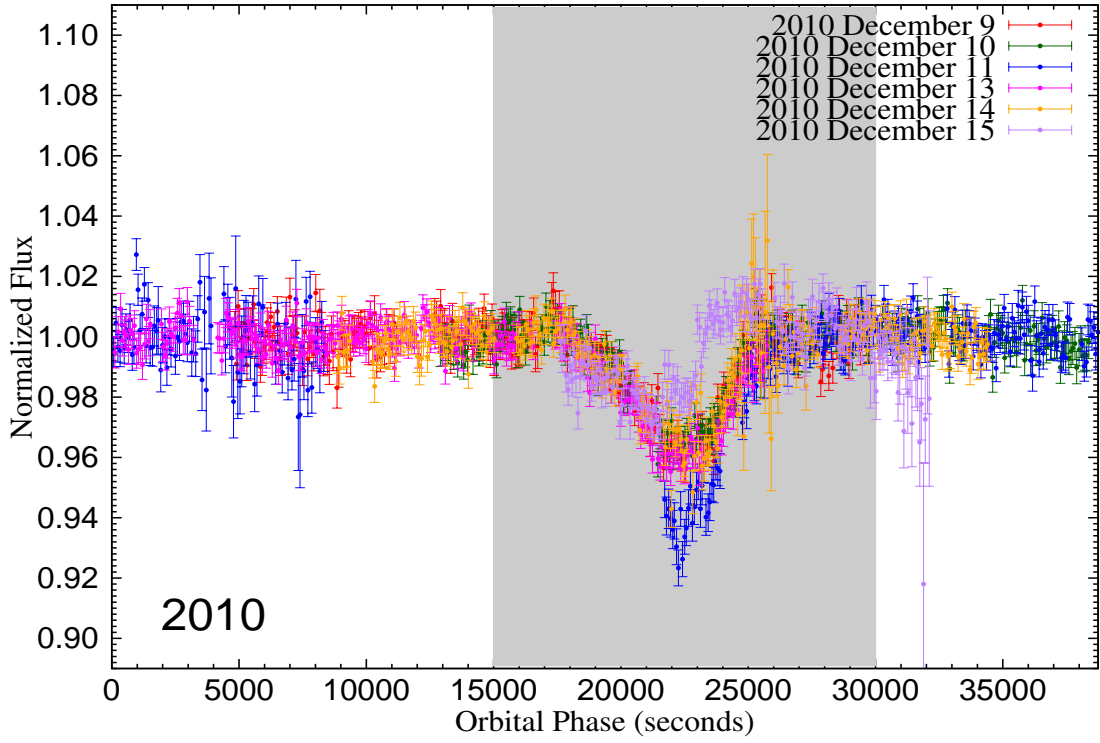


Figure 5.2: Same as Figure 5.1, but for 6 reliable light curves in 2010 observation.

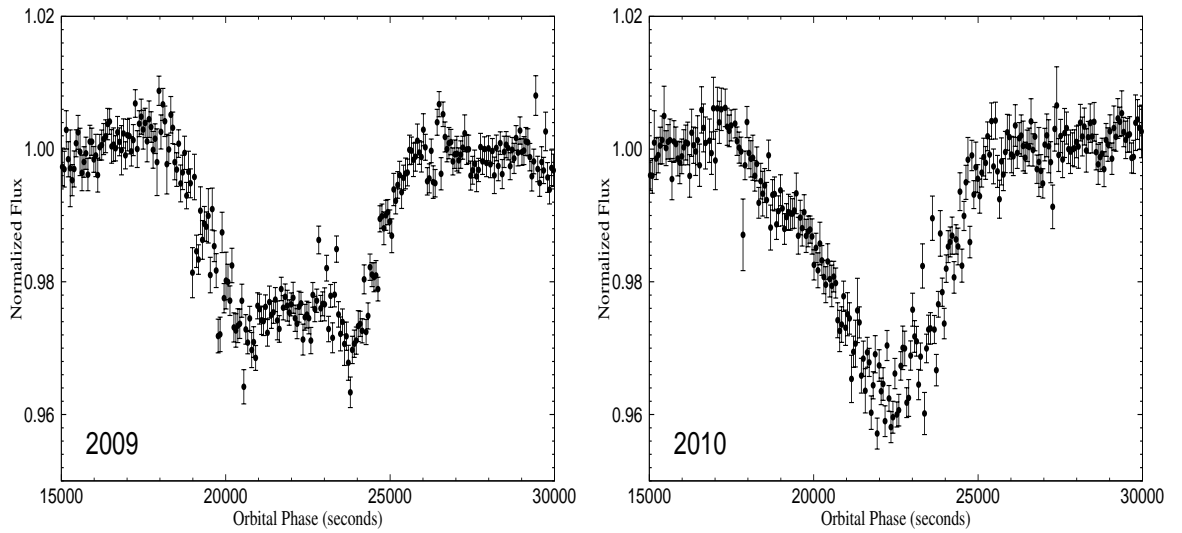


Figure 5.3: The template light curves after one-minute binning for 2009 (left) and 2010 (right) observations.

so that they minimize the  $\chi^2$  value defined as

$$\chi^2 = \sum_i \frac{(f_{\text{data},i} - f_{\text{model},i})^2}{\sigma_{\text{data},i}^2}, \quad (5.1)$$

where  $i$  indicates the variables at  $t_i$ .  $f_{\text{data},i}$  and  $\sigma_{\text{data},i}$  are the stellar flux and error of the template light curves, and  $f_{\text{model},i}$  denotes the stellar model flux calculated by the methods in chapter 4.

## 5.2 Individual fittings

We first perform the individual fits for 2009 and 2010 light curves, respectively, for the purpose of checking whether our light curve modelling scheme in chapter 4 operates correctly. The fixed values or explored ranges (basically following B13) are summarized in Table 5.1.

Table 5.1: Parameters in the individual fittings

| parameter                          | fixed value | explored range          |
|------------------------------------|-------------|-------------------------|
| $R_{\star,\text{eq}}(R_{\odot})$   | -           | 0.8 - 1.6               |
| $R_{\text{p}}/R_{\star,\text{eq}}$ | -           | 0.01 - 0.50             |
| $P_{\text{rot}}$ (days)            | 0.448410    | -                       |
| $P_{\text{orb}}$ (days)            | 0.448410    | -                       |
|                                    |             | 30861700±4320 (2009)    |
| $t_0$ (s)                          | -           | or 60848300±4320 (2010) |
| $i_{\text{orb}}(^{\circ})$         | -           | 0 - 90                  |
| $\Omega(^{\circ})$                 | -           | 0 - 360                 |
| $i_{\star}(^{\circ})$              | -           | 90 - 180                |
| $e \cos \omega$                    | 0           | -                       |
| $e \sin \omega$                    | 0           | -                       |
| $T_{\text{pol}}(K)$                | 3470        | -                       |
| $c_1$                              | 0.735       | -                       |
| $c_2$                              | 0.0         | -                       |
| $\beta_{\text{GD}}$                | 0.25        | -                       |

In Table 5.1,  $R_{\star,\text{eq}}$  is the stellar *equatorial* radius,  $R_{\text{p}}$  is the planetary radius,  $P_{\text{rot}}$  is the stellar spin period (we adopt the synchronous condition,  $P_{\text{rot}} = P_{\text{orb}}$  in this section),  $t_0$  is the time of inferior conjunction ( $\omega + f = \pi/2$ ) centered on the values in individual fits in B13 with error of 0.05 days,  $i_{\star}$  is the stellar inclination,  $i_{\text{orb}}$  is the planetary orbital inclination,  $\Omega$  is the longitude of the ascending node,  $e$  is the orbital eccentricity,  $\omega$  is the argument of the periapse in the planetary orbit,  $T_{\text{pol}}$  is the stellar polar surface temperature,  $c_1$  and  $c_2$  are limb-darkening parameters and  $\beta_{\text{GD}}$  is gravity darkening parameter.

We adopt the same fixed values for  $P_{\text{rot}}$ ,  $P_{\text{orb}}$ ,  $c_1$  and  $\beta_{\text{GD}}$  as in B13. Moreover, the explored range for  $R_{\star,\text{eq}}$  is also identical to that in B13. The value of 3470 K is used as the stellar effective temperature in B13. Since it is convenient to adopt the polar temperature rather than effective temperature for our light curve model in chapter 4, we adopt the value of 3470 K as stellar polar temperature, based on the fact that the deviation of the

polar one from effective one would be negligible. Since the value for  $c_2$  is not stated in B13, we employ the theoretical value of 0 by the estimation with the help of Claret et al. (1995) and Sing (2010).

Our results and comparison with B13 are described in Table 5.2. Table 5.2 indicates

Table 5.2: Individual fitting for 2009 (left) and 2010 (right) transits. The  $\chi_r^2$  value of B13 is just for reference.

|                | 2009         |              | 2010           |              |              |
|----------------|--------------|--------------|----------------|--------------|--------------|
|                | B13          | this work    | B13            | this work    |              |
| $R_*(R_\odot)$ | 1.19±0.07    | 1.19±0.03    | $R_*(R_\odot)$ | 1.39±0.11    | 1.34±0.08    |
| $R_p(R_J)$     | 2.00±0.17    | 1.89±0.06    | $R_p(R_J)$     | 1.80±0.20    | 2.26±0.99    |
| $t_0$ (s)      | 30861700±200 | 30861249±242 | $t_0$ (s)      | 60848300±290 | 60848126±575 |
| $i$ (°)        | 64±3         | 64.0±1.8     | $i$ (°)        | 58±5         | 54.3±5.2     |
| $\lambda$ (°)  | 90±22        | 92.0±24.3    | $\lambda$ (°)  | 136±33       | 134±36.1     |
| $\psi$ (°)     | 2±19         | -2.4±19.8    | $\psi$ (°)     | 31±25        | 17.9±32.7    |
| d.o.f          | -            | 244          | d.o.f          | -            | 239          |
| $\chi_r^2$     | (2.11)       | 2.18         | $\chi_r^2$     | (1.54)       | 1.70         |

that results in this work and those in B13 are in good agreement. Although  $t_0$  for 2009 is the only exception, its extent of deviation is not so large. Since our way of evaluating  $\chi_r^2$  value is not necessary the same as that in B13, we cannot make simple comparison of  $\chi_r^2$  between them and us. We show the  $\chi_r^2$  value of B13 not for comparison but just for reference, and the same applies to the following (Tables 5.2 and 5.4). These achievements lead to the conclusion that our light curve modelling and fitting scheme does operate correctly.

### 5.3 Extrapolation of the individual fittings

Before the joint fits, B13 extrapolated 2009/2010 individual fits through the nodal precession model, and found that the simple forward/backward predictions with  $M_* = 0.44M_\odot$  and  $M_p = 1.0M_J$  do not reproduce the transit light curve in 2010/2009. Our 2009/2010 extrapolations following B13 also fail to reproduce the observed light curves in 2010/2009 in a similar fashion to the results by B13. Therefore, we need to fit both 2009 and 2010 light curves simultaneously in joint fits. Since the shapes of extrapolated light curves are almost identical with those in B13, it is concluded that our formulae for the nodal precession in chapter 3 operates properly.

### 5.4 Joint fittings with the synchronous condition

The joint fitting always accompanies the calculation of the nodal precession from 2009 to 2010. So we need to add  $M_*$  and  $M_p$  in the parameters to specify the magnitudes of

stellar spin and planetary orbital angular momenta. The fixed values or explored ranges of the system parameters in joint fits are summarized in Table 5.1.

Table 5.1: Parameters in the joint fittings

| parameter                              | fixed value   | explored range  |
|--|---|---|
| $M_\star(M_\odot)$                     | 0.34 or 0.44  | -   |
| $M_p(M_J)$                             | -   | 0.01 - 100  |
| $R_{\star,\text{eq}}(R_\odot)$         | -   | 0.8 - 1.6   |
| $R_p/R_{\star,\text{eq}}$              | -   | 0.01 - 0.50   |
| $P_{\text{rot}}=P_{\text{orb}}$ (days) | 0.448410 (for $M_\star = 0.34M_\odot$ )<br>or 0.448413 (for $M_\star = 0.44M_\odot$ ) | -   |
| $t_0$ (s)                              | -   | $60848500 \pm 4320$<br>$125.7 \pm 10.4$ (prograde)<br>or $54.3 \pm 10.4$ (retrograde) |
| $i$ ( $^\circ$ )                       | -   | $46 \pm 72.2$ (prograde)<br>or $134 \pm 72.2$ (retrograde)                            |
| $\lambda$ ( $^\circ$ )                 | -   | $17.9 \pm 65.4$   |
| $\psi$ ( $^\circ$ )                    | -   | -   |
| $e \cos \omega$                        | 0   | -   |
| $e \sin \omega$                        | 0   | -   |
| $T_{\text{pol}}(K)$                    | 3470  | -   |
| $c_1$                                  | 0.735   | -   |
| $c_2$                                  | 0.0   | -   |
| $\beta_{\text{GD}}$                    | 0.25  | -   |

The parameter range for  $M_p$  is the same as that in joint fits in B13. We fix the stellar mass  $M_\star$  to 0.34/0.44  $M_\odot$  depending on the stellar model in Siess et al. (2000) or Baraffe et al. (1998), and vary only  $R_\star$  as in B13. Thus the parallel analyses for both cases are required as will be shown in the following subsections.

As noted in chapter 2, both prograde and retrograde solutions on  $\phi$  are possible by only individual fittings. Since the joint fits include the nodal precession and the precession period depends on  $\phi$  ( $P_\Omega \propto 1/\sin 2\phi$ ), we perform both prograde and retrograde joint fits to see which solution can reproduce 2009 and 2010 light curves better. Since both prograde and retrograde solutions of 2009 in individual fits by B13 are close to  $90^\circ$  ( $89^\circ.1$  and  $90^\circ.9$ ), the corresponding precession is too slow to provide the significant change to light curves between 2009 and 2010. Therefore B13 performed the joint fits within the bounds of 2010 individual fits, and we follow it. Since the angular results by joint fits in B13 are not within the  $1\sigma$  errors of the 2010 individual fits but within the  $2\sigma$  errors ( $i = 114^\circ.8 \pm 1^\circ.6$  by joint fits while  $i = 122^\circ \pm 5^\circ$  by 2010 individual fits), we adopt the  $2\sigma$  errors in 2010 individual fits as the angular ranges for the joint fits.

### 5.4.1 $M_\star = 0.34M_\odot$ case

Table 5.2 compares the results of B13 and ours for  $M_\star = 0.34M_\odot$ , and indicates that results by B13 and ours are in good agreement. Since it is checked that the joint fit starting

Table 5.2: Best-fit parameters in the joint fitting for  $M_\star = 0.34M_\odot$ . The  $\chi_r^2$  value of B13 is just for reference.

| parameter                 | B13               | this work        |
|---------------------------|-------------------|------------------|
| $M_p(M_J)$                | $3.0\pm 0.2$      | $2.61\pm 0.41$   |
| $R_\star(R_\odot)$        | $1.04\pm 0.01$    | $1.14\pm 0.02$   |
| $R_p(R_J)$                | $1.64\pm 0.07$    | $1.87\pm 0.04$   |
| $t_0$ (s)                 | $60848500\pm 100$ | $60847907\pm 19$ |
| $i$ ( $^\circ$ )          | $114.8\pm 1.6$    | $121.5\pm 0.9$   |
| $\lambda$ ( $^\circ$ )    | $43.9\pm 5.2$     | $51.7\pm 2.8$    |
| $\psi$ ( $^\circ$ )       | $29.4\pm 0.3$     | $25.4\pm 2.4$    |
| $\phi$ ( $^\circ$ )       | 69                | 75.3             |
| $\phi_\star$ ( $^\circ$ ) | 18                | 14.4             |
| $\phi_p$ ( $^\circ$ )     | 51                | 61.0             |
| $P_\Omega$ (days)         | 292.6             | 287.5            |
| $f$                       | 0.109             | 0.145            |
| d.o.f                     | -                 | 490              |
| $\chi_r^2$                | (2.17)            | 1.99             |

Table 5.3: Stellar radius with different definitions for  $M_\star = 0.34M_\odot$

|                    | B13            | this work      | this work $\times \sqrt{1-f}$ | this work $\times \sqrt[3]{1-f}$ |
|--------------------|----------------|----------------|-------------------------------|----------------------------------|
| $R_\star(R_\odot)$ | $1.04\pm 0.01$ | $1.14\pm 0.02$ | $1.05\pm 0.02$                | $1.08\pm 0.02$                   |
| $R_p(R_J)$         | $1.64\pm 0.07$ | $1.87\pm 0.04$ | $1.73\pm 0.04$                | $1.77\pm 0.04$                   |

with the solution by B13 (middle column in Table 5.2) returns the solution identical to our results (right column in Table 5.2), we conclude that we found the solution corresponding to that in B13. Within these parameters,  $M_p$ ,  $R_\star$  and  $R_p$  are worth being individually examined because they are most basic physical parameters for the star and planet. The planetary mass in this work agrees with that in B13 within  $1\sigma$  precision, while this is not the case for stellar and planetary radii.

This discrepancy could be attributed to the difference in the definitions of the stellar radius ( $R_\star$ ). Stellar radius in this work refers to the stellar *equatorial* radius, while there is no statement for the rigid definition of  $R_\star$  in B13. Therefore it is possible that they use the symbol  $R_\star$  to denote the stellar *effective* radius, which is different from stellar equatorial radius by the order of  $f$ . This difference cannot be neglected in our current viewpoint since we drop  $\mathcal{O}(f^2)$  and higher order terms but does not  $\mathcal{O}(f)$ . There exists

several ways to define the stellar effective radius. One of them is to define it so that the surface area of the stellar disk in the sky plane is identical to that of the circle with stellar effective radius as

$$R_{\star,\text{eff}} \equiv \sqrt{R_{\star,\text{eq}}R_{\star,\text{pol}}} = R_{\star,\text{eq}}\sqrt{1-f}, \quad (5.2)$$

where  $R_{\star,\text{pol}} = (1-f)R_{\star,\text{eq}}$  is the stellar polar radius. Another way is to define it so that the volume of the star is conserved as

$$R_{\star,\text{eff}} \equiv \sqrt[3]{R_{\star,\text{eq}}^2R_{\star,\text{pol}}} = R_{\star,\text{eq}}\sqrt[3]{1-f}. \quad (5.3)$$

Table 5.3 compares the stellar radius in B13 and stellar radii in this work with several definitions ( $R_{\star,\text{eq}}$  itself,  $R_{\star,\text{eq}}$  factored by  $\sqrt{1-f}$  and  $R_{\star,\text{eq}}$  factored by  $\sqrt[3]{1-f}$ ). Then it is concluded that the stellar radius in B13 and ours agree when B13 defined the symbol  $R_{\star}$  to denote the stellar effective radius (equation 5.2).

The planetary radius is evaluated through the transit depth which is dependent on the ratio of planetary to stellar radius ( $R_{\text{p}}/R_{\star}$ ). Therefore the difference in the definition of stellar radius propagates into the evaluation of planetary radius. Table 5.3 demonstrates also the planetary radii with different definitions for the stellar radius. And it is seen that planetary radius in B13 agrees with ours when  $R_{\star}$  in B13 is intended to denote the stellar effective radius (equation 5.2).

This propagation of discrepancy from stellar to planetary radius can be checked by taking the ratio of  $R_{\text{p}}/R_{\star}$  in this work to that in B13 as

$$\frac{R_{\text{p}}/R_{\star}(\text{this work})}{R_{\text{p}}/R_{\star}(\text{B13})} = \frac{1.87/1.14}{1.64/1.04} \sim 1.04, \quad (5.4)$$

which is found to be close to unity.

Although angular parameters ( $i$ ,  $\lambda$ ,  $\psi$ ,  $\phi$ ,  $\phi_{\star}$  and  $\phi_{\text{p}}$ ) by B13 and this work do not agree with each other within  $1\sigma$  precision, their discrepancies are found to be within several degrees ( $^{\circ}$ ). These considerations on individual parameters also support the conclusion that our solution correspond to that in B13.

#### 5.4.2 $M_{\star} = 0.44M_{\odot}$ case

Table 5.4 compares the results of B13 and ours for  $M_{\star} = 0.44M_{\odot}$ . First of all, it should be noted that the joint fit starting with the solution by B13 (middle column in Table 5.4) is not converged into our solution (right column in Table 5.2) but provides the solution worse than ours in terms of  $\chi_r^2$  value. Thereby we conclude that we succeeded in discovering the better solution than that in B13.

The discussion on individual parameters is as follows. The planetary mass in this work agrees with that in B13 with  $1\sigma$  precision as does in the case of  $M_{\star} = 0.34M_{\odot}$ . However, the stellar and planetary radii are not in agreement even under the modification by either  $\times\sqrt{1-f}$  or  $\times\sqrt[3]{1-f}$  as shown in Table 5.5. This discrepancy is in favor of the

Table 5.4: Best-fit parameters in the joint fitting for  $M_\star = 0.44M_\odot$ . The  $\chi_r^2$  value of B13 is just for reference.

| parameter                 | B13              | this work        |
|---------------------------|------------------|------------------|
| $M_p(M_J)$                | $3.6\pm 0.3$     | $4.20\pm 0.53$   |
| $R_\star(R_\odot)$        | $1.03\pm 0.01$   | $1.24\pm 0.02$   |
| $R_p(R_J)$                | $1.68\pm 0.07$   | $2.04\pm 0.04$   |
| $t_0$ (s)                 | $60848363\pm 38$ | $60848041\pm 18$ |
| $i$ ( $^\circ$ )          | $110.7\pm 1.3$   | $121.9\pm 0.8$   |
| $\lambda$ ( $^\circ$ )    | $54.5\pm 0.5$    | $44.3\pm 3.9$    |
| $\psi$ ( $^\circ$ )       | $30.3\pm 1.3$    | $30.8\pm 2.6$    |
| $\phi$ ( $^\circ$ )       | 73.1             | 75.4             |
| $\phi_\star$ ( $^\circ$ ) | 20.2             | 17.5             |
| $\phi_p$ ( $^\circ$ )     | 52.9             | 58.0             |
| $P_{\dot{\Omega}}$ (days) | 581.2            | 283.7            |
| $f$                       | 0.083            | 0.144            |
| d.o.f                     | -                | 488              |
| $\chi_r^2$                | (2.19)           | 2.15             |

Table 5.5: Stellar radius with different definitions for  $M_\star = 0.44M_\odot$

|                    | B13            | this work      | this work $\times \sqrt{1-f}$ | this work $\times \sqrt[3]{1-f}$ |
|--------------------|----------------|----------------|-------------------------------|----------------------------------|
| $R_\star(R_\odot)$ | $1.03\pm 0.01$ | $1.24\pm 0.02$ | $1.15\pm 0.02$                | $1.18\pm 0.02$                   |
| $R_p(R_J)$         | $1.68\pm 0.07$ | $2.04\pm 0.04$ | $1.89\pm 0.04$                | $1.94\pm 0.04$                   |

conclusion that solution by B13 and ours are essentially different. Since the planet-star radius ratios are almost identical with each other

$$\frac{R_p/R_\star(\text{this work})}{R_p/R_\star(\text{B13})} = \frac{2.04/1.24}{1.68/1.03} \sim 1.01, \quad (5.5)$$

specifically, this result indicates that our analysis estimated the significantly larger value for stellar radius than that in B13. This overestimation sensitively affects the precession period. It is remarkable that our result corresponds to the similar precession period to results in Table 5.2 ( $\sim 300$  days), while result in B13 shows about twice slower precession ( $\sim 600$  days). We here recall the dependence of the precession period on physical parameters as

$$P_{\dot{\Omega}} \propto M_\star^{5/3} R_\star^{-5} \omega_\star^{-2} n^{-7/3} \sin \phi_p (\sin 2\phi)^{-1}. \quad (3.17)$$

The larger stellar mass of  $0.44M_\odot$  compared to  $0.34M_\odot$  with other parameters ( $R_\star$ ,  $\omega_\star$ ,  $n$ ,  $\phi_p$  and  $\phi$ ) almost identical between these cases provided almost doubled precession period (581.2 days compared to 292.6 days) in B13. In this work, however, the effect of larger

stellar mass  $((0.44/0.34)^{5/3})$  is considerably suppressed by the effect of larger estimation for the stellar radius  $((1.24/1.14)^{-5})$ , which leads to the comparable precession period of 283.7 days ( $M_\star = 0.44M_\odot$ ) to 287.5 days ( $M_\star = 0.34M_\odot$ ). This is the example case of the degeneracy of precession period noted in chapter 2. Namely, the precessions with frequency of  $\frac{1}{2}\dot{\Omega}$ ,  $\dot{\Omega}$ ,  $2\dot{\Omega}$ , ... are possible as the solutions.

## 5.5 Data analysis without the synchronous condition

Next we move on to the parameter fit adopting the stellar spin period as an additional fitting parameter. We abandon all solutions that exceed the stellar break-up condition beyond which the star cannot retain the gravitationally-bounded shape:

$$R_{\star,\text{eq}}\omega_\star^2 - \frac{GM_\star}{R_{\star,\text{eq}}^2} > 0$$

$$\Leftrightarrow P_{\text{rot}} > 2\pi\sqrt{\frac{3}{4\pi G\rho_\star}}. \quad (5.6)$$

### 5.5.1 Individual fittings

In B13, they utilized the results on the angular parameters in individual fits with  $P_{\text{rot}} = 0.448410$  days in order to set the angular ranges of the subsequent joint fits. However, it is unclear that this angular ranges in individual fits with  $P_{\text{rot}} = 0.448410$  days are also applicable to the joint fits without the synchronous condition where the stellar spin period can deviate from  $P_{\text{rot}} = 0.448410$  days. Before the joint fits without the synchronous condition, therefore, it is necessary to investigate the dependence of angular ranges in the individual fits on the stellar spin period. If the angular ranges are not affected by the stellar spin period so much, then we could utilize the same angular ranges in the joint fits without the synchronous condition as those in the individual fits with synchronous condition with  $P_{\text{rot}} = 0.448410$  days. Based on this motivation, we first perform the 2010 individual fits with fixed stellar spin period of  $P_{\text{rot}} = 0.3, 0.4, 0.5, \dots, 1.9, 2.0$  days and investigated how the angular ranges depend on the stellar spin period. The results are summarized in Table 5.1. Table 5.1 implies

1. All  $i$  values are consistent within  $1\sigma$  error in the case of  $P_{\text{rot}} = 0.448410$  days ( $5^\circ.2$ ).
2. All  $\lambda$  values but that for  $P_{\text{rot}} = 0.3$  days are consistent within  $1\sigma$  error in the case of  $P_{\text{rot}} = 0.448410$  days ( $36^\circ.4$ ).
3. All  $\psi$  values are consistent within  $1\sigma$  error in the case of  $P_{\text{rot}} = 0.448410$  days ( $32^\circ.7$ ).
4.  $\chi_r^2$  value becomes worse as the star rotates more slowly.

Again the angular results by joint fits in B13 are beyond the  $1\sigma$  error of the 2010 individual fits but within the  $2\sigma$ . Based on this fact, we set the angular ranges for the joint fits

Table 5.1: Angular parameters and  $\chi_r^2$  value for the 2010 individual fittings for differently-fixed stellar spin periods. Since the covariance matrix from the Levenberg-Marquardt fitting algorithm is used to generate the quoted errors, errors in angular parameters could exceed  $180^\circ$ .

| stellar spin period (days)                | $i(^\circ)$     | $\lambda(^\circ)$  | $\psi(^\circ)$    | $\chi_r^2$ |
|---|-----------------|--------------------|-------------------|------------|
| 0.3                                       | $54.2 \pm 13.4$ | $81.6 \pm 28.3$    | $41.4 \pm 12.9$   | 1.67       |
| 0.4                                       | $52.5 \pm 11.2$ | $113.4 \pm 16.1$   | $31.7 \pm 20.1$   | 1.68       |
| 0.448410<br>(same as that in section 5.2) | $54.3 \pm 5.2$  | $133.9 \pm 36.4$   | $17.9 \pm 32.7$   | 1.71       |
| 0.5                                       | $56.2 \pm 15.8$ | $133.0 \pm 161.9$  | $21.4 \pm 126.3$  | 1.84       |
| 0.6                                       | $56.3 \pm 29.5$ | $133.5 \pm 374.9$  | $24.9 \pm 317.6$  | 1.97       |
| 0.7                                       | $55.7 \pm 42.2$ | $134.1 \pm 615.4$  | $26.6 \pm 547.2$  | 2.03       |
| 0.8                                       | $55.3 \pm 58.0$ | $134.3 \pm 864.5$  | $27.4 \pm 803.2$  | 2.06       |
| 0.9                                       | $54.8 \pm 70.6$ | $134.6 \pm 1012.6$ | $27.9 \pm 981.1$  | 2.08       |
| 1.0                                       | $54.9 \pm 51.3$ | $134.7 \pm 575.9$  | $28.3 \pm 885.3$  | 2.09       |
| 1.1                                       | $55.0 \pm 42.8$ | $134.8 \pm 460.9$  | $28.7 \pm 830.6$  | 2.11       |
| 1.2                                       | $55.1 \pm 36.8$ | $135.0 \pm 244.9$  | $28.9 \pm 735.1$  | 2.12       |
| 1.3                                       | $55.2 \pm 32.6$ | $135.0 \pm 193.3$  | $29.1 \pm 776.4$  | 2.12       |
| 1.4                                       | $55.2 \pm 31.2$ | $135.0 \pm 197.3$  | $29.3 \pm 858.2$  | 2.13       |
| 1.5                                       | $55.3 \pm 28.3$ | $135.2 \pm 226.3$  | $29.4 \pm 883.5$  | 2.13       |
| 1.6                                       | $55.3 \pm 26.9$ | $135.2 \pm 244.1$  | $29.5 \pm 969.0$  | 2.14       |
| 1.7                                       | $55.3 \pm 26.2$ | $135.2 \pm 245.9$  | $29.6 \pm 3567.3$ | 2.14       |
| 1.8                                       | $55.4 \pm 25.1$ | $135.0 \pm 3397.2$ | $29.6 \pm 4897.9$ | 2.14       |
| 1.9                                       | $55.4 \pm 24.4$ | $135.2 \pm 340.4$  | $29.7 \pm 1279.9$ | 2.14       |
| 2.0                                       | $55.4 \pm 23.8$ | $135.1 \pm 182.7$  | $29.8 \pm 1339.0$ | 2.14       |

without the synchronous condition basically as the  $2\sigma$  errors of the 2010 individual fits for  $P_{\text{rot}} = 0.448410$  days. The only one exception is the range for  $\lambda$ . The result of  $\lambda$  for  $P_{\text{rot}} = 0.3$  days ( $81^\circ.6 \pm 28^\circ.3$ ) goes beyond even  $2\sigma$  errors of our 2010 individual fits for  $P_{\text{rot}} = 0.448410$  days ( $133^\circ.9 \pm 72^\circ.8$ ). Taken together, we adopt the survey ranges for angular parameters as follows.

1. The survey range of  $i$  is within  $2\sigma$  error in the case of  $P_{\text{rot}} = 0.448410$  days, as  $i(^\circ) = 126.7 \pm 10.4$  for prograde solution,  $i(^\circ) = 54.3 \pm 10.4$  for retrograde solution.
2. The survey range of  $\lambda$  is enlarged so that the range in the case of  $P_{\text{rot}} = 0.448410$  days covers the range in the case of  $P_{\text{rot}} = 0.3$  days, as  $\lambda(^\circ) = 46.1 \pm 80.6$  for prograde solution,  $\lambda(^\circ) = 133.9 \pm 80.6$  for retrograde solution.
3. The survey range of  $\psi$  is within  $2\sigma$  error in the case of  $P_{\text{rot}} = 0.448410$  days, as  $\psi(^\circ) = 17.9 \pm 55.4$ .

Ranges to be surveyed for other parameters are the same as those in Table 5.1.

In addition, we set the upper and lower limits on the stellar spin period  $P_{\text{rot}}$  as follows.

1. Upper limit is 30 days resembling the rotational period of the Sun.
2. Lower limit is set so that  $P_{\text{rot}}$  is within the boundary beyond which the the star breaks up even with the lower limit radius ( $0.8R_{\odot}$ ), as  $P_{\text{rot}} > 2\pi\sqrt{\frac{(0.8R_{\odot})^3}{GM_{\star}}}$ .

### 5.5.2 Joint fittings for $M_{\star} = 0.34M_{\odot}$ case

We repeated the joint fits starting with a variety of the initial values for angular parameters ( $i_{\text{orb}}$ ,  $\Omega$ ,  $i_{\star}$ ) and stellar spin period ( $P_{\text{rot}}$ ). Table 5.2 presents the best, second-best and third-best prograde solutions and best prograde solution with synchronous condition for comparison. We were not able to find the self-consistent retrograde solutions. Table 5.2

Table 5.2: Best solutions in the joint fittings without the synchronous condition for  $M_{\star} = 0.34M_{\odot}$

| parameter                                     | synchronous case | best             | second-best      | third-best       |
|---|------------------|------------------|------------------|------------------|
| $M_{\text{p}}(M_{\text{J}})$                  | $2.61\pm 0.41$   | $6.24\pm 0.29$   | $7.20\pm 0.32$   | $6.74\pm 0.13$   |
| $R_{\star,\text{eq}}(R_{\odot})$              | $1.14\pm 0.02$   | $1.22\pm 0.01$   | $1.21\pm 0.01$   | $1.18\pm 0.01$   |
| $R_{\star,\text{eq}}\sqrt{1-f}(R_{\odot})$    | $1.05\pm 0.02$   | $1.06\pm 0.01$   | $1.05\pm 0.01$   | $1.05\pm 0.01$   |
| $R_{\star,\text{eq}}\sqrt[3]{1-f}(R_{\odot})$ | $1.08\pm 0.02$   | $1.11\pm 0.01$   | $1.10\pm 0.01$   | $1.10\pm 0.01$   |
| $R_{\text{p}}(R_{\text{J}})$                  | $1.87\pm 0.04$   | $2.34\pm 0.07$   | $2.53\pm 0.12$   | $2.08\pm 0.05$   |
| $R_{\text{p}}\sqrt{1-f}(R_{\text{J}})$        | $1.73\pm 0.04$   | $2.05\pm 0.07$   | $2.19\pm 0.10$   | $1.86\pm 0.04$   |
| $R_{\text{p}}\sqrt[3]{1-f}(R_{\text{J}})$     | $1.77\pm 0.04$   | $2.14\pm 0.07$   | $2.30\pm 0.11$   | $1.93\pm 0.04$   |
| $P_{\text{rot}}$ (days)                       | 0.448410         | $0.389\pm 0.006$ | $0.375\pm 0.006$ | $0.397\pm 0.006$ |
| $t_0$ (s)                                     | $60847907\pm 19$ | $60847981\pm 19$ | $60847950\pm 20$ | $60847966\pm 18$ |
| $i(^{\circ})$                                 | $121.5\pm 0.9$   | $126.4\pm 0.7$   | $127.2\pm 0.8$   | $124.0\pm 0.7$   |
| $\lambda(^{\circ})$                           | $51.7\pm 2.8$    | $52.7\pm 2.0$    | $54.0\pm 2.0$    | $50.3\pm 1.0$    |
| $\psi(^{\circ})$                              | $25.4\pm 2.4$    | $37.3\pm 1.7$    | $41.1\pm 1.8$    | $41.2\pm 0.0$    |
| $\phi(^{\circ})$                              | 75.3             | 88.4             | 92.5             | 88.2             |
| $\phi_{\star} (^{\circ})$                     | 14.4             | 26.9             | 30.4             | 30.4             |
| $\phi_{\text{p}} (^{\circ})$                  | 61.0             | 61.5             | 62.1             | 57.8             |
| $P_{\dot{\Omega}}$ (days)                     | 287.5            | 1398.7           | 819.3            | 1425.2           |
| $f$   | 0.145            | 0.234            | 0.251            | 0.207            |
| d.o.f   | 489              | 489              | 489              | 489              |
| $\chi_r^2$                                    | 1.989            | 1.970            | 1.973            | 1.974            |

concludes that the removal of the spin-orbit synchronous condition causes a variety of solutions to be possible for the current observational data. In other words, the model light curves constructed by these solutions are almost identical with each other as Figure 5.4 plots. Therefore we are not able to distinguish them with current data yet and it is still premature to conclude that the best solution in Table 5.2 are the unique solution and all others fail.

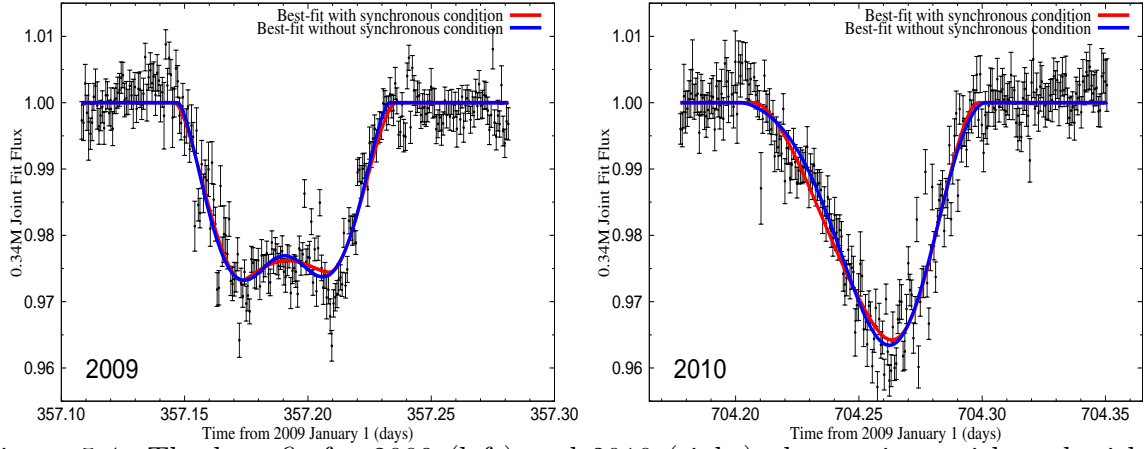


Figure 5.4: The best-fit for 2009 (left) and 2010 (right) observations with and without synchronous condition (red and blue, respectively) for  $M_{\star} = 0.34M_{\odot}$ .

### 5.5.3 Joint fittings for $M_{\star} = 0.44M_{\odot}$ case

We describe the best, second-best and third-best prograde solutions for  $M_{\star} = 0.44M_{\odot}$  and best prograde solution with the synchronous condition for comparison in Table 5.3. Again in this case we were unable to find the self-consistent retrograde solutions. The conclusion for  $M_{\star} = 0.44M_{\odot}$  is the same as that for  $M_{\star} = 0.34M_{\odot}$ . Namely, a variety of solutions are possible for the current data, and they give almost identical light curves as Figure 5.5. This degeneracy prevents us from interpreting that the best solution without synchronous condition is the unique solution in this case and other solution candidates are all of no use.

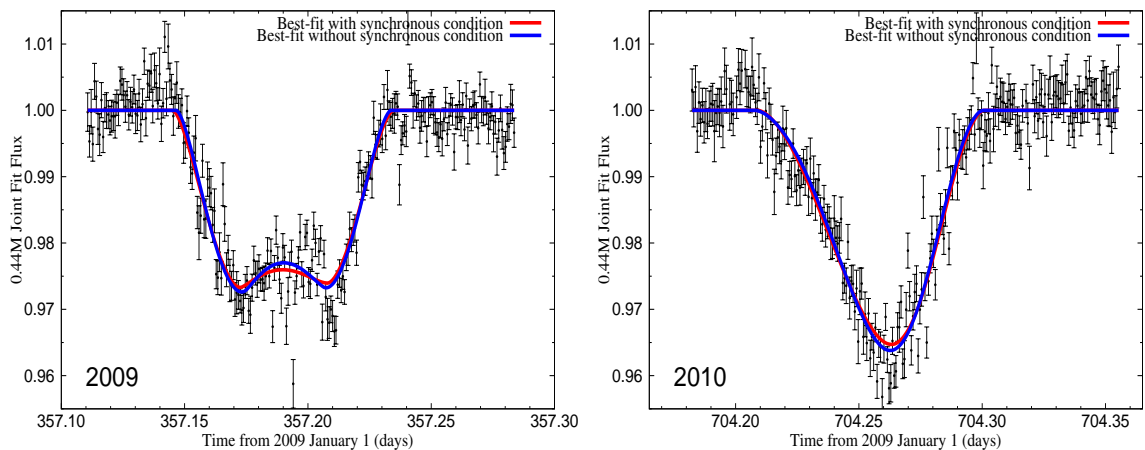


Figure 5.5: The best-fit for 2009 (left) and 2010 (right) observations with and without synchronous condition (red and blue, respectively) for  $M_{\star} = 0.44M_{\odot}$ .

Table 5.3: Best solutions in the joint fittings without the synchronous condition for  $M_\star = 0.44M_\odot$ 

| parameter                                   | synchronous case | best             | second-best      | third-best       |
|---|------------------|------------------|------------------|------------------|
| $M_p(M_J)$                                  | $4.20\pm 0.53$   | $5.82\pm 0.53$   | $8.36\pm 0.39$   | $7.76\pm 0.35$   |
| $R_{\star,\text{eq}}(R_\odot)$              | $1.24\pm 0.02$   | $1.26\pm 0.02$   | $1.32\pm 0.01$   | $1.31\pm 0.01$   |
| $R_{\star,\text{eq}}\sqrt{1-f}(R_\odot)$    | $1.15\pm 0.02$   | $1.14\pm 0.02$   | $1.13\pm 0.01$   | $1.12\pm 0.01$   |
| $R_{\star,\text{eq}}\sqrt[3]{1-f}(R_\odot)$ | $1.18\pm 0.02$   | $1.18\pm 0.02$   | $1.19\pm 0.01$   | $1.18\pm 0.01$   |
| $R_p(R_J)$                                  | $2.04\pm 0.04$   | $2.11\pm 0.05$   | $3.05\pm 0.14$   | $3.29\pm 0.18$   |
| $R_p\sqrt{1-f}(R_J)$                        | $1.89\pm 0.04$   | $1.91\pm 0.05$   | $2.62\pm 0.12$   | $2.81\pm 0.15$   |
| $R_p\sqrt[3]{1-f}(R_J)$                     | $1.94\pm 0.04$   | $1.98\pm 0.05$   | $2.75\pm 0.13$   | $2.96\pm 0.16$   |
| $P_{\text{rot}}$ (days)                     | 0.448413         | $0.412\pm 0.007$ | $0.366\pm 0.006$ | $0.356\pm 0.007$ |
| $t_0$ (s)                                   | $60848041\pm 18$ | $60848060\pm 17$ | $60848161\pm 19$ | $60848274\pm 21$ |
| $i$ ( $^\circ$ )                            | $121.9\pm 0.8$   | $122.8\pm 0.9$   | $128.9\pm 0.7$   | $129.8\pm 0.6$   |
| $\lambda$ ( $^\circ$ )                      | $44.3\pm 3.9$    | $43.9\pm 3.4$    | $45.8\pm 2.2$    | $41.7\pm 2.3$    |
| $\psi$ ( $^\circ$ )                         | $30.8\pm 2.6$    | $34.3\pm 2.2$    | $38.9\pm 1.5$    | $38.0\pm 1.4$    |
| $\phi$ ( $^\circ$ )                         | 75.4             | 78.7             | 88.5             | 86.7             |
| $\phi_\star$ ( $^\circ$ )                   | 17.5             | 21.5             | 26.3             | 24.1             |
| $\phi_p$ ( $^\circ$ )                       | 58.0             | 57.2             | 62.1             | 62.6             |
| $P_{\dot{\Omega}}$ (days)                   | 283.7            | 281.4            | 1288.5           | 593.9            |
| $f$   | 0.144            | 0.178            | 0.263            | 0.271            |
| d.o.f                                       | 489              | 489              | 489              | 489              |
| $\chi_r^2$                                  | 2.155            | 2.115            | 2.146            | 2.150            |

## 5.6 Discussion

### 5.6.1 Re-analysis of the current data without phase-fold

It is worthwhile referring to the advantage and drawback of the phase-fold. In this procedure the white noises on each light curve are significantly offset to produce the less noisy light curve. The observed data of PTFO 8-8695 is so noisy that noise-reduction by phase-fold is very useful to analyze the light curve with better precision and accuracy. The weak point of this procedure is, however, that any change of transit light curve over the observational intervals is lost by combining several light curves into one. Since 2009 observation spreads over about 1.5 months and 2010 over about 1 week, this problem is rather striking particularly in 2009 observation. Figure 5.6 shows the theoretical prediction of the transit light curves within the 2009 observational term from 2009 December 4 to 2010 January 15 for  $M_\star = 0.34M_\odot$  with the synchronous condition. The top panel illustrates the evolution of transit light curves for every two weeks (red, magenta, cyan and blue, in series), and these epochs correspond to the colored vertical lines at the bottom panel in series. It can be seen that the 1.5 months duration obviously brings about the significant change in shape of transit light curves, and thereby some information on their variabil-

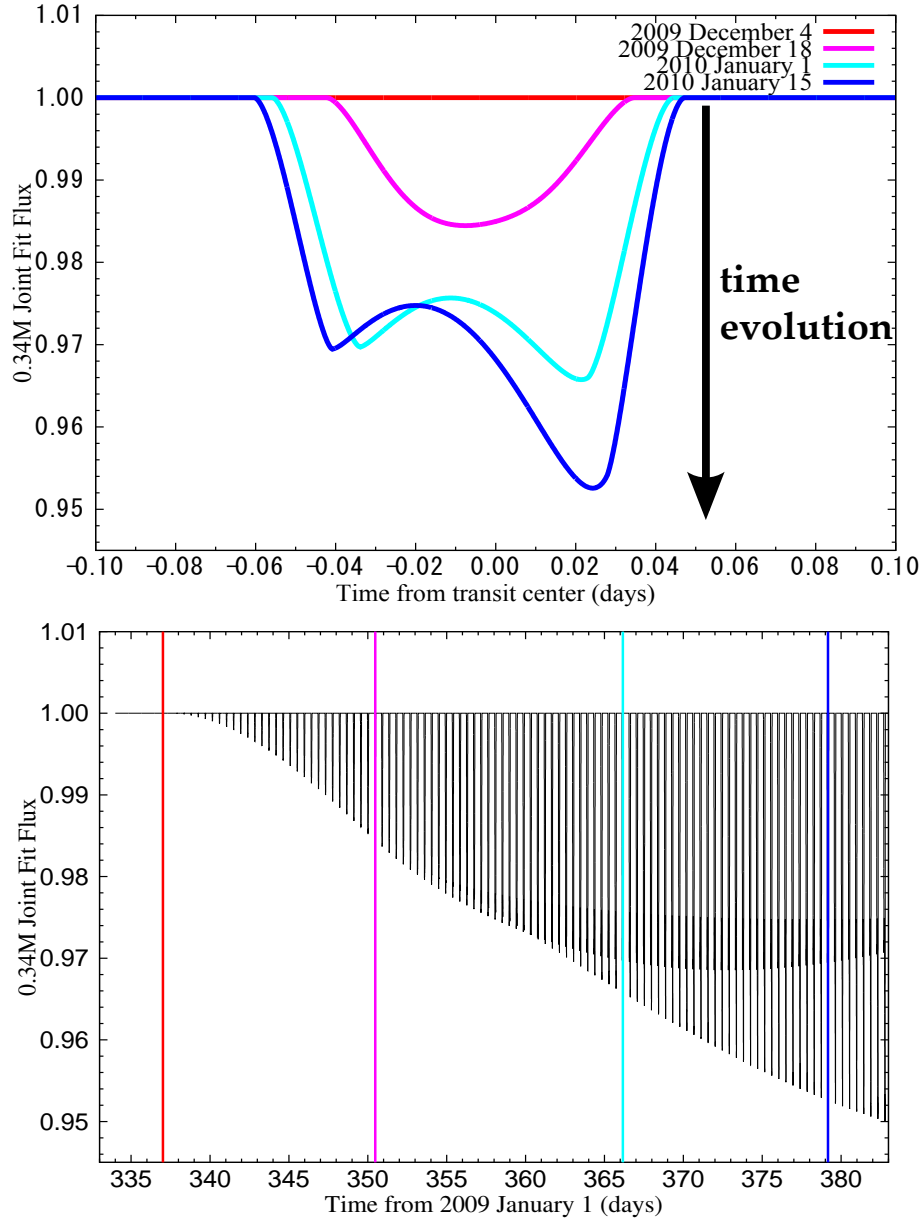


Figure 5.6: The predicted evolution of the transit light curve during the 2009 observational epoch (from 2009 December 1 to 2010 January 18) with the spin-orbit synchronous condition for  $M_{\star} = 0.34M_{\odot}$ . The top panel shows the time evolution of transit light curve for every two weeks (red, magenta, cyan and blue, in series), and these observational epochs correspond to the colored vertical lines at the bottom panel.

ity is lost by phase-fold. This theoretical prediction questions the validity of phase-fold and then raises the necessity of re-analyzing the current data without phase-fold. This re-analysis accompanies the increase of the computational cost to treat larger number of transit light curves simultaneously. However, this problem is worth being tackled with seriously for the purpose of picking up the additional information on PTF0 8-8695 system

that phase-folded data never provides.

Figure 5.7 is to assess the features of each transit light curve which phase-fold and subsequent averaging would conceal. Figure 5.7 is basically the same as Figures 5.1 and

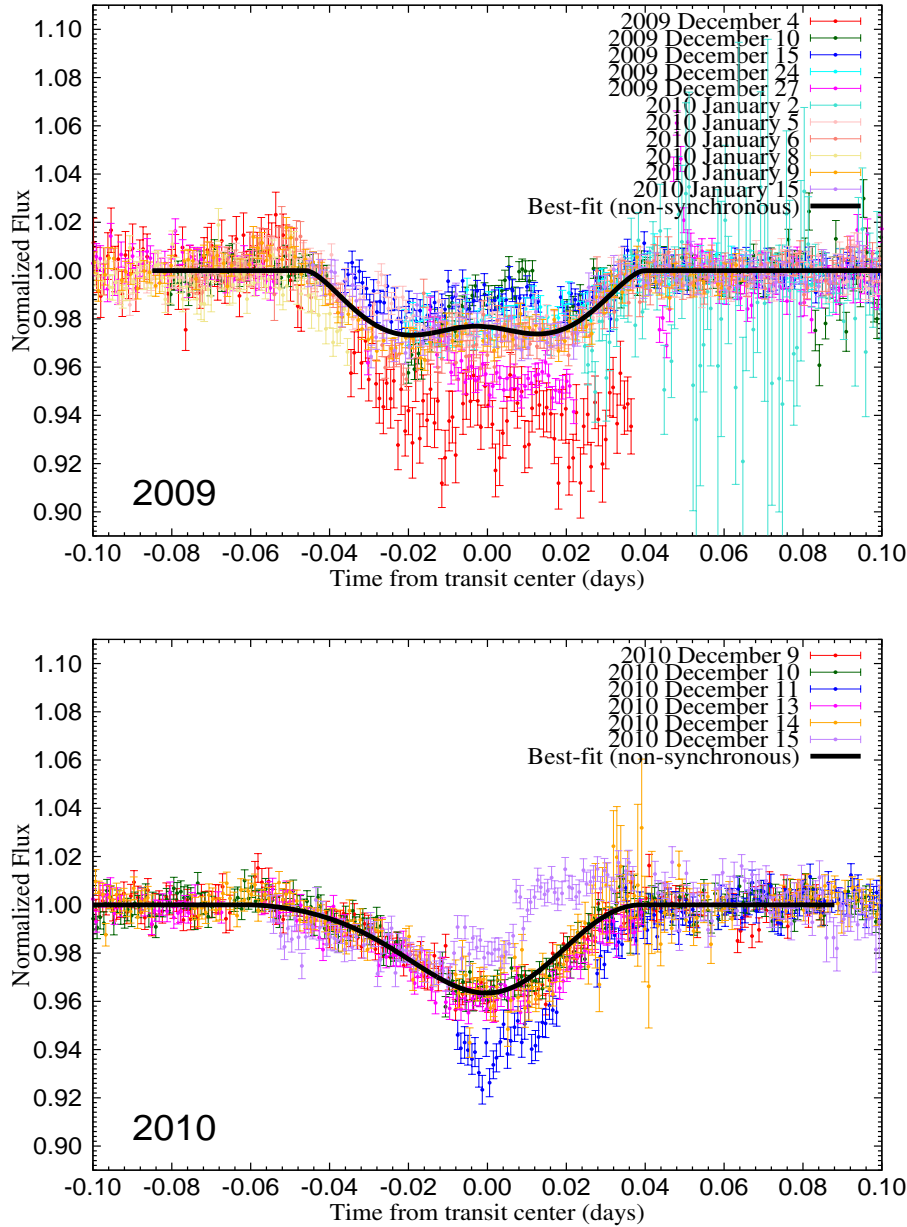


Figure 5.7: Phase-folded transit light curve for 11 reliable light curves in 2009 (top) and 2010 (bottom) observation supplemented with the best-fit model light curves (black lines). Different colors show different days when transit was observed.

5.2 but supplemented with the best-fit model light curve (black lines). It is obvious that 2009 December 9 (red at the top panel), 2009 December 27 (magenta at the top panel), 2010 December 11 (blue at the bottom panel) and 2010 December 15 (purple at the

bottom panel) transits significantly deviate from the best-fit to the averaged light curve. Apart from the discussion whether these deviation comes from the precession-induced variability of the transit light curves, it is concluded that the averaging followed by the phase-fold would miss such features of each transit light curve.

### 5.6.2 Future prediction to distinguish the possible solutions

We next discuss the difference of the variability among the possible solutions given in the previous section. The future prediction of the transit light curve shape is presented, and their detectability is argued in this section for the purpose of distinguishing the possible solutions. As shown in the previous section, removal of the spin-orbit synchronous condition provides the diversity of the architecture of the nodal precession, thus the possible solutions without the synchronous condition are mutually different. It is worth being stressed that such a difference of the precession state is the key to distinguish a variety of solutions from the future observation for PTFO 8-8695 system. First, we see how the precession architectures between them differ from 2009 to 2010 observation. Since the precession periods of the best solution with the synchronous condition, best, second-best and third-best solutions without the synchronous condition are completely different (288, 1399, 819 and 1425 days for  $M_\star = 0.34M_\odot$  and 284, 281, 1289 and 594 days for  $M_\star = 0.44M_\odot$ ), the variability of transit light curves are predicted to be correspondingly different. Figure 5.8 illustrates how differently the four solutions for  $M_\star = 0.34M_\odot$  (Table 5.2) connect the 2009 and 2010 observations, and Figure 5.9 is for  $M_\star = 0.44M_\odot$  (Table 5.3). In Figures 5.8 and 5.9, the time evolution of the transit depth by the best solution with the synchronous condition is shown as red lines, while magenta, cyan and blue lines are for the best, second-best and third-best solutions without the synchronous condition, respectively. Although each solution provides almost identical transit light curves at the epoch of 2009 and 2010 observations (top-left and bottom-right graphs, respectively, in the top panels in Figures 5.8 and 5.9), it is obvious that their shapes at the intermediate epochs are different with each other. Specifically, the bottom-left graphs at the top panels in Figures 5.8 and 5.9 illustrate one of the epochs when the difference of the transit depth among possible solutions is expected to be maximized. This is the epoch during which some of the transit signals are expected to disappear (red for  $M_\star = 0.34M_\odot$ , and red and magenta for  $M_\star = 0.44M_\odot$ ). Thereby such a (almost) transit-less epoch is particularly preferable to the observation for the immediate distinction of these possible solutions. In conclusion, taking the additional observation is the most straightforward way to see which solution is likely to hold in the actual system.

For that reason, we are now collaborating with Prof. Atsunori Yonahara and his colleagues in Kyoto Sangyo University (KSU). They are now trying to observe PTFO 8-8695 with their 1.3 m Araki-telescope in Koyama Astronomical Observatory (KAO), and under the process of detecting the actual transit signals. The transit observation will be performed intensively from 2014 November to 2015 January during which the time evolution of the transit light curves is predicted as in the light gray regions in Figures 5.10 and 5.11. Again the best solution with the synchronous condition is shown as red lines, while magenta, cyan and blue lines are for the best, second-best and third-best

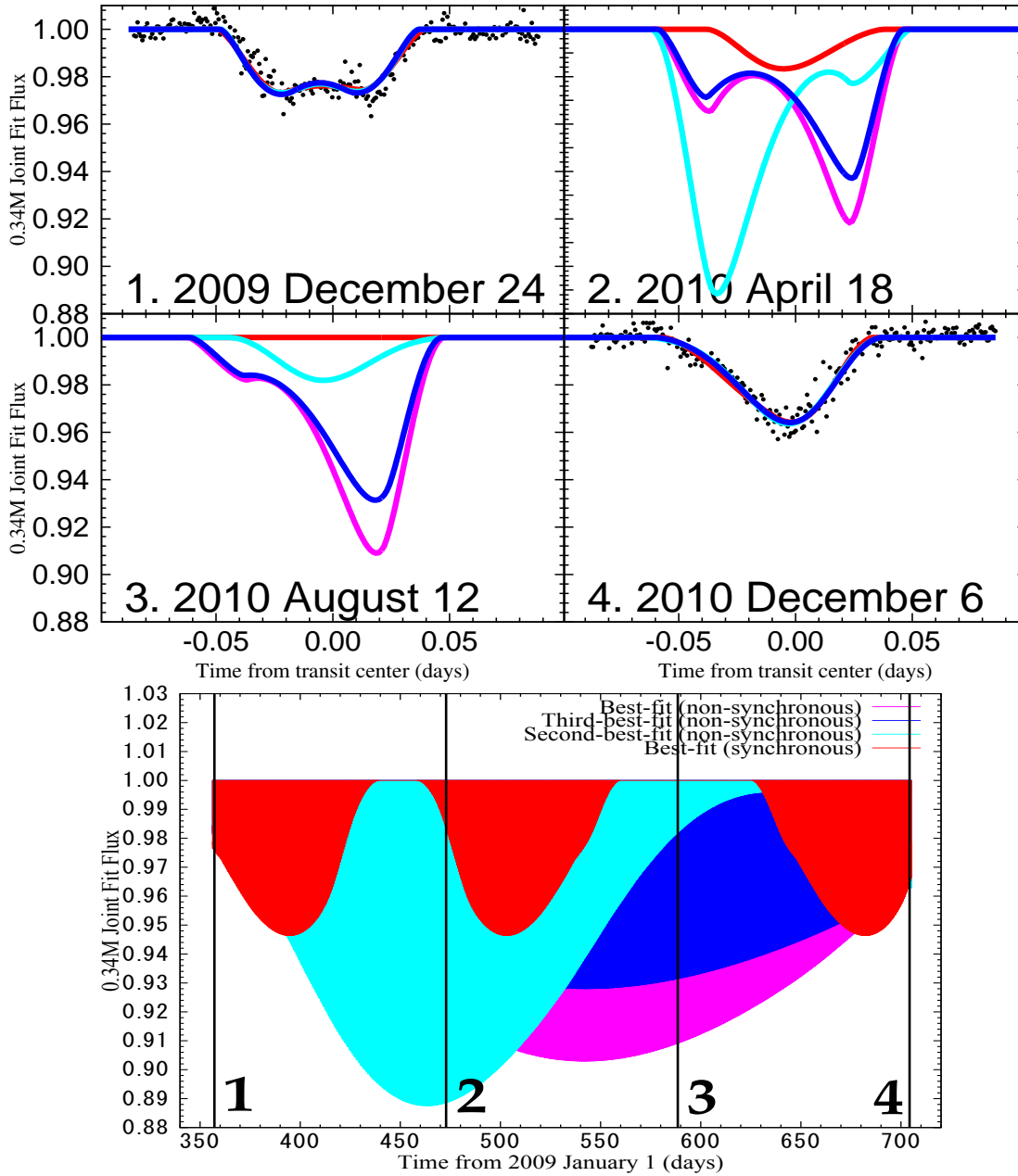


Figure 5.8: The predicted evolution of the light curves for the four solutions in Table 5.2 from 2009 to 2010 observation epoch for  $M_{\star} = 0.34M_{\odot}$ . The bottom panel illustrates the whole evolution from 2009 (leftmost vertical line) to 2010 (rightmost vertical line). The four vertical lines are drawn for every four months, each of which corresponds to the enlarged graph at the top panel. The best solution with the synchronous condition is denoted as red lines, while magenta, cyan and blue are for the best, second-best and third-best solutions without the synchronous condition, respectively.

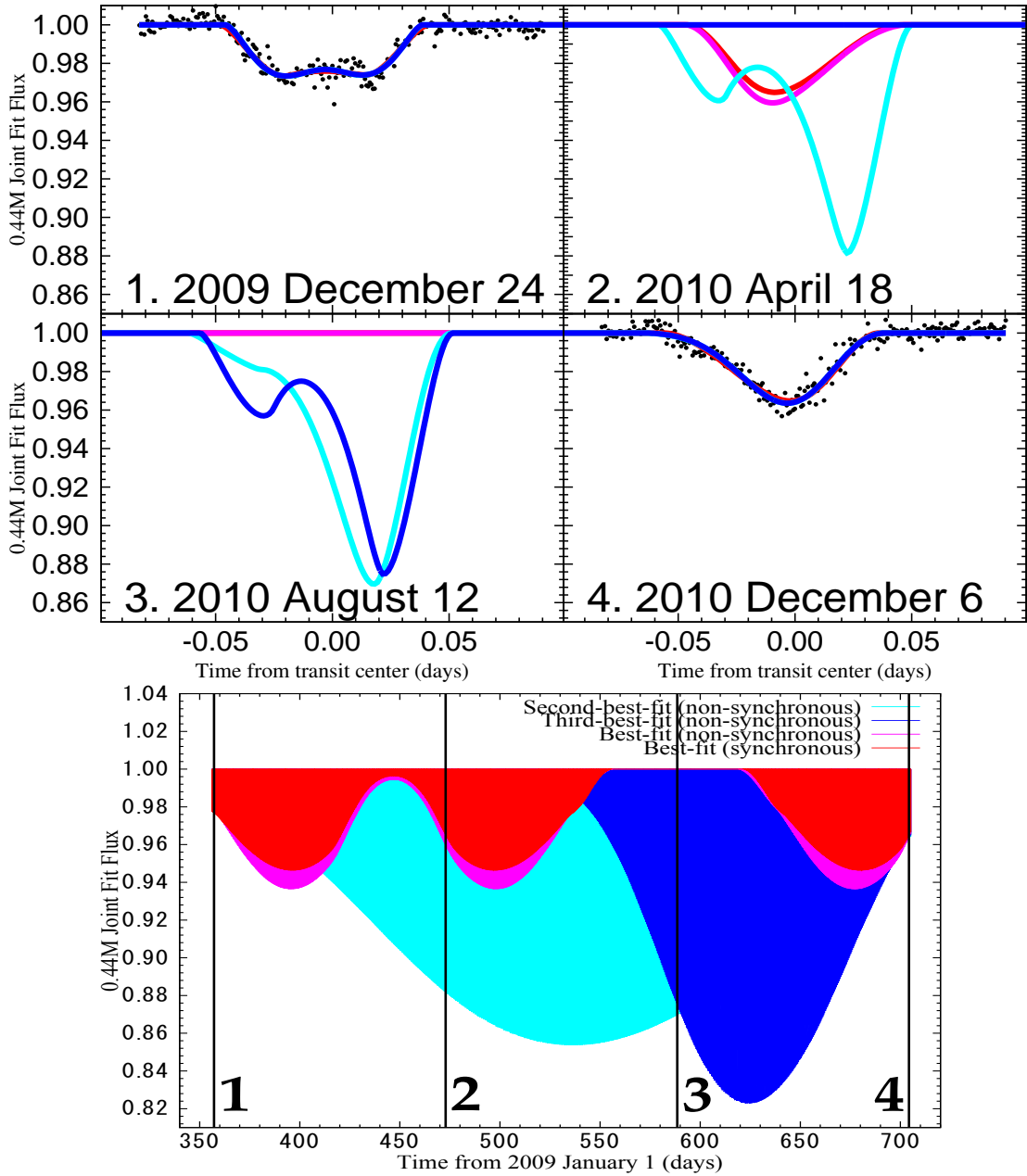


Figure 5.9: Same as Figure 5.8, but for  $M_{\star} = 0.44M_{\odot}$ .

solutions without the synchronous condition, respectively. Figures 5.10 and 5.11 imply that some epochs during KAO photometric observation are available to distinguish these solutions since their predicted transit depth differs by several percents. Specifically for  $M_{\star} = 0.34M_{\odot}$ , the difference is expected to be close to 10% at the first term of the observation (compare cyan and the others during 2014 November; top graphs at the top panel in Figure 5.10). Or for  $M_{\star} = 0.44M_{\odot}$ , the difference is estimated to be about 3% at the later term of the observation (compare blue and the others during 2015 January;

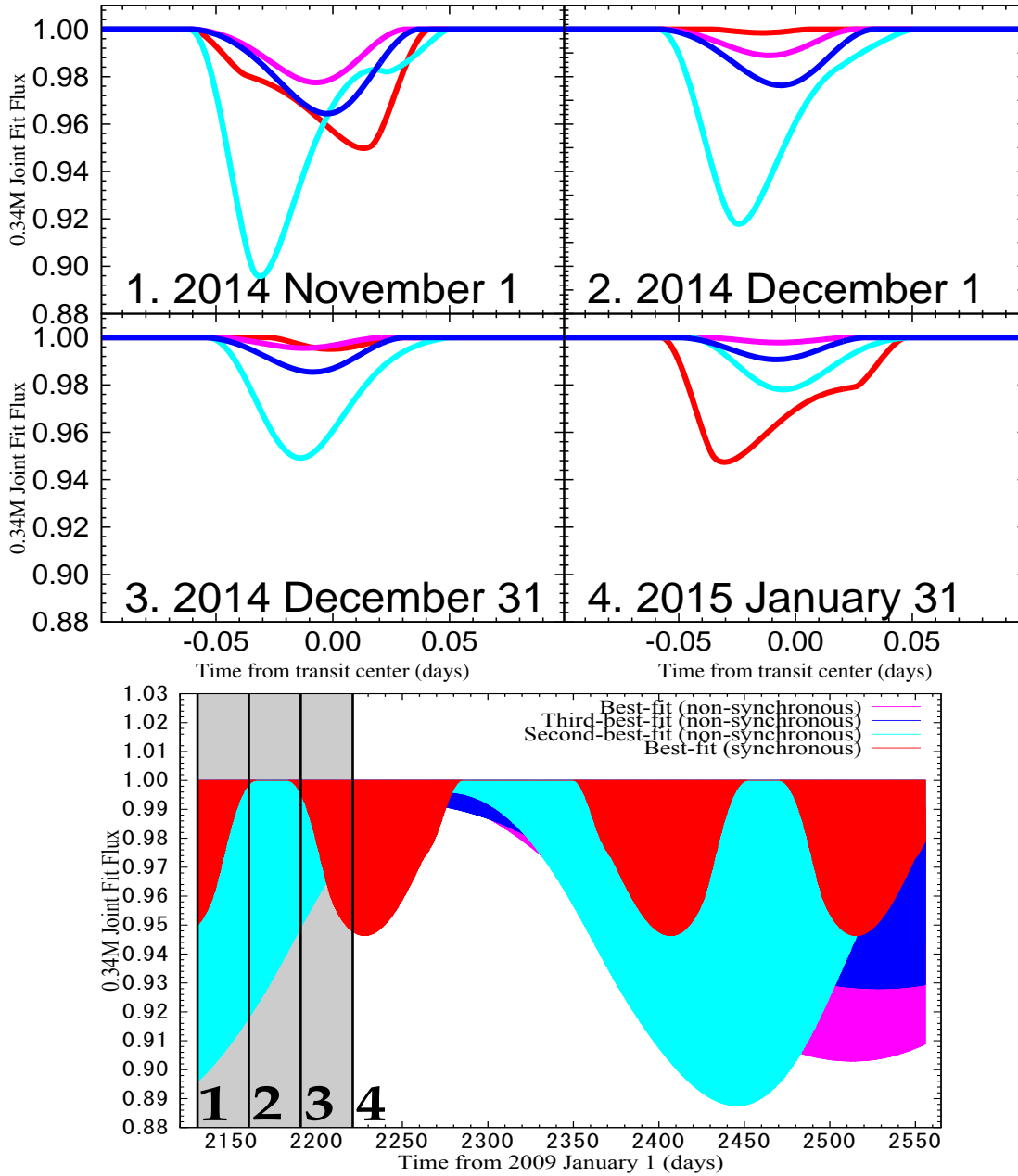


Figure 5.10: The predicted evolution of the light curves for the four solutions in Table 5.2 from 2014 November 1 to 2015 December 31 for  $M_{\star} = 0.34M_{\odot}$ . The bottom panel illustrates the whole evolution. The four vertical lines are drawn for every one month during the observational term by KAO (light gray region), each of which corresponds to the enlarged graph at the top panel. The best solution with the synchronous condition is denoted as red lines, while magenta, cyan and blue are for the best, second-best and third-best solutions without the synchronous condition, respectively.

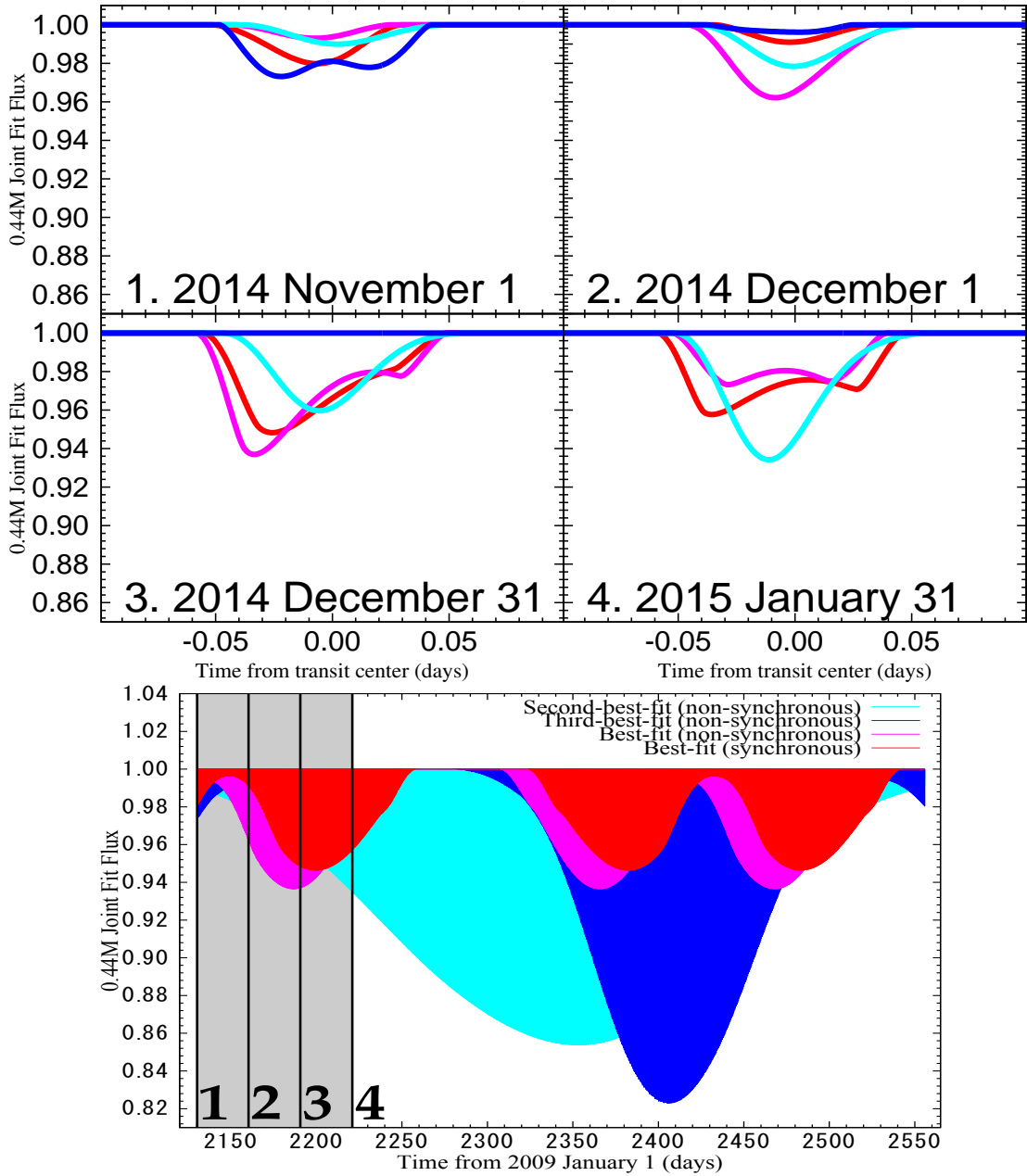


Figure 5.11: Same as Figure 5.10, but for  $M_{\star} = 0.44M_{\odot}$ .

bottom graphs at the top panel in Figure 5.11). It is worthwhile emphasizing that these differences of several percents are detectable by the facilities in KAO.

### 5.6.3 The possibility for the detection of the planetary spin

Recently the planetary spin has been attracting more and more attention. The planetary spin periods and directions in the solar system are well measured and widely known. As

for spin periods, they are estimated to be  $\sim 59$  days for Mercury,  $\sim 117$  days for Venus,  $\sim 24$  hours for Earth,  $\sim 25$  hours for Mars,  $\sim 10$  hours for Jupiter,  $\sim 10$  hours for Saturn,  $\sim 17$  hours for Uranus and  $\sim 16$  hours for Neptune. Among them, Mercury and Venus are now considered to be under the influence of the tidal interaction with the Sun and their rotations are already significantly spun down to approach their orbital periods. Moreover, Spin directions with respect to orbital planes are measured to be  $< 0^\circ.027$  for Mercury,  $\sim 117^\circ$  for Venus,  $\sim 23^\circ$  for Earth,  $\sim 25^\circ$  for Mars,  $\sim 3^\circ$  for Jupiter,  $\sim 25^\circ$  for Saturn,  $\sim 98^\circ$  for Uranus and  $\sim 28^\circ$  for Neptune. Among them, Uranus is widely known for its sideways rotation and Venus is famous for its turned-over rotation, whose origins remain poorly understood. The current frequency and direction of the planetary spin are expected to result from the accretion of the angular momentum during planetary formation phase. Therefore, the spin rate and direction straightly reflect the angular momentum accumulation through the planetesimal collision/accretion process and subsequent gas accretion process that planets experienced during their formation stage. Since the exoplanetary samples whose spin rate and direction are detected simultaneously definitely contribute to reveal such processes, the estimation of the spin states in the exoplanetary systems is the important challenge.

The detection of the planetary spin had not been realized for long time. This is mainly because the effect of the planetary spin on the observational data is so tiny that noises on the data from any observational facilities conceals the signatures of planetary spin. However recent great improvements on the observational precision and accuracy, for example the launch of Kepler satellite, are now creating new scientific field of approaching the planetary spin effect. Recently Snellen et al. (2014) succeeded in estimating the planetary equatorial spin velocity of  $\beta$  Pictoris b to be  $\sim 25$  km/s. This work comes from the investigation of the rotationally-induced broadening of planetary thermal emission line that is obtained by direct imaging method. This indicates that a young gas giant  $\beta$  Pictoris b rotates significantly faster than any planets in our solar system. To say further, Zhu et al. (2014) achieved the simultaneous detection of both planetary spin period and direction to be  $\sim 1.6$  hours and  $\sim 70^\circ$  with respect to its orbital plane for Kepler-39 b. In this work planetary spin rate and direction are measured through the analysis of the planetary rotationally-induced oblateness on the Kepler transit light curves. To do that they investigated the slight deformation of the transit light curves induced by the elliptical shape of the transiting planet, which was far from available without extreme precision and accuracy of the Kepler data. To sum up, these successful works on the detection of planetary spin represent that new astronomical generation is approaching where the investigation of planetary spin effect is within our scientific reach.

As for the planetary spin, some interesting suggestions are also given by this work. The precession model derived as Lagrange's planetary equations in chapter 3 cannot treat the planetary spin because they are formulated analytically with the assumption that the orbiting planet is point-mass in the absence of rotational angular momentum. Therefore, we performed the numerical integration of the EOM in Appendix D (equation D.50  $\sim$  equation D.52) in order to assess the effect of the planetary spin on the dynamical evolution of the system. Although also in the PTFO 8-8695 system the planetary spin

angular momentum is smaller in magnitude than that of the star by about four orders of magnitude ( $|\mathbf{S}_p|/|\mathbf{S}_\star| = \frac{\tilde{C}_p}{\tilde{C}_\star} \frac{M_p}{M_\star} \left(\frac{R_p}{R_\star}\right)^2 \frac{\omega_p}{\omega_\star} \sim 10^{-4}$ ), the planetary spin is found to be significantly influential on the nodal precession by our numerical calculations. Exactly speaking, the planetary spin angular momentum makes total angular momentum vector ( $\mathbf{S}_\star + \mathbf{L} + \mathbf{S}_p$ ) slightly deviate from the summation of stellar spin and planetary orbital motion ( $\mathbf{S}_\star + \mathbf{L}$ ), which slightly modifies the architecture of the nodal precession. Such difference appears in the resulting precession period. The precession period deviates from that in  $\mathbf{S}_p$ -less case by several days, depending on the planetary spin frequency and direction. Unfortunately the current data is so noisy that we cannot pick up such a tiny signal induced by the planetary spin. However, future observational data that will be provided with higher precession and accuracy could make it possible to detect of the planetary spin in the oblate star-planet systems. The formulations necessary in such circumstances are already in our possession, as shown in Appendix D.

#### 5.6.4 Tidal evolution of PTFO 8-8695 system

The results and discussion so far are all focused on the short term evolution of the system; the nodal precession whose expected time scale is several hundred days. In addition to such a short term behavior, long term evolution of the system also presents another perspective to get insight into the nature of the pre-main-sequence star and close-in planet system. As introduced in chapter 1, planetary system with close-in planets cannot avoid the influence of the tidal interaction between the star and planet, which is dominant for the long term evolution of the system. Since the tidal force between the star and planet has the dependence on their separation of order of -3 ( $F_{\text{tide}} \propto r^{-3}$ ) unlike the inverse square law for the Newtonian gravity ( $F_{\text{grav}} \propto r^{-2}$ ), the tidal force becomes stronger as the planet is located closer to the central star. The orbital semi-major axis of the PTFO 8-8695 b is so small ( $a \leq 2R_\star$ ) that we need to take into account the tidal effect when pursuing the long term evolution of PTFO 8-8695. The introduction and formulation of the standard equilibrium tidal model are presented in Appendix D.3. Note here that the two new parameters show up when evaluating the effectiveness of the tidal effect, Love number  $k_2$  and tidal delay time  $\Delta t$ . The Love number and tidal delay time both refer to the fluid property of the central star. The former is in terms of stellar elasticity against the stress and the latter is in terms of the delay of the response of the stellar tidal bulge induced by the tidal force from the planet. In general cases, the effectiveness of the tidal force is argued with the tidal quality factor,  $Q$ , which is the combination of  $k_2$  and  $\Delta t$  as  $Q \propto 1/(k_2 \times \Delta t)$ . Note that larger value of  $Q$  corresponds to weaker tidal effect.

All calculation to pursue the tidal evolution of the system was performed by numerical integration of equation (D.61)  $\sim$  equation (D.63). The test calculation employing the values of Love number and tidal delay time estimated for the Sun ( $k_2=0.028$  and  $\Delta t=0.1$  s) indicates that tidal effect leads to the planetary orbital decay ( $a \rightarrow 0$ ) with the time scale of order of  $10^4$  yrs, which is two orders of magnitude smaller than the age of the central star PTFO 8-8695 (2.6-2.7 Myrs) as shown in Figure 5.12. This rapid orbital decay is totally inconsistent with the observational picture that favours the existence of

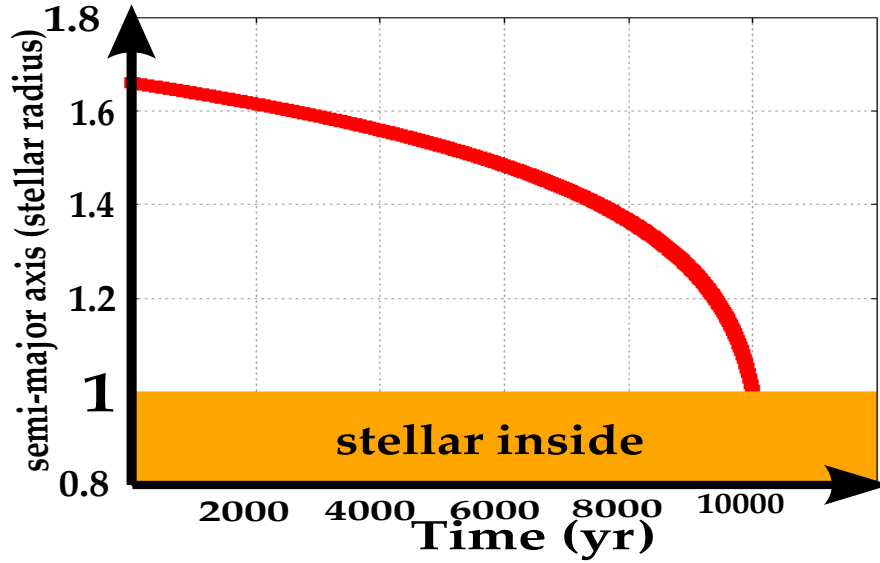


Figure 5.12: Time evolution of the planetary semi-major axis with the Love number of  $k_2 = 0.028$  and tidal delay time of  $\Delta t = 0.1$  s, both of which are estimated for the Sun. The vertical axis is normalized by the stellar radius of PTFO 8-8605, and stellar inside is denoted as the orange region.

close-in planet in PTFO 8-8695 system. Since the values above are those estimated for the Sun, however, there is no need for them to be the same as those of the pre-main-sequence star PTFO 8-8695. By estimating the reasonable value (or lower constraint) of tidal quality factor  $Q$  for PTFO 8-8695, on the contrary, one can approach the internal structure and fluid properties of pre-main-sequence stars which are poorly known today due to the scarcity of the observed samples. Such new insights on the physical properties of pre-main-sequence stars are expected to shed light on the stellar evolution mechanism which leaves many questions today.

# Chapter 6

## Summary and Future Prospects

Recent observations have detected a large number of exoplanets and revealed the diversity of exoplanetary systems beyond our conventional perspective on the planetary systems. And it is now required to characterize the observed exoplanets for the better understanding of the formation scenario of the planetary systems. In this thesis, we characterized a transiting planetary system PTFO 8-8695 through the unexpected shapes and time-variability of its transit light curves taken by Palomar Observatory in 2009 and 2010. For that purpose, we formulated the equations necessary for the dynamical evolution of the system and modelled the light curve generating scheme. The pioneering work on this planetary system, Barnes et al. (2013), adopted the spin-orbit synchronous condition under which the stellar rotational period is synchronized to the planetary orbital period. However, the standard tidal theory suggests that the spin-orbit synchronous condition is unphysical and difficult to hold in PTFO 8-8695 system. Based on this motivation, we re-analyzed PTFO 8-8695 system basically following the procedure in Barnes et al. (2013), but adopting stellar spin period not as a fixed value to the planetary rotational period but as a fitting parameter. The achievements of our study are summarized as follows.

1. Discovery of the diversity of the solutions in the absence of the spin-orbit synchronous condition. Before the main fittings, we performed the 2009, 2010 individual fit and 2009-2010 joint fit with the spin-orbit synchronous condition for the purpose of comparing the results with those by Barnes et al. (2013). We found that our fits provided almost identical results with those by Barnes et al. (2013), which implies that both our equations for the dynamical evolution of the system in chapter 3 and our light curve model in chapter 4 operate correctly. The main fittings indicated that a variety of solutions are possible for this planetary system in the absence of the spin-orbit synchronous condition, all of which present  $\chi_r^2$  values comparable to or slightly better than that with synchronous condition (Tables 5.2 and 5.3). In fact, the differences of  $\chi_r^2$  values among those solutions are so tiny that it is premature to conclude that one solution out of several possible ones definitively corresponds to the true solution while all others fail. It should be noted here that although the transit light curves by these solutions coincide at the epochs of 2009 and 2010 observations, they are expected to be totally different with each other at

other epochs. To say further, utilizing the differences in the precession period is the easiest way to distinguish the possible solutions because the predicted precession periods among them vary greatly. Specifically, the precession period is estimated to be 1399, 819 and 1425 days for the best, second-best and third-best solutions for  $M_{\star} = 0.34M_{\odot}$ , respectively, and 281, 1289 and 594 days for the best, second-best and third-best solutions for  $M_{\star} = 0.44M_{\odot}$ , respectively. This diversity in the precession period inevitably results in the difference in the shape of the transit light curves at the epochs of future observation, from which the selection of the true solution becomes possible. We provided the future prediction of the light curves as a groundwork for such future observations (Figures 5.10 and 5.11). We are now collaborating with the researchers in Kyoto Sangyo University and under the process of acquiring the photometric data of PTF0 8-8695 during 2014 November - 2015 January. The additional transit light curves from such observations are expected to serve as the clues not only to select the possible solutions by this work, but also to constrain the system parameters strongly.

2. Specification of the demerits of the phase-fold of transit light curves in Barnes et al. (2013). The phase-fold makes several transit light curves combined into one. Since in particular the 2009 observational term spreads over about 1.5 months, however, this procedure adopted in Barnes et al. (2013) would drop the variability of the transit light curve during the observational intervals. By reproducing the time evolution of the transit light curve during 2009 observational term, we pointed out that 1.5 months interval brings about the significant change in light curves (Figure 5.6). Therefore it is concluded that a part of the information in original data is lost by phase-fold. The re-analysis of the current data without phase-fold is an important issue to be tackled with.
3. Prospects of the detection of the planetary spin. The effect of the planetary spin on the architecture of the precession was checked with our general formulation in Appendix D. Although the planetary spin angular momentum is smaller in magnitude than stellar spin or planetary orbital angular momenta by several orders of magnitude, it is shown that the planetary spin alters the precession period by several days, depending on the spin frequency and direction. Thus the accumulation of the observational data could open the path to investigate the exoplanetary spin frequency and direction. Since the planetary spin state is expected to reflect the angular momentum accumulation history that the proto-planets had experienced, the estimation of the spin state contributes to reveal the angular momentum transportation mechanism within the protoplanetary disk which is not well known today.
4. Tidal evolution of the pre-main-sequence star system. Besides the short term evolution of the system (the nodal precession with periods of several hundred or thousand days), we pursued the long term evolution of PTF0 8-8695 system taking into account the tidal effect between the central star and the planet. And then we found that the results of the evolution with the tidal quality factor  $Q$  whose value is identified with that of the Sun are incompatible with the current configuration of

---

PTFO 8-8695 system. Specifically, the planet is predicted to fall into the central star within the time scale shorter than the age of the system (Figure 5.12). Since the  $Q$  value reflects the internal profiles of the star and planet, identification of the  $Q$  value consistent with the current architecture of the system may make it possible to investigate the internal structures of pre-main-sequence star or hot Jupiter which remain unclear until today.

Although the statistics on the spin-orbit angle  $\phi$  greatly contributes to reveal the origin of the widely-observed close-in planets, the measurement of  $\phi$  has not been well performed for the younger systems until today. This is because the RM effect, which is the most popular method to detect the projected spin-orbit angle  $\lambda$ , is hard to be applied to younger systems since faster rotation and higher noise level of younger stars make it difficult to detect the stellar spin signals by the observations. On the other hand, the nodal precession with gravity darkening effect becomes more available for the detection of  $\phi$  as the star rotates faster. This is because the larger extent of the stellar rotational deformation appears as the more drastic variability of the transit light curves. This method for the measurement of  $\phi$  making use of the nodal precession constructs the complementary relation with the measurements with the RM effect, and is expected to be successful as the standard model for the estimation of  $\phi$  for the rapid rotator systems (in general, younger systems).

The wavelength dependence of the shapes of transit light curves could also open the road of providing severer constraints on the system parameters. Originally, transit light curves are usually near-achromatic since planetary occultation basically gives no distinction for the wavelengths, and all wavelengths are united to construct the actually-observable stellar flux. However, both limb-darkening effect and gravity darkening effect have the wavelength dependence for their effectiveness. Thereby transit light curves show different shapes when seen by different wavelengths. The monochromatic transits at  $0.658 \mu m$  is assumed in this work following Barnes et al. (2013), however, the future transit observations with different wavelengths are expected to provide other insights into the properties of the system. In principle, the future observation for the stronger constraints on the system parameters is not necessarily performed with the spectroscopical facilities which usually require much equipment efforts, but can be achieved by only photometric observations at the several wavelengths.



# Acknowledgments

I would like to express my sincere gratitude to all of my collaborators. I could not have completed this dissertation without their help.

In particular, I would like to gratefully express thanks to my supervisor, Prof. Yasushi Suto, who provided me the opportunity to study and enjoy the exoplanetary science. He always seriously listened to my questions or ideas, and gave me precious advices on my research based on his great insight into various aspects of exoplanets. His way of thinking and his point of view on how science and people in science should be always encouraged me to put forward my research. I am also grateful to Yuxin Xue, who gave me various techniques of programming and spared time for me to check my code. I also sincerely acknowledge Kento Masuda, who taught me the dynamics of the planetary systems and the way of analysing the transit light curves from the beginning. He also readily took charge of formulating the light curve model, and made great effort to improve it. Furthermore, every day's insightful discussion with him always motivated me and triggered my research to go ahead. Also to all other people in UTAP, the University of Tokyo Theoretical Astrophysics group, I wish to show my gratitude. They attended my seminars, provided me helpful advices and gave me comfortable environments for my research.

Besides the UTAP members, I would like to show my deepest gratitude to Prof. Julian van Eyken and his collaborators, who willingly made the data by Palomar Observatory available to us, and Prof. Masahiro Ikoma, who got in contact with them. This work could never have been finished without their kindness. I also feel thankful to Prof. Atsunori Yonehara and his colleagues in Kyoto Sangyo University, who are now trying to obtain additional photometry on PTFO 8-8695.

Finally, I greatly thank my parents, Tsutomu Kamiaka and Junko Kamiaka. They always respected my decisions on my career judgement and supported me in all aspects.



# Appendix A

## Planet Formation Theory

### Appendix A.1 Conventional theory

Until a couple of decades ago, the solar system was the unique planetary system, and it consists of planets, dwarf planets and many other small objects including asteroids, Kuiper-belt objects, the Oort clouds and so on. Among them, planets have been known and been major research areas in physics, astronomy and planetary science. They are classified into mainly three groups; “terrestrial planets” for the innermost four planets (Mercury, Venus, Earth, Mars), “gas giants” for the intermediate two planets (Jupiter and Saturn) and “ice giants” for the outermost two planets (Uranus and Neptune). Since we did not know the architecture of other planetary systems before the first detection of an exoplanet, planet formation scenario had been developed and improved for the purpose of the natural explanation to the architecture of the solar system. The most successful planet formation theory, the Hayashi model, greatly attracts the attention and is widely accepted (Hayashi et al. 1985). The basic processes are briefly summarized as follows.

1. In the phase of the formation of the central protostar through the contraction of the molecular clouds, some portion of gas and dust components that retains their primordial angular momentum cannot accrete into the protostar and hence form the protoplanetary disk around the protostar.
2. The dust component within the disk is gradually settled into the mid-plane region, providing the environment suitable for the formation of planetesimals through accretion.
3. Mutual collisions among planetesimals lead to the formation of the proto-planets. This process is more likely to take place in the outer region of the snow line beyond which the stellar irradiation is not so severe that the dust particles are easy to coagulate. Therefore, the proto-planets within the snow line tend to be relatively smaller (known as terrestrial planets), while the solid cores beyond the snow line tend to become massive enough to trigger the subsequent acquisition of the gas envelopes to become gas giants.

Another important insight from this model is concerned with the orbital inclinations and eccentricities of the planets. Assuming that the stellar equatorial plane and protoplanetary disk are intrinsically coplanar, the Hayashi model predicts the resulting distribution of the planetary orbits to be coplanar and aligned with stellar equatorial plane, since all planet formation processes are considered to occur within the protoplanetary disk. Moreover, the resulting eccentricity of planets is likely to be close to zero, even if not, cannot be substantially large. This is because the friction of the planets within the protoplanetary disk with disk gas components acts on the planets to suppress their eccentricities to be close to zero.

In conclusion, the architecture of the planetary system that the Hayashi model predicts is the circular and coplanar system where the terrestrial planets reside in the inner part of the planetary system, and gas giants reside in the outer part. The most successful achievement of this model is that it can naturally explain the architecture of the solar system. This planet formation scenario is now known and widely accepted as the core accretion scenario (for example, see Ikoma et al. 2000, Armitage 2010).

## Appendix A.2 Spin-orbit angle distribution and its implication to planet formation theory

It is believed that the discrepancy between the observationally-revealed architecture of the planetary systems and theoretical prediction such as the existence of hot Jupiters, eccentric planets and retrograde planets could be reconciled by a slight modification of the Hayashi model. Specifically, the subsequent orbital migration after the formation of gas giants is responsible for the explanation of the diversity of the exoplanetary systems. According to that idea, some gas giants formed in the outer region of the planetary system are to experience the subsequent orbital migration, leading to the giant planets located at the vicinity of the central star as observational data demonstrate (Ida & Lin 2004). There exist two widely accepted mechanisms as the cause of the inward orbital migration; one is *disk interaction model* (Lin et al. 1996, Bate et al. 2003) and the other is *gravitational scattering model* (Wu & Murray 2003, Nagasawa & Ida 2011). The detailed explanation of these mechanisms with the help of analytical and/or numerical studies are beyond the scope of this paper, but we summarize their basic pictures briefly.

Disk interaction model is based on the idea that gas giants within the protoplanetary disk suffer from the friction with the remaining gas component of the disk, and exchanges their angular momentum. In this model, gas giants gradually shrink their orbits by providing their angular momentum to the surrounding gas components, and finally reach the vicinity of their central stars. This type of migration is called Type I/II migration depending on the mass of gas giants (Type I for less massive gas giants, Type II for massive gas giants). Especially Type II migration predicts that migrating gas giant open the gap around it within the disk (Klahr & Kley 2006, Duffell & MacFadyen 2013). The gas component flows into the gas giant from inner region of the gap and goes away into

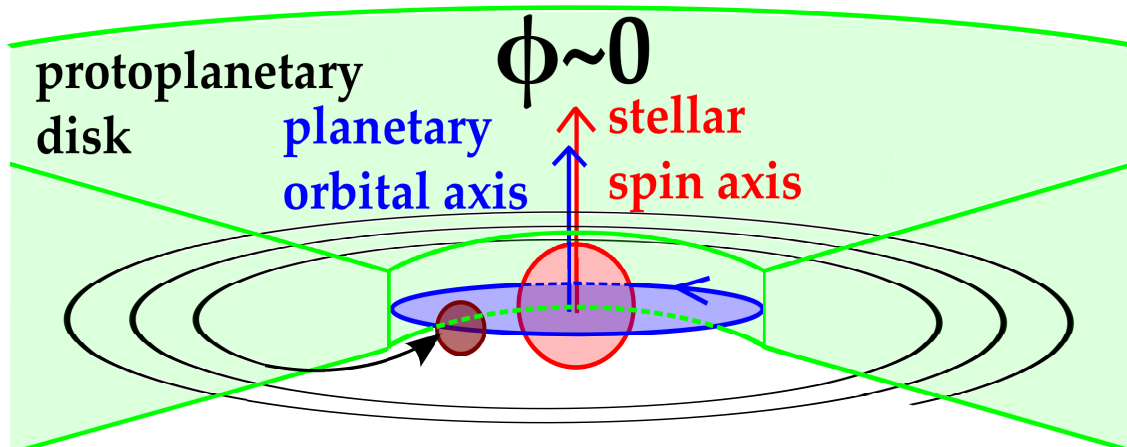


Figure A.1: Schematic illustration of the disk interaction model. The stellar spin and planetary orbital axes are denoted as the red and blue arrows, respectively. The spin-orbit angle, the angle between the stellar spin and planetary orbital axes is defined as  $\phi$ . The path of planetary orbital migration within the protoplanetary disk (light green region) is shown as the solid spiral.

the outer region of the gap. Thus the gas attains positive angular momentum from the planetary orbit, and gas giants migrate inward.

The gravitational scattering model concerns the dynamical evolution of the system after the protoplanetary disk dissipation. This model assumes the planetary system harbouring two or more gas giants orbiting around the central star. At the close encounter between gas giants, mutual gravitational interaction blows away one planet to outer orbit or even eject it from the planetary system. In turn, the counterpart planet falls into inner orbit to be observed as hot Jupiter, because total angular momentum of two gas giants is conserved. This model predicts that the resulting inner gas giant tends to show

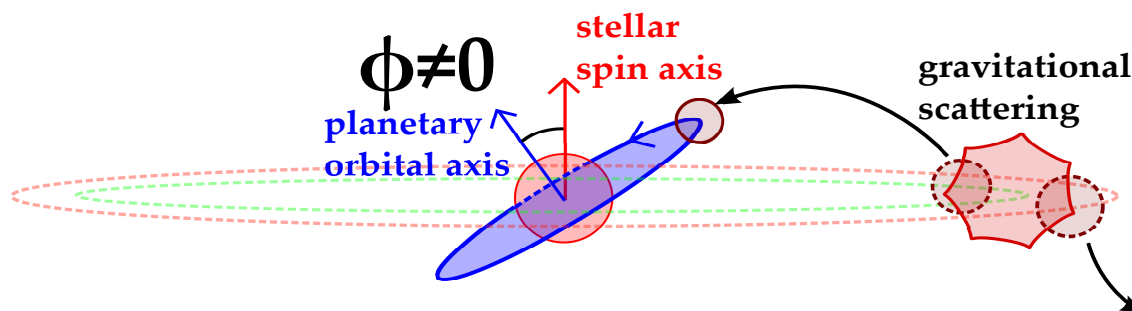


Figure A.2: Schematic illustration of the gravitational scattering model. The stellar spin and planetary orbital axes are denoted as the red and blue arrows, respectively. The spin-orbit angle, the angle between the stellar spin and planetary orbital axes is defined as  $\phi$ . The dashed and solid lines are the planet and its orbit before and after the gravitational scattering, respectively.

high orbital inclination with respect to the central star's equatorial plane, and/or high eccentricity. In fact, the radial velocity measurement of the exoplanetary systems is now accumulating the samples showing high eccentricity signature (Figure 1.1), which indicates that this dynamical scenario is capable of explaining the origin of such hot Jupiters.

So far, it is not yet clear which model is mainly responsible for the observed distribution of the hot Jupiters or their relative contribution in the actual planetary systems, since both models are consistent with the current data. Here, the key parameter to distinguish between the two models is the *spin-orbit angle*,  $\phi$ , the angle between the stellar spin axis and planetary orbital axis. As mentioned above disk interaction model predicts the planetary orbital axis is aligned with the stellar spin axis (namely, spin-orbit angle  $\phi$  is close to  $0^\circ$  (Figure A.1), whereas gravitational scattering model predicts spin-orbit angle  $\phi$  is distributed broadly (Figure A.2). Therefore, statistics of the measured  $\phi$  reveals which planet migration model is dominant in the actual planetary systems.

We here should pay attention to the possibility that the spin-orbit angle  $\phi$  evolves with time due to the tidal effect with the central star after hot Jupiters reached the vicinity of the central star (Hut 1981, Barker & Ogilvie 2009 and Correia et al. 2011). In general, the tidal force between star and planet makes (i) planetary semi-major axis damp, (ii) orbital eccentricity damp (approaching circular orbit), (iii) stellar/planetary spin frequency and orbital frequency be synchronized and (iv) stellar equatorial plane and planetary orbital plane be coplanar ( $\phi \rightarrow 0^\circ$ ). Therefore the determined spin-orbit angle  $\phi$  from observational data may reflect the degree of the tidal effect that the star and planet experience after the inward orbital migration of gas giants. Thus this process may conceal the initial memory of the orbital migration mechanism and prevent us from simple interpretation to  $\phi$ . The strength of the tidal effect is also another important problem.

Tidal dissipation is thought to occur mainly in the convective envelope of the central star, whose depth is sensitive to the spectrum type of the star. Some works (Winn et al. 2010, Dawson 2014) claim that the tidal effect becomes stronger for  $T_{\text{eff}} < 6100\text{K}$  cases (with thick convective envelope) than for  $T_{\text{eff}} > 6100\text{K}$  cases (with tiny convective envelope). This fact makes the problem more complicated because we have to take the effective temperature of the star into account for the estimation of the spin-orbit angle  $\phi$ .

The Rossiter-McLaughlin effect (hereafter, the RM effect) is the most popular method to measure the spin-orbit angle (Rossiter 1924 and McLaughlin 1924). In general, stellar rotation causes the stellar flux from the stellar portion approaching the observer to be blue shifted, while the stellar flux from the stellar portion receding the observer to be red shifted, resulting in the broadened spectra lines. When the planet is prograde and the transit event is seen by edge-on, planet hides first the approaching and then receding portion of the stellar disk. Accordingly, the spectrum lines from the star are as a whole to be red and then blue shifted. The extent that the spectrum lines are blue/red shifted and its time variation differ according to (i) the direction of stellar spin axis (stellar obliquity), (ii) the direction with which the transiting planet enters the stellar disk and (iii) the impact parameter of the transit, from which one can measure the spin-orbit angle *projected onto the sky plane*,  $\lambda$ . Recently large number of measurement of spin-orbit angle  $\phi$  has been performed, some of them reporting spin-orbit aligned cases and the others

are misaligned (Hirano et al. 2012, Albrecht et al. 2013, Queloz et al. 2000, Winn et al. 2005, Hirano et al. 2011 and Walkowicz & Basri 2013). Figure A.3 shows the observed distribution of projected spin-orbit angle  $\lambda$ . Although it can be seen that observed samples have the tendency to be concentrated near alignment state  $\lambda \sim 0^\circ$ , significant fraction of planetary systems is highly misaligned, even in retrograde orbits.

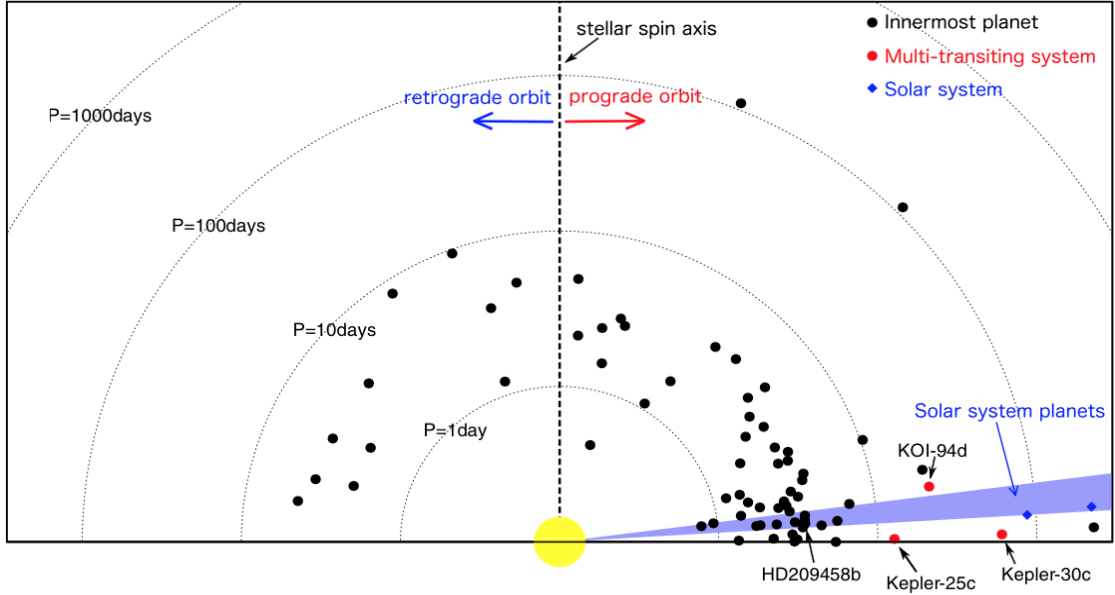


Figure A.3: Observed distribution of the projected spin-orbit angle  $\lambda$  via the RM effect as of August 20, 2013. Black circles denote the inner-most in single transiting systems, while red circles denote the largest planets in the multi-transiting systems. The solar system planets are depicted as blue diamonds. Figure taken from Xue et al. (2014).

The sensitivity of the RM effect to measure  $\lambda$  declines when the central star rotates rapidly. This is partly because rapid rotation causes the observed spectra lines to be severely broadened, which makes the blue/red shift difficult to be clearly analyzed. In general, magnetic braking mechanism is thought to decelerate the stellar rotation with time, leading to sharper spectra lines as the star becomes older. Therefore in other words, the RM effect is hard to be applied to the pre-main-sequence stars since they are usually considered as rapid rotators. Another reason for this tendency is that younger stars are so active that higher noise level may inhibit us from obtaining precise and accurate observational signals. Thus almost all successful works with the RM effect are focused on the matured main-sequence stars. The spin-orbit angle in the younger system, however, has not been seriously investigated until today.

Although projected spin-orbit angle  $\lambda$  is useful in revealing the configuration of the directions of stellar spin or planetary orbit in the observing system,  $\lambda$  is different from the three dimensional spin-orbit angle  $\phi$ . To say further,  $\lambda$  is always smaller than  $\phi$  because it is projected quantity. Recently, a new method that combines the RM effect and stellar seismology becomes available in estimating  $\phi$  (Huber et al. 2013, Benomar et al. 2014)

since the investigation of the stellar seismology provides the information on the direction of the stellar spin.

In conclusion for this chapter, both statistics of the observational data on spin-orbit angle  $\phi$  and detailed understanding on the tidal effect responsible for the time evolution of  $\phi$  are definitely required in order to make clear the actual formation scenario of widely observed hot Jupiters.

# Appendix B

## Keplerian Motion

### Appendix B.1 Planetary position and velocity in terms of true anomaly

Under the condition where the central star and the planet can be assumed to be the point masses, the orbit of the planet is derived in analytical form as an elliptical motion from Newton's equation, which is so-called two-body problem. In this chapter, the index 0 is to denote the central star, while 1 is for the planet. The following contents are easier to understand with Figures 3.1 and 3.2. The equations of motion in the inertial frame with star (mass  $M_0$ ) and planet (mass  $M_1$ ) under the gravitational interactions are given by

$$M_0 \ddot{\mathbf{r}}_0 = +G \frac{M_0 M_1}{r} \mathbf{r} \quad (\text{B.1})$$

$$M_1 \ddot{\mathbf{r}}_1 = -G \frac{M_0 M_1}{r} \mathbf{r}, \quad (\text{B.2})$$

with gravitational constant  $G$ , position vectors of the star  $\mathbf{r}_0$  and the planet  $\mathbf{r}_1$ , and the relative motion of the planet with respect to the star  $\mathbf{r} = \mathbf{r}_1 - \mathbf{r}_0$ . From these equations, the time evolution of the relative motion  $\mathbf{r}$  is calculated by solving

$$\ddot{\mathbf{r}} + G(M_0 + M_1) \frac{\mathbf{r}}{r} = 0, \quad (\text{B.3})$$

whose integration leads to

$$\mathbf{r} \times \dot{\mathbf{r}} = \mathbf{h}, \quad (\text{B.4})$$

where  $\mathbf{h}$  is the constant vector perpendicular to both  $\mathbf{r}$  and  $\dot{\mathbf{r}}$ . Therefore the planetary orbit lies within the plane normal to  $\mathbf{h}$ , and never changes its direction with time.

In order to solve equation (B.3), we adopt the polar coordinate centered on the star, whose position, velocity and acceleration vectors are written as

$$\mathbf{r} = r \hat{\mathbf{r}} \quad (\text{B.5})$$

$$\dot{\mathbf{r}} = \dot{r}\hat{\mathbf{r}} + r\dot{\theta}\hat{\boldsymbol{\theta}} \quad (\text{B.6})$$

$$\ddot{\mathbf{r}} = (\ddot{r} - r\dot{\theta}^2)\hat{\mathbf{r}} + \left[ \frac{1}{r} \frac{d}{dt}(r^2\dot{\theta}) \right] \hat{\boldsymbol{\theta}}, \quad (\text{B.7})$$

where  $\hat{\mathbf{r}}$  and  $\hat{\boldsymbol{\theta}}$  are the unit vectors along with radial and azimuthal directions, respectively. Substitution of equations (B.5) and (B.6) into equation (B.4) gives

$$\mathbf{h} = r^2\dot{\theta}\hat{\mathbf{z}}, \quad (\text{B.8})$$

with unit vector  $\hat{\mathbf{z}}$  lying along with the normal to orbital plane. The magnitude of this vector

$$h = r^2\dot{\theta} \quad (\text{B.9})$$

remains constant although  $r$  and  $\dot{\theta}$  may vary with time. Therefore, the the area element  $dA$  swept by the planetary position vector during the time interval  $dt$  is

$$dA = \int_0^r r dr d\theta = \frac{1}{2} r^2 d\theta, \quad (\text{B.10})$$

and thus

$$\dot{A} = \frac{1}{2} r^2 \dot{\theta} = \frac{1}{2} h = \text{constant}, \quad (\text{B.11})$$

which states that the star-planet line sweeps the equal areas in equal times.

Comparison equation (B.7) with equation (B.3) provides the scalar differential equation,

$$\ddot{r} - r\dot{\theta}^2 = -\frac{G(M_0 + M_1)}{r^2}. \quad (\text{B.12})$$

Transition of the variable  $r$  into  $u = \frac{1}{r}$  and making use of equation (B.9) give

$$\ddot{r} = -h \frac{d^2 u}{d\theta^2} \dot{\theta} = -h^2 u^2 \frac{d^2 u}{d\theta^2}, \quad (\text{B.13})$$

leading to

$$\frac{d^2 u}{d\theta^2} + u = \frac{G(M_0 + M_1)}{h^2}, \quad (\text{B.14})$$

where time derivative was all eliminated. The solution of this equation becomes

$$u = \frac{G(M_0 + M_1)}{h^2} [1 + e \cos(\theta - \varpi)] \quad (\text{B.15})$$

where  $e$  and  $\varpi$  are two constants of integration, and turning back to  $r$  gives

$$r = \frac{p}{1 + e \cos(\theta - \varpi)}, \quad (\text{B.16})$$

with  $p = h^2/G(M_0 + M_1)$ . In general, this kind of solution is applied into three different motions (elliptic orbit including a circle, parabola and hyperbola) depending on the initial conditions of the system. We here consider only elliptic motions and for which

$$p = a(1 - e^2), \quad (\text{B.17})$$

where a constant variable  $a$  is the semi-major axis of the elliptic orbit.  $a$  and the semi-minor axis  $b$  are related through  $e$  by

$$b^2 = a^2(1 - e^2) \quad (\text{B.18})$$

Therefore,  $r$  can be given by

$$r = \frac{a(1 - e^2)}{1 + e \cos(\theta - \varpi)} \quad (\text{B.19})$$

with any given value of  $\theta$ . In addition, the planet is located at the periapse ( $r = a(1 - e)$ ) when  $\theta = \varpi$ , whereas located at the apoapse ( $r = a(1 + e)$ ) when  $\theta = \varpi + \pi$ . Here  $\varpi$  coincides with the angular direction for which the planet lies in the periapse. Then we here define the *true anomaly*  $f$  measured with respect to the periapse direction ( $f = \theta - \varpi$ ), which gives

$$r = \frac{a(1 - e^2)}{1 + e \cos f}. \quad (\text{B.20})$$

If we define the cartesian coordinate centered on the star with  $x$ -axis pointing the direction of the periapse, the position of the planet is represented as

$$x = r \cos f \quad (\text{B.21})$$

$$y = r \sin f. \quad (\text{B.22})$$

The orbital period,  $T$ , can be related to other orbital parameters. Since  $T$  is the time required for the star-planet line to sweep the all elliptic area of the planetary orbit ( $A = \pi ab$ ), so from equation (B.11)

$$T^2 = \left(\frac{A}{\dot{A}}\right)^2 = \left(\frac{\pi ab}{\frac{1}{2}h}\right)^2 = \frac{4\pi^2}{G(M_0 + M_1)} a^3, \quad (\text{B.23})$$

which turns out to be independent of the orbital eccentricity  $e$ . This equation corresponds to the Kepler's third law. We here define the mean motion  $n$  as the planetary orbital frequency,

$$n = \frac{2\pi}{T}, \quad (\text{B.24})$$

which rewrites the Kepler's third law and  $h$ ;

$$G(M_0 + M_1) = n^2 a^3, \quad (\text{B.25})$$

$$h = na^2\sqrt{1 - e^2} = \sqrt{G(M_0 + M_1)a(1 - e^2)}. \quad (\text{B.26})$$

It is useful to write down the analytic expression for the planetary velocity  $v$  as well as the position  $r$  (equation B.20). To proceed, we take scalar product of equation (B.3) with  $\dot{\mathbf{r}}$  and use equations (B.5) and (B.6), leading to

$$\dot{\mathbf{r}} \cdot \ddot{\mathbf{r}} + G(M_0 + M_1) \frac{\dot{r}}{r^2} = 0, \quad (\text{B.27})$$

whose integration provides

$$\frac{1}{2}v^2 - \frac{G(M_0 + M_1)}{r} = C, \quad (\text{B.28})$$

where  $v^2 = \dot{\mathbf{r}} \cdot \dot{\mathbf{r}}$  and  $C$  is the constant of the integration. Equation (B.28) clearly shows that the orbital energy per unit mass is conserved through the planetary orbital motion. With the help of equation (B.6), we obtain

$$v^2 = \dot{\mathbf{r}} \cdot \dot{\mathbf{r}} = \dot{r}^2 + r^2 \dot{f}^2. \quad (\text{B.29})$$

Differentiation of equation (B.20) shows

$$\dot{r} = \frac{r \dot{f} e \sin f}{1 + e \cos f}, \quad (\text{B.30})$$

which can be combined with equations (B.26), (B.20) and (B.26) into

$$\dot{r} = \frac{na}{\sqrt{1 - e^2}} e \sin f \quad (\text{B.31})$$

and

$$r \dot{f} = \frac{na}{\sqrt{1 - e^2}} (1 + e \cos f). \quad (\text{B.32})$$

Therefore we can rewrite equation (B.29);

$$v^2 = \frac{n^2 a^2}{1 - e^2} (1 + 2e \cos f + e^2), \quad (\text{B.33})$$

or

$$v^2 = G(M_0 + M_1) \left( \frac{2}{r} - \frac{1}{a} \right), \quad (\text{B.34})$$

which are the function of  $f$  and  $r$ , respectively.

## Appendix B.2 Planetary position in terms of time

In the previous section, we eliminated the time derivative from differential equations, so we got the planetary position  $r$  in terms of  $\theta$  (equivalently, true anomaly  $f$ ). In this section, we show the way to relate the planetary position and time through several variables and equations. For that, we first rewrite  $\dot{r}$  in terms of  $r$  with the aid of equations (B.20), (B.25), (B.32) and (B.34). It returns

$$\dot{r} = \frac{na}{r} \sqrt{a^2 e^2 - (r - a)^2}. \quad (\text{B.35})$$

This differential equation can be solved by introducing a new variable, *eccentric anomaly*  $E$ , so that  $E$  satisfies

$$r = a(1 - e \cos E). \quad (\text{B.36})$$

Then differential equation is transformed into

$$\dot{E} = \frac{n}{1 - e \cos E}, \quad (\text{B.37})$$

and the solution is given by

$$n(t - t_0) = E - e \sin E, \quad (\text{B.38})$$

where  $t_0$  is to be the constant of the integration which meets  $E = 0$  when  $t = t_0$ . By introducing additional variable *mean anomaly*,  $M = n(t - t_0)$ , it becomes possible to write

$$M = E - e \sin E, \quad (\text{B.39})$$

which is known as *Kepler equation*. It is clear that  $M = f = 0$  when  $t = t_0$ , and  $M = f = \pi$  when  $t = t_0 + T/2$ . Also, one can see that mean anomaly  $M$  varies linearly with time.

For a given  $t$ , one can (i) determine  $M$  from  $M = n(t - t_0)$ , and (ii) find  $E$  by solving equation (B.39), (iii) get  $r$  from equation (B.36). When specifying the three dimensional planetary position in terms of the orbital elements, however, it is convenient to write down the planetary position in terms of true anomaly  $f$ , rather than eccentric anomaly  $E$ . From geometrical exercises, it can be shown that  $E$  and  $f$  are related;

$$\tan \frac{f}{2} = \sqrt{\frac{1+e}{1-e}} \tan \frac{E}{2}. \quad (\text{B.40})$$

Finally, this equation completes the path to relate the given time  $t$  and planetary position  $r$ , represented in terms of  $f$  (equation B.20).

## Appendix B.3 Three dimensional representation of the planetary orbit

Three dimensional planetary position vector is written down as

$$\begin{pmatrix} x \\ y \\ z \end{pmatrix} = \begin{pmatrix} r \cos f \\ r \sin f \\ 0 \end{pmatrix} \quad (\text{B.41})$$

in the coordinates centered on the star where  $x$ -axis points the direction of the periape of the planetary elliptic orbit,  $y$ -axis is perpendicular to the  $x$ -axis and lies within the planetary orbital plane, and  $z$ -axis points the direction normal to the orbital plane giving a right-handle triad with both  $x$  and  $y$ -axes. By definition, planet orbits within the  $x$ - $y$  plane.

We next convert this expressions into those in the reference frame where  $Z$ -axis points the observer and  $X$ -axis lies along with reference direction, making remaining  $Y$ -axis form a right-handed triad with both  $X$  and  $Z$ -axes. The plane which contains  $X$  and  $Y$ -axes is the reference plane.

Let  $i$  denote the orbital inclination, the angle between the orbital plane and the reference plane. The ascending node is defined as the point where the planet crosses the reference plane from negative- $Z$  region to positive- $Z$  region. The longitude of the ascending node,  $\Omega$ , is to depict the argument of the ascending node measured from  $X$ -axis. The angle between the radius vector to the longitude of the ascending node and the radius vector to the periape is called argument of periape with the character  $\omega$ . Note that the inclination  $i$  is defined for  $0^\circ < i < 180^\circ$ , and the orbit is called prograde when  $0^\circ < i < 90^\circ$ , while retrograde when  $90^\circ < i < 180^\circ$ .

$(x, y, z)$  system and  $(X, Y, Z)$  system are related with each other through three-times rotational manipulations.

1. rotation about the  $z$ -axis by the angle  $\omega$  so that  $x$ -axis coincides with the radial vector to the longitude of the ascending node.
2. rotation about the  $x$ -axis by the angle  $i$  so that the reference and orbital plane are aligned.
3. rotation about the  $z$ -axis by the angle  $\Omega$  so that the radial vector to the periape coincides with  $X$ -axis.

Rotation matrices about  $x$ ,  $y$  and  $z$ -axes are specified as

$$P_x(\phi) = \begin{pmatrix} \cos \phi & -\sin \phi & 0 \\ \sin \phi & \cos \phi & 0 \\ 0 & 0 & 1 \end{pmatrix}, \quad (\text{B.42})$$

$$P_y(\phi) = \begin{pmatrix} \cos \phi & 0 & \sin \phi \\ 0 & 1 & 0 \\ -\sin \phi & 0 & \cos \phi \end{pmatrix}, \quad (\text{B.43})$$

and

$$P_z(\phi) = \begin{pmatrix} 1 & 0 & 0 \\ 0 & \cos \phi & -\sin \phi \\ 0 & \sin \phi & \cos \phi \end{pmatrix}. \quad (\text{B.44})$$

Consequently,

$$\begin{pmatrix} X \\ Y \\ Z \end{pmatrix} = P_z(\Omega)P_x(i)P_z(\omega) \begin{pmatrix} x \\ y \\ z \end{pmatrix}, \quad (\text{B.45})$$

which gives by equation (B.41)

$$\begin{aligned} X &= r(\cos \Omega \cos(\omega + f) - \sin \Omega \sin(\omega + f) \cos i) \\ Y &= r(\sin \Omega \cos(\omega + f) + \cos \Omega \sin(\omega + f) \cos i) \\ Z &= r \sin(\omega + f) \sin i. \end{aligned} \quad (\text{B.46})$$

These are the analytical expressions for the three dimensional planetary position in the reference frame in terms of true anomaly  $f$ .



# Appendix C

## Transits

### Appendix C.1 General theory

#### Appendix C.1.1 Geometry of the transits

When seen nearly from edge-on, the star and planet in an exoplanetary system periodically eclipse each other. In general the star and planet have quite unequal sizes, and the eclipse of the smaller body in front of the larger body is called *transit* and the eclipse of the smaller body behind the larger body is *occultation* (Figure C.1). We hereafter focus on

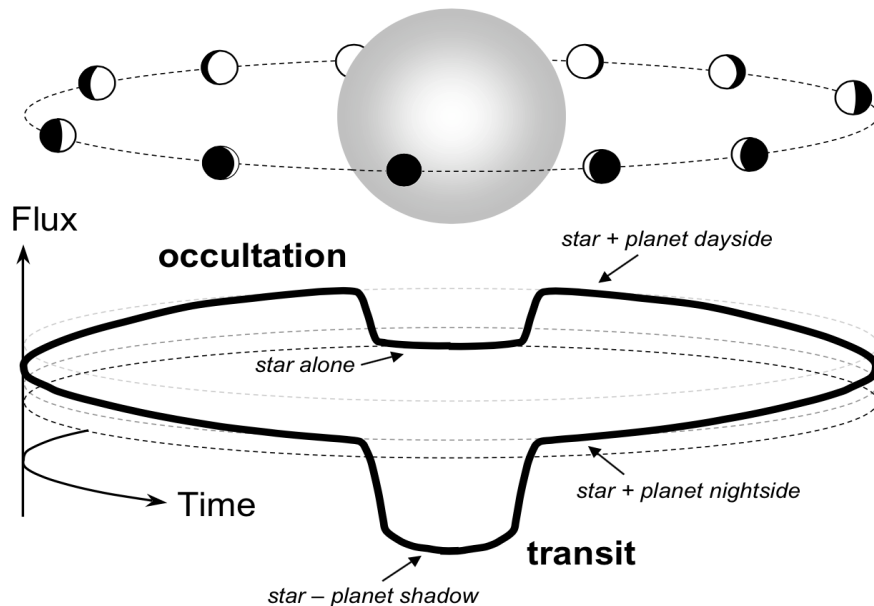


Figure C.1: Schematic illustration of the transits and occultations. We observe not the stellar and planetary flux separately, but only combined one. During a transit, the flux decreases because the planet masks a fraction of the stellar disk. Figure taken from Winn (2010).

the transits alone (see Winn 2010 for occultations).

For the geometric description, we adopt the  $(X, Y, Z)$  coordinates in Appendix B with  $X$ - $Y$  plane coincidental with the sky plane and positive  $Z$ -direction pointing at the observer (Figure 3.2). The transit occurs when the sky-projected planetary position,  $r_{\text{sky}} = \sqrt{X^2 + Y^2}$ , is smaller than the stellar radius  $R_\star$ . This relation is specified with the aid of equations (B.20) and (B.46);

$$r_{\text{sky}} = \frac{a(1 - e^2)}{1 + e \cos f} \sqrt{1 - \sin^2(\omega + f) \sin^2 i} < R_\star, \quad (\text{C.1})$$

where  $a, e, \omega, i$  and  $f$  are the semi-major axis of the planetary orbit, orbital eccentricity, the argument of periapse, orbital inclination and true anomaly, respectively. In general cases, the epochs when  $r_{\text{sky}}$  is minimized are around the inferior conjunction when  $\omega + f = +\pi/2$  unless the central star is highly oblate, the planetary orbit is extremely eccentric or close-in orbits are with grazing eclipses. Then the condition (C.1) is reduced in terms of the impact parameter  $b$ , the sky-projected distance at the inferior conjunction in units of the stellar radius;

$$b = \frac{a \cos i}{R_\star} \left( \frac{1 - e^2}{1 + e \sin \omega} \right) < 1. \quad (\text{C.2})$$

For the common case  $R_\star \ll a$ , the planet's path across the stellar disk is approximately a straight line between the points  $X = \pm R_\star \sqrt{1 - b^2}$  at  $Y = bR_\star$  ( $X$ -axis is chosen to be parallel to the transit path here;  $\Omega = 180^\circ$ ). Note that  $R_\star \ll a$  does not hold in PTF0 8-8695 system where the orbiting exoplanet is so close to the central star that  $a \sim 1.7R_\star$ .

### Appendix C.1.2 Phases of the transits

In a non-grazing eclipse, the stellar and planetary disks are tangent at four contact epochs  $t_1, t_2, t_3$  and  $t_4$  as illustrated in Figure C.2 (In a grazing eclipse, second and third contact do not occur). The epochs  $t_1$  and  $t_4$  can be calculated with  $r_{\text{sky}} = R_\star + R_p$ , while  $t_2$  and  $t_3$  are with  $r_{\text{sky}} = R_\star - R_p$ . The planetary orbital phase is classified into three stages with the help of  $t_1$ - $t_4$ ;

1. out-of-transit ( $t < t_1$  or  $t_4 < t$ ). The planetary disk never overlaps with the stellar disk.
2. ingress ( $t_1 < t < t_2$ ) and egress ( $t_3 < t < t_4$ ). Some (not all) portion of the planetary disk overlaps with the stellar disk.
3. full-transit ( $t_2 < t < t_3$ ). The planetary disk completely overlaps with the stellar disk.

The durations of ingress and egress are almost the same unless the stellar oblateness is very large or the planetary orbit is highly eccentric where the projected speed of the planet varies between ingress and egress.

The ordinary shape of transit light curve is given in Figure C.3.

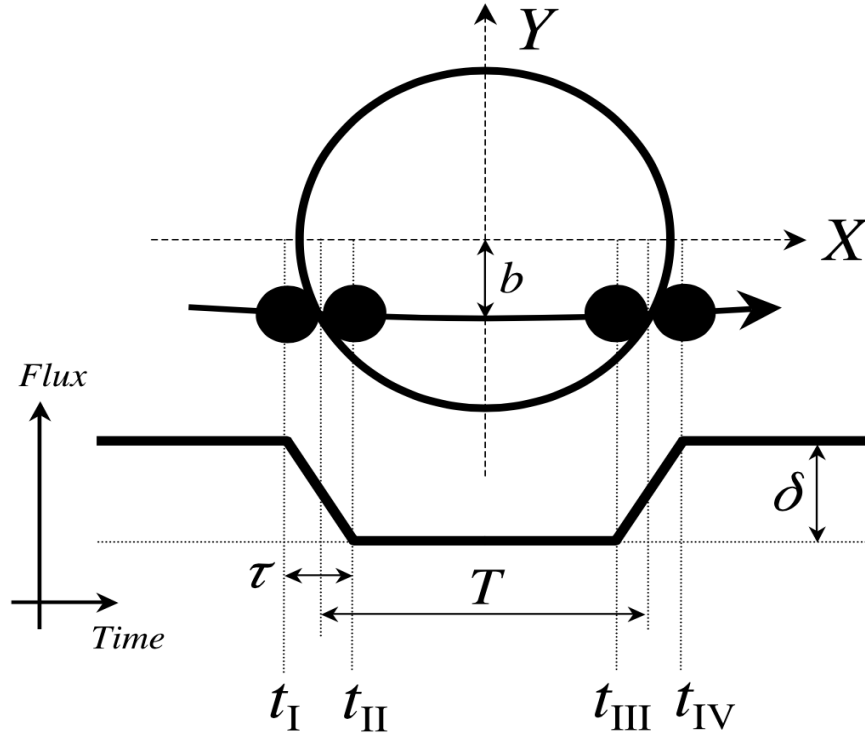


Figure C.2: Schematic illustration of the out-of-transit, ingress/egress and full-transit phases in the  $X$ - $Y$  plane (sky plane). The  $X$  and  $Y$  axes are chosen so that the descending node of the planet's orbit is placed along the positive- $X$  axis (i.e.,  $\Omega = 180^\circ$ ).  $t_1$ - $t_4$  are the four contact epochs between the stellar and planetary disks.  $\tau$  and  $T$  are the durations of ingress/egress and full-transit phases, respectively.  $b$  is the impact parameter of transit, and  $\delta$  denotes the extent of flux reduction during the full-transit phase. Figure taken from Winn (2010).

## Appendix C.2 Supplements to the light curve modelling

### Appendix C.2.1 Integration scheme of $F_{\text{blocked}}(t)$

#### full transit or ingress/egress

When integrating equation (4.10), we need to judge the system is under (i) out-of-transit, (ii) ingress/egress or (iii) full transit. The position of the planetary disk center in the sky plane,  $(x'_p, y'_p)$ , is calculated from Keplerian motion (see equation B.46 in Appendix B) as

$$x'_p = r(\cos \Omega \cos(\omega + f) - \sin \Omega \sin(\omega + f) \cos i) \quad (\text{C.3})$$

$$y'_p = \frac{r}{1 - f_{\text{eff}}} (\sin \Omega \cos(\omega + f) + \cos \Omega \sin(\omega + f) \cos i). \quad (\text{C.4})$$

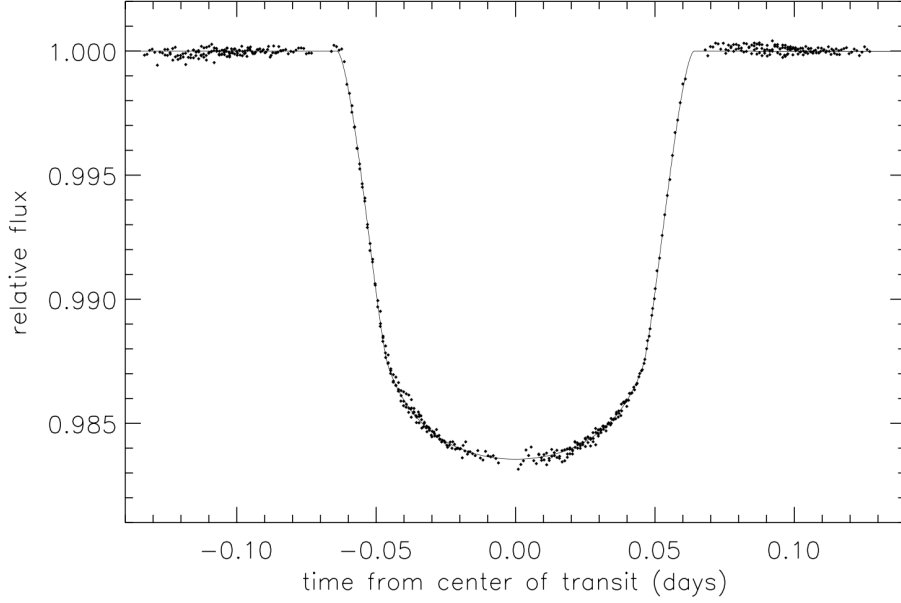


Figure C.3: Phase-folded transit light curve of HD 209458. Figure taken from Brown et al. (2001).

Then, the distance from the origin to the point on the edge of planetary disk,  $d_p$ , is parametrized as

$$d_p^2(\theta) = \left[ x'_p + R_p \cos\left(\frac{\pi}{2} + \theta'_p + \theta\right) \right]^2 + \left[ y'_p + \frac{R_p}{1 - f_{\text{eff}}} \sin\left(\frac{\pi}{2} + \theta'_p + \theta\right) \right]^2, \quad (\text{C.5})$$

where  $R_p$  is the planetary radius,  $\theta'_p = \tan^{-1}(y'_p/x'_p)$  and  $0 < \theta < 2\pi$ . The values of  $\theta$  that minimizes/maximizes  $d_p$ ,  $\theta_{p,\text{min}}/\theta_{p,\text{max}}$ , correspond to the roots of

$$\begin{aligned} f_p(\theta) &\equiv \frac{dd_p^2}{d\theta} \\ &= 2y'_p \frac{R_p}{1 - f_{\text{eff}}} \cos\left(\frac{\pi}{2} + \theta'_p + \theta\right) - 2x'_p R_p \sin\left(\frac{\pi}{2} + \theta'_p + \theta\right) \\ &\quad + 2 \left[ \left( \frac{R_p}{1 - f_{\text{eff}}} \right)^2 - R_p^2 \right] \sin\left(\frac{\pi}{2} + \theta'_p + \theta\right) \cos\left(\frac{\pi}{2} + \theta'_p + \theta\right) \end{aligned} \quad (\text{C.6})$$

in  $0 < \theta_{p,\text{min}} < \pi$  and  $\pi < \theta_{p,\text{max}} < 2\pi$ , respectively. Then we define the (i) out-of-transit, (ii) ingress/egress and (iii) full transit as

1.  $r_{\text{min}} \equiv d_p(\theta_{p,\text{min}}) \geq R_{\star,\text{eq}}$
2.  $r_{\text{min}} \equiv d_p(\theta_{p,\text{min}}) < R_{\star,\text{eq}}$  and  $r_{\text{max}} \equiv d_p(\theta_{p,\text{max}}) > R_{\star,\text{eq}}$
3.  $r_{\text{max}} \equiv d_p(\theta_{p,\text{max}}) \leq R_{\star,\text{eq}}$

In case 1, obviously  $F_{\text{blocked}}(t) = 0$ . We discuss cases 2 and 3 separately below.



Second,  $\theta_{p,\text{lower}}(r')$  and  $\theta_{p,\text{upper}}(r')$  are translated to the angles  $\theta_{\text{min}}(r')$  and  $\theta_{\text{max}}(r')$  in the polar coordinates centered on the origin through the relation

$$\begin{pmatrix} r' \cos \theta_{\text{min/max}}(r') \\ r' \sin \theta_{\text{min/max}}(r') \end{pmatrix} = \begin{pmatrix} x'_p \\ y'_p \end{pmatrix} + \begin{pmatrix} R_p \cos \left( \frac{\pi}{2} + \theta'_p + \theta_{p,\text{lower/upper}}(r') \right) \\ \frac{R_p}{1-f_{\text{eff}}} \sin \left( \frac{\pi}{2} + \theta'_p + \theta_{p,\text{lower/upper}}(r') \right) \end{pmatrix}. \quad (\text{C.9})$$

### integration during the full transit

During the full transit,  $F_{\text{blocked}}(t)$  is calculated in the polar coordinates  $(\tilde{r}, \tilde{\theta})$  centered on  $(x'_p, y'_p)$ ;

$$F_{\text{blocked}}(t) = (1 - f_{\text{eff}}) \int_0^{2\pi} d\tilde{\theta} \int_0^{\tilde{R}(\tilde{\theta})} \tilde{r} d\tilde{r} I_{\lambda,p}(\tilde{r}, \tilde{\theta}), \quad (\text{C.10})$$

where  $I_{\lambda,p}$  is defined as

$$I_{\lambda,p}(\tilde{r}, \tilde{\theta}) \equiv I_{\lambda} \left( \sqrt{(x'_p + \tilde{r} \cos \tilde{\theta})^2 + (y'_p + \tilde{r} \sin \tilde{\theta})^2}, \tan^{-1} \left[ (y'_p + \tilde{r} \sin \tilde{\theta}) / (x'_p + \tilde{r} \cos \tilde{\theta}) \right] \right). \quad (\text{C.11})$$

The integration with respect to  $\tilde{r}$  is ahead, followed by  $\tilde{\theta}$  integration. The upper limit of the radial integration,  $\tilde{R}(\tilde{\theta})$ , is dependent on  $\tilde{\theta}$  since the planetary disk takes elongated shape to the  $y$ -direction through the transformation making elliptic stellar disk into circle form ( $y' = y/(1 - f_{\text{eff}})$ ), and given by the condition

$$\left( \frac{\tilde{R}(\tilde{\theta}) \cos \tilde{\theta}}{R_p} \right)^2 + (1 - f_{\text{eff}})^2 \left( \frac{\tilde{R}(\tilde{\theta}) \sin \tilde{\theta}}{R_p} \right)^2 = 1 \quad (\text{C.12})$$

as

$$\tilde{R}(\tilde{\theta}) = \frac{R_p}{\sqrt{\cos^2 \tilde{\theta} + (1 - f_{\text{eff}})^2 \sin^2 \tilde{\theta}}}. \quad (\text{C.13})$$

### Appendix C.2.2 Consistency relation for $T_{\text{pol}}$

The temperature parameter necessary for our light curve model is the polar surface temperature  $T_{\text{pol}}$ , while the parameter that observations provide is the stellar effective temperature  $T_{\text{eff}}$ . They are not identical, but related as (Philippov & Rafikov 2013)

$$T_{\text{pol}} = T_{\text{eff}} \times \left[ \frac{1}{\pi R_{\star,\text{eq}}^2 (1 - f_{\text{eff}})} \int_{\text{stellar disk}} L(r', \theta') \left( \frac{g(r', \theta')}{g_{\text{pole}}} \right)^{4\beta_{\text{GD}}} r' dr' d\theta' \right]^{-1/4}. \quad (\text{C.14})$$

In this thesis, however,  $T_{\text{pol}}$  and is assumed to be the same as  $T_{\text{eff}}$  since the difference would generally be negligible.

### Appendix C.2.3 Absolute dimension of the system

In the formulation in chapters 3 and 4, the resulting transit light curve is invariant under the transformation of  $M_\star$  and  $R_{\star,\text{eq}}$  that keeps  $\rho_\star \equiv M_\star / \frac{4}{3}\pi R_{\star,\text{eq}}^3$  the same. Therefore, any  $M_\star$  and  $R_{\star,\text{eq}}$  scaled in such a way are approved as the solutions that satisfy the observed transit light curves, which make it impossible to obtain the absolute set of  $M_\star$  and  $R_{\star,\text{eq}}$  (i.e., one cannot get  $M_\star$  and  $R_{\star,\text{eq}}$  separately). One way to solve this problem is to make use of the information on spectroscopic  $v \sin i_\star$ , because

$$\begin{aligned} v \sin i_\star &= \frac{2\pi R_{\star,\text{eq}}}{P_{\text{rot}}} \sin i_\star = \frac{2\pi}{R_{\text{rot}}} \left( \frac{3M_\star}{4\pi\rho_\star} \right)^{1/3} \sin i_\star \\ &= 4.90187 \text{ kms}^{-1} \left( \frac{1/P_{\text{rot}}}{\mu\text{Hz}} \right) \left( \frac{M_\star}{M_\odot} \right)^{1/3} \left( \frac{\rho_\star}{\text{gcm}^{-3}} \right)^{-1/3} \sin i_\star \end{aligned} \quad (\text{C.15})$$

explicitly includes either  $M_\star$  or  $R_{\star,\text{eq}}$  (for example, Barnes et al. 2011).



# Appendix D

## General Formulation of Equations of Motion

### Appendix D.1 Gravitational potential energy

#### Appendix D.1.1 Centrifugal forces

In this chapter, the index 0 with mass  $M$  or radius  $R$  is to denote the central star while 1 for the planet. Stellar or planetary spin causes them to be deformed due to the effect of centrifugal force. Let  $x_3$ -axis be along with the spin vector (with spin rate  $\omega$ , unit vector  $\hat{\mathbf{S}}$ ) of the rotating body,  $x_1$ - and  $x_2$ -axes be mutually orthogonal directions placed within the plane perpendicular to the  $x_3$ -axis. In addition, let  $r$ ,  $\theta$  and  $\phi$  be the radial extent, colatitude and longitude measured in the spherical coordinates centered on the body, respectively. The centrifugal force per unit mass is given as (Goldstein et al. 2002)

$$\mathbf{F}_{\text{cf}} = \omega^2(x_1\hat{\mathbf{x}}_1, x_2\hat{\mathbf{x}}_2, 0), \quad (\text{D.1})$$

and centrifugal potential  $V_{\text{cf}}$  which satisfies  $\mathbf{F}_{\text{cf}} = -\nabla V_{\text{cf}}$  is given by

$$V_{\text{cf}}(r, \theta) = -\frac{1}{2}\omega^2 r^2 \sin^2 \theta. \quad (\text{D.2})$$

This potential is found to be independent of the longitude, which means that the rotational effect breaks the spherical symmetry of the system but retains axisymmetry ( $a = b > c$  where  $a$ ,  $b$  and  $c$  are the radii of the object along with  $x_1$ -,  $x_2$ - and  $x_3$ -axis, respectively).

#### Appendix D.1.2 Gravitational potential outside of the rotating body

First we set  $\mathbf{r} = (r \sin \theta \cos \phi, r \sin \theta \sin \phi, r \cos \theta)$  as a position vector of the point outside the star and  $\mathbf{r}' = (r' \sin \theta' \cos \phi', r' \sin \theta' \sin \phi', r' \cos \theta')$  as a position vector of the mass element within the star ( $r > r'$ ), with  $(\theta, \phi)$  showing the polar and azimuthal angles of  $\mathbf{r}$

and  $(\theta', \phi')$  for  $\mathbf{r}'$ . Based on this expression, the integral over the whole figure of the star with respect to  $\mathbf{r}'$  provides the gravitational potential  $V$  at  $\mathbf{r}$ :

$$V = -G \int_{\text{star}} \frac{1}{|\mathbf{r} - \mathbf{r}'|} dM_0, \quad (\text{D.3})$$

where  $G$  is gravitational constant,  $dM_0 = \rho_0 r'^2 \sin \theta' dr' d\theta' d\phi'$  is the mass element placed at  $\mathbf{r}'$  with mass density distribution of the star  $\rho_0$ .

The integrand can be expanded as

$$\begin{aligned} \frac{1}{|\mathbf{r} - \mathbf{r}'|} &= r^{-1} \left[ 1 - 2 \frac{r'}{r} (\hat{\mathbf{r}} \cdot \hat{\mathbf{r}}') + \left( \frac{r'}{r} \right)^2 \right]^{-\frac{1}{2}} \\ &= \frac{1}{r} \sum_{n=0}^{\infty} \left( \frac{r'}{r} \right)^n P_n(\hat{\mathbf{r}} \cdot \hat{\mathbf{r}}'), \end{aligned} \quad (\text{D.4})$$

where  $P_n(\hat{\mathbf{r}} \cdot \hat{\mathbf{r}}')$  is a Legendre polynomial of degree  $n$ . In the spherical coordinates, the argument  $(\hat{\mathbf{r}} \cdot \hat{\mathbf{r}}')$  is rewritten in terms of colatitudes and longitudes of  $\mathbf{r}$  and  $\mathbf{r}'$  as

$$\hat{\mathbf{r}} \cdot \hat{\mathbf{r}}' = \cos \theta \cos \theta' + \sin \theta \sin \theta' \cos(\phi - \phi'). \quad (\text{D.5})$$

The following theorem for the Legendre polynomials is helpful to write down  $P_n(\hat{\mathbf{r}} \cdot \hat{\mathbf{r}}')$  in terms of colatitudes and longitudes as

$$\begin{aligned} P_n(\hat{\mathbf{r}} \cdot \hat{\mathbf{r}}') &= \sum_{m=0}^n (2 - \delta_{m0}) \frac{(n-m)!}{(n+m)!} P_{nm}(\cos \theta) P_{nm}(\cos \theta') \cos(m(\phi - \phi')) \\ &= P_n(\cos \theta) P_n(\cos \theta') + 2 \sum_{m=1}^n \frac{(n-m)!}{(n+m)!} P_{nm}(\cos \theta) P_{nm}(\cos \theta') \cos(m(\phi - \phi')), \end{aligned} \quad (\text{D.6})$$

where  $P_{nm}$  is the associated Legendre polynomial of degree  $n$ , order  $m$  (note:  $m \leq n$ ,  $P_{n0}(x) = P_n(x)$ ) and  $\delta_{m0}$  is Kronecker's delta. The explicit forms of  $P_{nm}$  up to the 4th degree are presented in Table D.1. Note that  $\rho_0 = \rho_0(r', \theta')$  does not depend on  $\phi'$  and is symmetric for northern and southern hemispheres of the rotating star.

With *Stokes coefficients*  $C_{nm}, S_{nm}$  defined as

$$\left\{ \begin{array}{l} C_{nm} \\ S_{nm} \end{array} \right\} = \frac{1}{M_0 R_0^n} (2 - \delta_{m0}) \frac{(n-m)!}{(n+m)!} \int_{\text{star}} (r')^n P_{nm}(\cos \theta') \left\{ \begin{array}{l} \cos(m\phi') \\ \sin(m\phi') \end{array} \right\} dM_0, \quad (\text{D.7})$$

the gravitational potential  $V$  can be expressed briefly as

$$V = -\frac{GM_0}{r} \sum_{n=0}^{\infty} \sum_{m=0}^n \left( \frac{R_0}{r} \right)^n (C_{nm} \cos(m\phi) + S_{nm} \sin(m\phi)) P_{nm}(\cos \theta) \quad (\text{D.8})$$

with stellar mass  $M_0$  and stellar equatorial radius  $R_0$ . Baring in mind that  $S_{n0} = 0$ , we here derive the explicit form of Stokes coefficients up to 4th degree. In the following procedure, we use

$$\begin{pmatrix} x'_1 \\ x'_2 \\ x'_3 \end{pmatrix} = \begin{pmatrix} r' \sin \theta' \cos \phi' \\ r' \sin \theta' \sin \phi' \\ r' \cos \theta' \end{pmatrix}, \quad (\text{D.9})$$

and the symmetry of  $\rho_0$  with respect to the  $\theta = \pi/2$  plane (stellar equator). Namely,  $\rho_0$  is an even function with respect to  $\cos \theta'$ .

- $n = 0$

$$C_{00} = \frac{1}{M_0} \int_{\text{star}} dM_0 = 1 \quad (\text{D.10})$$

- $n = 1$

$$C_{10} = \frac{1}{M_0 R_0} \int_{\text{star}} r' \cos \theta' dM_0 = \frac{1}{M_0 R_0} \int_{\text{star}} x'_3 dM_0 = 0 \quad (\text{D.11})$$

$$C_{11} = \frac{1}{M_0 R_0} \int_{\text{star}} r' \sin \theta' \cos \phi' dM_0 = \frac{1}{M_0 R_0} \int_{\text{star}} x'_1 dM_0 = 0 \quad (\text{D.12})$$

$$S_{11} = \frac{1}{M_0 R_0} \int_{\text{star}} r' \sin \theta' \sin \phi' dM_0 = \frac{1}{M_0 R_0} \int_{\text{star}} x'_2 dM_0 = 0 \quad (\text{D.13})$$

- $n = 2$

$$\begin{aligned} C_{20} &= \frac{1}{M_0 R_0^2} \int_{\text{star}} r'^2 \left( \frac{3}{2} \cos^2 \theta' - \frac{1}{2} \right) dM_0 \\ &= -\frac{1}{M_0 R_0^2} \left( I_{33} - \frac{1}{2}(I_{11} + I_{22}) \right) = -\frac{1}{M_0 R_0^2} (C_0 - A_0) \end{aligned} \quad (\text{D.14})$$

$$C_{21} = \frac{1}{M_0 R_0^2} \int_{\text{star}} r'^2 \sin \theta' \cos \theta' \cos \phi' dM_0 = \frac{I_{31}}{M_0 R_0^2} = 0 \quad (\text{D.15})$$

$$S_{21} = \frac{1}{M_0 R_0^2} \int_{\text{star}} r'^2 \sin \theta' \cos \theta' \sin \phi' dM_0 = \frac{I_{23}}{M_0 R_0^2} = 0 \quad (\text{D.16})$$

$$C_{22} = \frac{1}{4M_0 R_0^2} \int_{\text{star}} r'^2 \sin^2 \theta' \cos 2\phi' dM_0 = \frac{I_{22} - I_{11}}{4M_0 R_0^2} = 0 \quad (\text{D.17})$$

$$S_{22} = \frac{1}{4M_0 R_0^2} \int_{\text{star}} r'^2 \sin^2 \theta' \sin 2\phi' dM_0 = \frac{I_{12}}{2M_0 R_0^2} = 0, \quad (\text{D.18})$$

where the moment of inertia tensor  $I_{ij}$  ( $i, j = 1, 2, 3$ ) of the rotating star are defined as

$$I_{ii} = \int_{\text{star}} (x_j^2 + x_k^2) dM_0 \quad \text{for } i \neq j \neq k \quad (\text{D.19})$$

$$I_{ij} = - \int_{\text{star}} x_i x_j dM_0 \quad \text{for } i \neq j, \quad (\text{D.20})$$

and from axisymmetry

$$I_{11} = I_{22}(\equiv A_0) \neq I_{33}(\equiv C_0) \quad (\text{D.21})$$

$$I_{ij}(i \neq j) = 0. \quad (\text{D.22})$$

•  $n = 3$

$$C_{30} = \frac{1}{M_0 R_0^3} \int_{\text{star}} r'^3 \left( \frac{5}{2} \cos^3 \theta' - \frac{3}{2} \cos \theta' \right) dM_0 = 0 \quad (\text{D.23})$$

$$C_{31} = \frac{1}{M_0 R_0^3} \int_{\text{star}} r'^3 \sin \theta' \left( \frac{5}{4} \cos^2 \theta' - \frac{1}{4} \right) \cos \phi' dM_0 = 0 \quad (\text{D.24})$$

$$S_{31} = -\frac{1}{M_0 R_0^3} \int_{\text{star}} r'^3 \sin \theta' \left( \frac{5}{4} \cos^2 \theta' - \frac{1}{4} \right) \sin \phi' dM_0 = 0 \quad (\text{D.25})$$

$$C_{32} = \frac{1}{M_0 R_0^3} \int_{\text{star}} r'^3 \frac{1}{4} \cos \theta' \sin^2 \theta' \cos 2\phi' dM_0 = 0 \quad (\text{D.26})$$

$$S_{32} = \frac{1}{M_0 R_0^3} \int_{\text{star}} r'^3 \frac{1}{4} \cos \theta' \sin^2 \theta' \sin 2\phi' dM_0 = 0 \quad (\text{D.27})$$

$$C_{33} = -\frac{1}{M_0 R_0^3} \int_{\text{star}} r'^3 \frac{1}{24} \sin^3 \theta' \cos 3\phi' dM_0 = 0 \quad (\text{D.28})$$

$$S_{33} = -\frac{1}{M_0 R_0^3} \int_{\text{star}} r'^3 \frac{1}{24} \sin^3 \theta' \sin 3\phi' dM_0 = 0 \quad (\text{D.29})$$

•  $n = 4$

$$C_{40} = \frac{1}{M_0 R_0^4} \int_{\text{star}} r'^4 P_4(\cos \theta') dM_0 (\neq 0) \quad (\text{D.30})$$

$$C_{41} = \frac{1}{M_0 R_0^4} \int_{\text{star}} r'^4 \sin \theta' \left( \frac{7}{4} \cos^3 \theta' - \frac{3}{4} \right) \cos \phi' dM_0 = 0 \quad (\text{D.31})$$

$$S_{41} = -\frac{1}{M_0 R_0^4} \int_{\text{star}} r'^4 \sin \theta' \left( \frac{7}{4} \cos^3 \theta' - \frac{3}{4} \right) \sin \phi' dM_0 = 0 \quad (\text{D.32})$$

$$C_{42} = \frac{1}{M_0 R_0^4} \int_{\text{star}} r'^4 \sin^2 \theta' \left( \frac{7}{24} \cos^2 \theta' - \frac{1}{24} \right) \cos 2\phi' dM_0 = 0 \quad (\text{D.33})$$

$$S_{42} = \frac{1}{M_0 R_0^4} \int_{\text{star}} r'^4 \sin^2 \theta' \left( \frac{7}{24} \cos^2 \theta' - \frac{1}{24} \right) \sin 2\phi' dM_0 = 0 \quad (\text{D.34})$$

$$C_{43} = -\frac{1}{M_0 R_0^4} \int_{\text{star}} r'^4 \cos \theta' \sin^3 \theta' \cos 3\phi' dM_0 = 0 \quad (\text{D.35})$$

$$S_{43} = -\frac{1}{M_0 R_0^4} \int_{\text{star}} r'^4 \cos \theta' \sin^3 \theta' \sin 3\phi' dM_0 = 0 \quad (\text{D.36})$$

$$C_{44} = \frac{1}{M_0 R_0^4} \int_{\text{star}} r'^4 \sin^4 \theta' \cos 4\phi' dM_0 = 0 \quad (\text{D.37})$$

$$S_{44} = \frac{1}{M_0 R_0^4} \int_{\text{star}} r'^4 \sin^4 \theta' \sin 4\phi' dM_0 = 0 \quad (\text{D.38})$$

The *gravitational coefficients* of degree  $n$ ,  $J_{n,0}$  (the latter index is to denote the star or planet), is defined as (Zharkov & Trubitsyn (1974), Armitage (2010))

$$J_{n,0} = -\frac{1}{M_0 R_0^2} \int_{\text{star}} (r')^n P_n(\cos \theta) dM_0, \quad (\text{D.39})$$

and it is not difficult to check  $J_{2,0} = -C_{20}$ ,  $J_{4,0} = -C_{40}$ .

Finally, recalling  $\cos \theta = \hat{\mathbf{r}} \cdot \hat{\mathbf{x}}_3 = \hat{\mathbf{r}} \cdot \hat{\mathbf{S}}_0$ , above results in terms of the Stokes coefficients yield the gravitational potential outside the rotating star to the 4th order of  $(R_0/r)$ :

$$V \simeq -\frac{GM_0}{r} \left[ 1 - J_{2,0} \left( \frac{R_0}{r} \right)^2 P_2(\hat{\mathbf{r}} \cdot \hat{\mathbf{S}}_0) - J_{4,0} \left( \frac{R_0}{r} \right)^4 P_4(\hat{\mathbf{r}} \cdot \hat{\mathbf{S}}_0) \right]. \quad (\text{D.40})$$

The gravitational potential actually used in our analysis does not contain the  $J_{4,0}$  term:

$$V \simeq -\frac{GM_0}{r} \left[ 1 - J_{2,0} \left( \frac{R_0}{r} \right)^2 P_2(\hat{\mathbf{r}} \cdot \hat{\mathbf{S}}_0) \right]. \quad (\text{D.41})$$

Note that symmetry of the rotating body causes the gravitational coefficients with odd degrees to vanish (i.e.,  $J_{2n+1,0} = 0$  ( $n = 0, 1, 2, \dots$ )).

### Appendix D.1.3 Gravitational potential energy in the oblate star-planet system

Let  $\mathbf{r}_0$  be the relative position vector pointing from the center of the star to the center of the planet, and  $\mathbf{r}''$  be the displacement vector of the planetary mass element  $dM_1$  from the center of the planet. Thereby the position of planetary mass element,  $\mathbf{r}$ , is given by  $\mathbf{r} = \mathbf{r}_0 + \mathbf{r}''$  ( $r_0 > r''$ ). Then integral of  $V$  multiplied by  $dM_1$  over the whole volume of the planet ( $\mathbf{r}''$  is supposed to sweep the whole planet) provides the gravitational potential energy  $U$  of the system consisting of the rotating star and rotating planet:

$$U = \int_{\text{planet}} V dM_1 = - \int_{\text{planet}} \frac{GM_0}{r} \left[ 1 - J_{2,0} \left( \frac{R_0}{r} \right)^2 P_2(\hat{\mathbf{r}} \cdot \hat{\mathbf{S}}_0) - J_{4,0} \left( \frac{R_0}{r} \right)^4 P_4(\hat{\mathbf{r}} \cdot \hat{\mathbf{S}}_0) \right] dM_1. \quad (\text{D.42})$$

Figure D.1 is helpful to understand the relation of several vectors in the oblate star-planet system. The  $1/r$  term in equation (D.42) can be rewritten in terms of  $\mathbf{r}_0$ ,  $\mathbf{r}''$ :

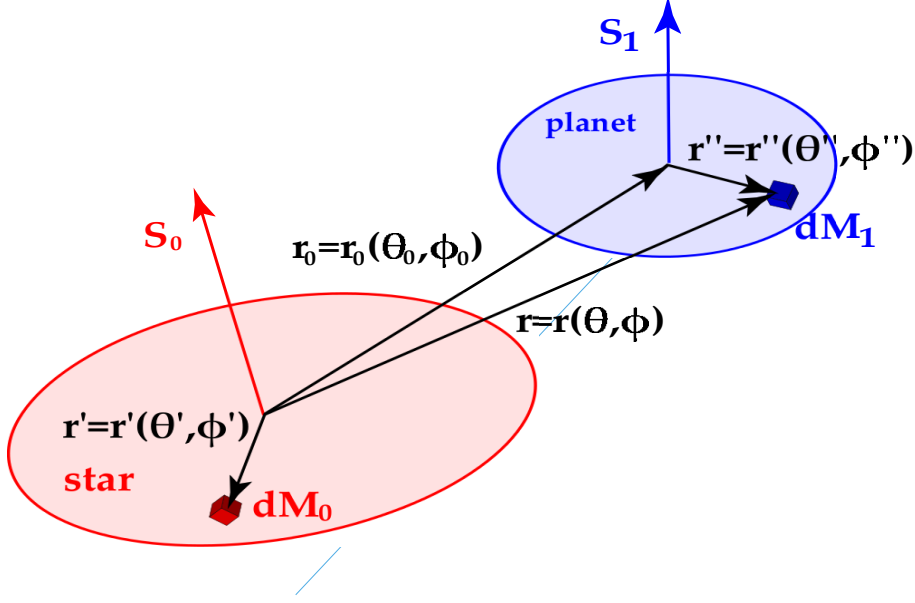


Figure D.1: Schematic illustration of the relation of vectors in the oblate star-planet system. The star is denoted as the red ellipse, while the planet is blue.

$$\begin{aligned}
\frac{1}{r} &= \frac{1}{r_0} \left[ 1 + 2 \frac{r''}{r_0} (\mathbf{r}_0 \cdot \mathbf{r}'') + \left( \frac{r''}{r_0} \right)^2 \right]^{-\frac{1}{2}} \\
&= \frac{1}{r_0} \left[ 1 - 2 \frac{r''}{r_0} (-\mathbf{r}_0 \cdot \mathbf{r}'') + \left( \frac{r''}{r_0} \right)^2 \right]^{-\frac{1}{2}} \\
&= \frac{1}{r_0} \sum_{n=0}^{\infty} \left( \frac{r''}{r_0} \right)^n P_n(-\mathbf{r}_0 \cdot \mathbf{r}'') = \frac{1}{r_0} \sum_{n=0}^{\infty} \left( \frac{r''}{r_0} \right)^n (-1)^n P_n(\mathbf{r}_0 \cdot \mathbf{r}'') \\
&= \frac{1}{r_0} \sum_{n=0}^{\infty} \sum_{m=0}^n \left( \frac{r''}{r_0} \right)^n (-1)^n (2 - \delta_{m0}) \frac{(n-m)!}{(n+m)!} P_{nm}(\cos \theta_0) P_{nm}(\cos \theta'') \cos(m(\phi_0 - \phi''))
\end{aligned} \tag{D.43}$$

where  $(\theta_0, \phi_0)$ ,  $(\theta'', \phi'')$  are the polar and azimuthal angles of  $\mathbf{r}_0$ ,  $\mathbf{r}''$ , respectively, in the spherical coordinate centered on the planet where its spin vector  $\hat{\mathbf{S}}_1$  is along with  $z$ -axis ( $\cos \theta_0 = \hat{\mathbf{r}}_0 \cdot \hat{\mathbf{S}}_1$ ,  $\cos \theta'' = \hat{\mathbf{r}}'' \cdot \hat{\mathbf{S}}_1$ ).

We focus on the gravitational potential energy  $U$  up to 5th order of  $1/r_0$ :

$$U \simeq \int_{\text{planet}} V \, dM_1 = -\frac{GM_0 M_1}{r_0} \left[ 1 - \sum_{n=1}^4 \left( \frac{1}{r_0} \right)^n A_n \right]. \tag{D.44}$$

With the help of the expansion formula for  $1/r$ ,  $A_n$  can be specified as follows.

- $n = 1$

$$A_1 = R_1 \sum_{m=0}^1 (C_{1m} \cos(m\phi_0) + S_{1m} \sin(m\phi_0)) P_{1m}(\cos \theta_0) = 0, \quad (\text{D.45})$$

where  $C_{nm}, S_{nm}$  take the same forms as the stellar case but  $(M_0, R_0, r', \theta', \phi')$  should be replaced by the planetary ones  $(M_1, R_1, r'', \theta'', \phi'')$ .

- $n = 2$

$$\begin{aligned} A_2 &= J_{2,0} R_0^2 P_2(\hat{\mathbf{r}}_0 \cdot \hat{\mathbf{S}}_0) - R_1^2 \sum_{m=0}^2 (C_{2m} \cos(m\phi_0) + S_{2m} \sin(m\phi_0)) P_{2m}(\cos \theta_0) \\ &= \sum_{i=0,1} J_{2,i} R_i^2 P_2(\hat{\mathbf{r}}_0 \cdot \hat{\mathbf{S}}_i) \end{aligned} \quad (\text{D.46})$$

- $n = 3$

The specification of  $A_3, A_4$  requires the angular relation between  $\hat{\mathbf{S}}_0$  and  $\hat{\mathbf{r}}''$ .  $\hat{\mathbf{S}}_0$  is the constant vector in the spherical coordinates centered on the planet, then  $\int_{\text{planet}} (\hat{\mathbf{r}}'' \cdot \hat{\mathbf{S}}_0) dM_1 = 0$  since  $\rho_1$  is an even function with respect to  $\cos \theta''$ .

$$\begin{aligned} A_3 &= \frac{3J_{2,0}R_0^2}{M_1} (\hat{\mathbf{r}}_0 \cdot \hat{\mathbf{S}}_0) \int_{\text{planet}} r'' (\hat{\mathbf{r}}'' \cdot \hat{\mathbf{S}}_0) dM_1 \\ &\quad + R_1^3 \sum_{m=0}^3 (C_{3m} \cos(m\phi_0) + S_{3m} \sin(m\phi_0)) P_{3m}(\cos \theta_0) \\ &\quad - J_{2,0} R_0^2 R_1 \left( \frac{15}{2} (\hat{\mathbf{r}}_0 \cdot \hat{\mathbf{S}}_0)^2 - \frac{3}{2} \right) \sum_{m=0}^1 (C_{1m} \cos(m\phi_0) + S_{1m} \sin(m\phi_0)) P_{1m}(\cos \theta_0) \\ &= 0 + 0 + 0 = 0 \end{aligned} \quad (\text{D.47})$$

- $n = 4$

$$\begin{aligned}
A_4 &= J_{4,0} R_0^4 P_4(\hat{\mathbf{r}}_0 \cdot \hat{\mathbf{S}}_0) \\
&\quad - R_1^4 \sum_{m=0}^4 (C_{4m} \cos(m\phi_0) + S_{4m} \sin(m\phi_0)) P_{4m}(\cos \theta_0) \\
&\quad + \frac{5}{2} J_{2,0} R_0^2 R_1^2 \left( 7(\hat{\mathbf{r}}_0 \cdot \hat{\mathbf{S}}_0)^2 - 1 \right) \sum_{m=0}^2 (C_{2m} \cos(m\phi_0) + S_{2m} \sin(m\phi_0)) P_{2m}(\cos \theta_0) \\
&\quad - 15 \frac{J_{2,0} R_0^2}{M_1} (\hat{\mathbf{r}}_0 \cdot \hat{\mathbf{S}}_0) \int_{\text{planet}} r''^2 (\hat{\mathbf{r}}_0 \cdot \hat{\mathbf{r}}'') (\hat{\mathbf{r}}'' \cdot \hat{\mathbf{S}}_0) dM_1 \\
&\quad + \frac{3}{2} \frac{J_{2,0} R_0^2}{M_1} \int_{\text{planet}} r''^2 (\hat{\mathbf{r}}'' \cdot \hat{\mathbf{S}}_0)^2 dM_1 \\
&\quad - \frac{J_{2,0} R_0^2}{M_1} \left( 5(\hat{\mathbf{r}}_0 \cdot \hat{\mathbf{S}}_0)^2 - \frac{1}{2} \right) \left( \int_{\text{planet}} r''^2 dM_1 \right) \\
&= \sum_{i=0,1} J_{4,i} R_i^4 P_4(\hat{\mathbf{r}}_0 \cdot \hat{\mathbf{S}}_i) \\
&\quad - \frac{5}{2} \frac{J_{2,0} J_{2,1} R_0^2 R_1^2}{M_1} \left( 7(\hat{\mathbf{r}}_0 \cdot \hat{\mathbf{S}}_0)^2 - 1 \right) P_2(\hat{\mathbf{r}}_0 \cdot \hat{\mathbf{S}}_1) \\
&\quad + \frac{J_{2,0} R_0^2}{M_1} \int_{\text{planet}} r''^2 \left( 5(\hat{\mathbf{r}}_0 \cdot \hat{\mathbf{S}}_0)^2 - \frac{1}{2} - 15(\hat{\mathbf{r}}_0 \cdot \hat{\mathbf{S}}_0) (\hat{\mathbf{r}}_0 \cdot \hat{\mathbf{r}}'') (\hat{\mathbf{r}}'' \cdot \hat{\mathbf{S}}_0) + \frac{3}{2} (\hat{\mathbf{r}}'' \cdot \hat{\mathbf{S}}_0)^2 \right) dM_1
\end{aligned} \tag{D.48}$$

$A_2$  term is found to be the summation of most dominant terms out of the terms induced by stellar/planetary deformation (i.e., all terms except for a simple Newtonian potential  $GM_0M_1/r_0$ ). This term is derived by assuming that the counterpart object of deformation-calculating body is point-mass. In turn,  $A_4$  term results from the simultaneous consideration of both stellar/planetary deformation with finite (nonzero) volumes. Therefore,  $A_2$  term is the order of  $f$ , while  $A_4$  terms is the order of  $f^2$ .

## Appendix D.2 Hamiltonian and equations of motion for the spin-orbit nodal precession

### Appendix D.2.1 Equations of motion in the oblate star-planet system

With the help of the analytic expression for the gravitational potential energy in the oblate star-planet system, the Hamiltonian of the system is obtained:

$$H = \frac{\mathbf{p}^2}{2\beta} - \frac{GM_0M_1}{r} \left( 1 - \sum_{i=0,1} J_{2,i} \left( \frac{R_i}{r} \right)^2 P_2(\hat{\mathbf{r}} \cdot \hat{\mathbf{S}}_i) \right) + \sum_{i=0,1} \frac{\mathbf{S}_i^2}{2\tilde{C}_i M_i R_i^2}, \tag{D.49}$$

where the first term in right hand side is the kinetic energy of the orbiting planet relative to the central star with  $\beta$  denoting the reduced mass, the second term is gravitational potential energy and the third term corresponds to the stellar and planetary rotational energy, respectively. Hamilton's equations enables us to write down the equations of motion (EOM) in this system in terms of the differential equations for planetary position  $\mathbf{r}$ , planetary momentum  $\mathbf{p}$ , stellar spin angular momentum  $\mathbf{S}_0$  and planetary spin angular momentum  $\mathbf{S}_1$  (Boué & Laskar 2006, 2009):

$$\dot{\mathbf{r}} = \nabla_{\mathbf{p}} H = \frac{\mathbf{p}}{\beta} \quad (\text{D.50})$$

$$\begin{aligned} \dot{p}_i &= -(\nabla_{\mathbf{r}} H)_i \\ &= -\frac{\beta\mu}{(2r)^5} \left[ 2r^2 r_i + \sum_{j=0,1} 3R_j^2 J_{2,j}(\hat{\mathbf{S}}_j \cdot \hat{\mathbf{r}}) \left[ \left( 1 + 2(\hat{\mathbf{S}}_j \cdot \hat{\mathbf{r}}) \hat{S}_{j,i} \hat{r}_i - 5(\hat{\mathbf{s}}_j \cdot \hat{\mathbf{r}})^2 \right) r_i + \frac{1}{r} (r^2 - r_i^2) \hat{S}_{j,i} \right] \right] \end{aligned} \quad (\text{D.51})$$

$$\dot{\mathbf{S}}_i = 2\nabla_{\mathbf{S}_i} H \times \mathbf{S}_i = \frac{3GM_0 M_1 J_{2,i} R_i^2}{r^3} (\hat{\mathbf{r}} \cdot \hat{\mathbf{S}}_i) (\hat{\mathbf{r}} \times \hat{\mathbf{S}}_i). \quad (\text{D.52})$$

It is not difficult to check the angular momentum conservation law with above formulae and orbital angular momentum  $\mathbf{L} = \mathbf{r} \times \mathbf{p}$  as

$$\dot{\mathbf{S}}_0 + \dot{\mathbf{S}}_1 + \dot{\mathbf{L}} = \dot{\mathbf{S}}_0 + \dot{\mathbf{S}}_1 + \dot{\mathbf{r}} \times \mathbf{p} + \mathbf{r} \times \dot{\mathbf{p}} = 0. \quad (\text{D.53})$$

In order to pursue the dynamical evolution of the system with time, numerical integration of these equations is most robust and straightforward way.

### Appendix D.2.2 Laplace-Runge-Lenz vector

Laplace-Runge-Lenz vector (hereafter, Lenz vector) is the vector pointing towards the periaapse from the central star with the magnitude identical to the value of orbital eccentricity  $e$ :

$$\mathbf{e} = \frac{\dot{\mathbf{r}} \times \mathbf{L}}{\beta\mu} - \frac{\mathbf{r}}{r}, \quad (\text{D.54})$$

with  $\mu = G(M_0 + M_1)$ .

### Appendix D.2.3 Equations of motion after orbital averaging

In the case where the dynamical evolution of the system of interest occurs with much longer time scale than the planetary orbital period, it is convenient to take orbital average of EOM to pursue the secular evolution of the system. This procedure reduces the computational cost, thereby one can calculate the evolution of the system for longer time.

For instance, the precession period in the PTFO 8-8695 system ( $\sim 100$ - $1000$  days), which is much longer than the planetary orbital period ( $\sim 10$  hours). Moreover, the time scale necessary for the tidal effect between the central star and the planet to become dominant is much larger than either of them ( $> 10^4$  years).

Orbital averaging is the average with respect to the planetary true anomaly  $f$  ( $\int_0^{2\pi} df$ ), the angular parameter used to denote on what orbital phase the planet is located for a given time. Under this operation, the information on the planetary orbital phase and planetary momentum is lost, and correspondingly EOM for the planetary orbital motion ( $\dot{\mathbf{r}}$  and  $\dot{\mathbf{p}}$ ) are replaced by differential equations with respect to the orbital angular momentum and Lenz vector ( $\dot{\mathbf{L}}$  and  $\dot{\mathbf{e}}$ ). The EOM after averaging becomes.

$$\dot{\mathbf{S}}_i = \alpha_i (\hat{\mathbf{L}} \cdot \hat{\mathbf{S}}_i) (\hat{\mathbf{L}} \times \hat{\mathbf{S}}_i), \quad (\text{D.55})$$

$$\dot{\mathbf{L}} = -\dot{\mathbf{S}}_0 - \dot{\mathbf{S}}_1, \quad (\text{D.56})$$

$$\dot{\mathbf{e}} = \sum_{i=0,1} \frac{\alpha_i}{L} \left( (\hat{\mathbf{L}} \cdot \hat{\mathbf{S}}_i) (\hat{\mathbf{e}} \times \hat{\mathbf{S}}_i) + \frac{1}{2} (1 - 5(\hat{\mathbf{L}} \cdot \hat{\mathbf{S}}_i)^2) (\hat{\mathbf{e}} \times \hat{\mathbf{L}}) \right), \quad (\text{D.57})$$

where

$$\alpha_i = \frac{3GM_0M_1J_{2,i}R_i^2}{2a^3(1-e^2)^{3/2}}. \quad (\text{D.58})$$

## Appendix D.3 Equilibrium tidal theory and equations of motion

### Appendix D.3.1 Equilibrium tidal potential

The tidal potential  $U_T$  for the star and planet is written (Kaula 1964, Mignard 1979 and Correia et al. 2011):

$$U_T = \frac{G}{r^3} \sum_{i=0,1} k_{2,i} M_{(1-i)}^2 \frac{R_i^5}{r_i^3} P_2(\hat{\mathbf{r}} \cdot \hat{\mathbf{r}}'_i), \quad (\text{D.59})$$

where  $\mathbf{r}'$  is the position of the interacting body at a time delayed of  $\Delta t_i$ .  $k_{2,0}$  and  $k_{2,1}$  are the second Love numbers for the star and planet, respectively. As the rheology of stars and planets are not well known, the quantitative evaluation of  $\Delta t_i$  is very difficult. Therefore, we adopt here a model with constant  $\Delta t_i$  just for simplicity:

$$\mathbf{r}'_i = \mathbf{r} + \Delta t_i (\omega_i \hat{\mathbf{S}}_i \times \mathbf{r} - \dot{\mathbf{r}}). \quad (\text{D.60})$$

### Appendix D.3.2 Equations of motion for the tidal evolution

The equations of motion for the secular tidal evolution are given by making use of tidal potential (D.59) instead of rotational potential (D.44) in Hamilton's equations (D.50)-(D.52) and by orbital averaging:

$$\dot{\mathbf{S}}_i = K_i n \left[ f_4(e) \sqrt{1-e^2} \frac{\omega_i}{2n} (\hat{\mathbf{S}}_i - (\hat{\mathbf{L}} \cdot \hat{\mathbf{S}}_i) \hat{\mathbf{L}}) - f_1(e) \frac{\omega_i}{n} \hat{\mathbf{S}}_i + f_2(e) \hat{\mathbf{L}} + \frac{(\mathbf{e} \cdot \hat{\mathbf{S}}_i)(6+e^2)}{4(1-e^2)^{9/2}} \frac{\omega_i}{n} \mathbf{e} \right], \quad (\text{D.61})$$

$$\dot{\mathbf{L}} = -\dot{\mathbf{S}}_0 - \dot{\mathbf{S}}_1, \quad (\text{D.62})$$

$$\begin{aligned} \dot{\mathbf{e}} = & \sum_{i=0,1} \frac{15}{2} k_{2,i} n \left( \frac{M_{(1-i)}}{M_i} \right) \left( \frac{R_i}{a} \right)^5 f_4(e) (\hat{\mathbf{L}} \times \hat{\mathbf{e}}) \\ & - \sum_{i=0,1} \frac{K_i}{\beta a^2} \left[ f_4(e) \frac{\omega_i}{2n} (\hat{\mathbf{e}} \cdot \hat{\mathbf{S}}_i) \hat{\mathbf{L}} - \left( \frac{11}{2} f_4(e) (\hat{\mathbf{L}} \cdot \hat{\mathbf{S}}_i) \frac{\omega_i}{n} - 9f_5(e) \right) \mathbf{e} \right], \end{aligned} \quad (\text{D.63})$$

where

$$K_i = \Delta t_i \frac{3k_{2,i} G M_{(1-i)}^2 R_i^5}{a^6}, \quad (\text{D.64})$$

$$f_1(e) = \frac{1 + 3e^2 + 3e^4/8}{(1-e^2)^{9/2}}, \quad (\text{D.65})$$

$$f_2(e) = \frac{1 + 15e^2/2 + 45e^4/8 + 5e^6/16}{(1-e^2)^6}, \quad (\text{D.66})$$

$$f_3(e) = \frac{1 + 31e^2/2 + 255e^4/8 + 185e^6/16 + 25e^8/64}{(1-e^2)^{15/2}}, \quad (\text{D.67})$$

$$f_4(e) = \frac{1 + 3e^2/2 + e^4/8}{(1-e^2)^5}, \quad (\text{D.68})$$

and

$$f_5(e) = \frac{1 + 15e^2/4 + 15e^4/8 + 5e^6/64}{(1-e^2)^{13/2}}. \quad (\text{D.69})$$

## Appendix D.4 From angular momentum vectors to rotational/orbital parameters

Given angular momentum vectors and Lenz vector for a given time, they can be converted into the rotational/orbital parameters of the system ( $\omega_i$ :spin frequency of the star or planet,  $a$ :planetary orbital semi-major axis and  $e$ :planetary orbital eccentricity), which are required in right hand side in (D.61) ~ (D.63) when evaluating the angular momentum vectors at the next time step:

$$\omega_i = \frac{\mathbf{S}_i \cdot \hat{\mathbf{S}}_i}{\tilde{C}_i M_i R_i^2} \quad (\text{D.70})$$

$$a = \frac{|\mathbf{L}|^2}{\beta \mu^2 (1 - e^2)} \quad (\text{D.71})$$

$$e = |\mathbf{e}|, \quad (\text{D.72})$$

where  $\tilde{C}_i$  is the moment of inertia coefficient for the rotating body.

Table D.1: associated Legendre polynomials  $P_{nm}(\cos\theta)$  of degree  $n$ , order  $m$

|         | $m = 0$  | $m = 1$  | $m = 2$                                       | $m = 3$                      | $m = 4$           |
|---------|--|--|---|------------------------------|-------------------|
| $n = 0$ | 1  |  |   |                              |                   |
| $n = 1$ | $\cos\theta$                                       | $\sin\theta$   |   |                              |                   |
| $n = 2$ | $\frac{3}{2}\cos^2\theta - \frac{1}{2}$            | $3\cos\theta\sin\theta$                              | $3\sin^2\theta$                               |                              |                   |
| $n = 3$ | $\frac{5}{2}\cos^3\theta - \frac{3}{2}\cos\theta$  | $\sin\theta(\frac{15}{2}\cos^2\theta - \frac{3}{2})$ | $15\sin^2\theta\cos\theta$                    | $15\sin^3\theta$             |                   |
| $n = 4$ | $\frac{1}{8}(35\cos^4\theta - 30\cos^2\theta + 3)$ | $\frac{5}{2}\sin\theta(7\cos^3\theta - 3\cos\theta)$ | $\frac{15}{2}\sin^2\theta(7\cos^2\theta - 1)$ | $-105\sin^3\theta\cos\theta$ | $105\sin^4\theta$ |



# References

- Ahlers, J. P., Seubert, S. A., & Barnes, J. W. 2014, *ApJ*, 786, 131, Spin-Orbit Alignment for 110 Day Period KOI368.01 from Gravity Darkening
- Albrecht, S., Winn, J. N., Marcy, G. W., Howard, A. W., Isaacson, H., & Johnson, J. A. 2013, *ApJ*, 771, 11, Low Stellar Obliquities in Compact Multiplanet Systems
- Anderson, D. R., Hellier, C., Gillon, M., Triaud, A. H. M. J., Smalley, B., Hebb, L., Collier Cameron, A., Maxted, P. F. L., Queloz, D., West, R. G., Bentley, S. J., Enoch, B., Horne, K., Lister, T. A., Mayor, M., Parley, N. R., Pepe, F., Pollacco, D., Ségransan, D., Udry, S., & Wilson, D. M. 2010, *ApJ*, 709, 159, WASP-17b: An Ultra-Low Density Planet in a Probable Retrograde Orbit
- Armitage, P. J. 2010, *Astrophysics of Planet Formation*
- Baraffe, I., Chabrier, G., Allard, F., & Hauschildt, P. H. 1998, *A&A*, 337, 403, Evolutionary models for solar metallicity low-mass stars: mass-magnitude relationships and color-magnitude diagrams
- Barker, A. J. & Ogilvie, G. I. 2009, *MNRAS*, 395, 2268, On the tidal evolution of Hot Jupiters on inclined orbits
- Barnes, J. 2013, *Origins Of Intermediate-Period Planets From Spin-Orbit Alignment*, NASA Proposal #13-ADAP13-213
- Barnes, J. W. 2009, *ApJ*, 705, 683, Transit Lightcurves of Extrasolar Planets Orbiting Rapidly Rotating Stars
- Barnes, J. W., Linscott, E., & Shporer, A. 2011, *ApJS*, 197, 10, Measurement of the Spin-Orbit Misalignment of KOI-13.01 from Its Gravity-darkened Kepler Transit Lightcurve
- Barnes, J. W., van Eyken, J. C., Jackson, B. K., Ciardi, D. R., & Fortney, J. J. 2013, *ApJ*, 774, 53, Measurement of Spin-orbit Misalignment and Nodal Precession for the Planet around Pre-main-sequence Star PTF0 8-8695 from Gravity Darkening
- Bate, M. R., Lubow, S. H., Ogilvie, G. I., & Miller, K. A. 2003, *MNRAS*, 341, 213, Three-dimensional calculations of high- and low-mass planets embedded in protoplanetary discs

- Benomar, O., Masuda, K., Shibahashi, H., & Suto, Y. 2014, PASJ, Determination of three-dimensional spin-orbit angle with joint analysis of asteroseismology, transit lightcurve, and the Rossiter-McLaughlin effect: Cases of HAT-P-7 and Kepler-25
- Boué, G. & Laskar, J. 2006, *Icarus*, 185, 312, Precession of a planet with a satellite
- . 2009, *Icarus*, 201, 750, Spin axis evolution of two interacting bodies
- Briceño, C., Calvet, N., Hernández, J., Vivas, A. K., Hartmann, L., Downes, J. J., & Berlind, P. 2005, *AJ*, 129, 907, The CIDA Variability Survey of Orion OB1. I. The Low-Mass Population of Ori OB1a and 1b
- Brown, T. M., Charbonneau, D., Gilliland, R. L., Noyes, R. W., & Burrows, A. 2001, *ApJ*, 552, 699, Hubble Space Telescope Time-Series Photometry of the Transiting Planet of HD 209458
- Ciardi, D. R., Beichman, C. A., Carey, S. J., Crockett, C., Johns-Krull, C. M., Kane, S. R., McLane, J., Plavchan, P., Prato, L. A., Stauffer, J. R., van Belle, G., Van Eyken, J. C., & von Braun, K. 2014, in American Astronomical Society Meeting Abstracts, Vol. 223, American Astronomical Society Meeting Abstracts #223, 430.03
- Claret, A., Diaz-Cordoves, J., & Gimenez, A. 1995, *A&AS*, 114, 247, Linear and non-linear limb-darkening coefficients for the photometric bands R I J H K.
- Cochran, W. D., Hatzes, A. P., Butler, R. P., & Marcy, G. W. 1997, *ApJ*, 483, 457, The Discovery of a Planetary Companion to 16 Cygni B
- Correia, A. C. M., Laskar, J., Farago, F., & Boué, G. 2011, *Celestial Mechanics and Dynamical Astronomy*, 111, 105, Tidal evolution of hierarchical and inclined systems
- Dawson, R. I. 2014, *ApJ*, 790, L31, On the Tidal Origin of Hot Jupiter Stellar Obliquity Trends
- Dermott, S. F. 1979a, *Icarus*, 37, 575, Shapes and gravitational moments of satellites and asteroids
- . 1979b, *Icarus*, 37, 310, Tidal dissipation in the solid cores of the major planets
- Duffell, P. C. & MacFadyen, A. I. 2013, *ApJ*, 769, 41, Gap Opening by Extremely Low-mass Planets in a Viscous Disk
- Eggleton, P. P., Kiseleva, L. G., & Hut, P. 1998, *ApJ*, 499, 853, The Equilibrium Tide Model for Tidal Friction
- Goldstein, H., Poole, C., & Safko, J. 2002, *Classical mechanics*
- Gray, D. F. 2008, *The Observation and Analysis of Stellar Photospheres*

- 
- Hayashi, C., Nakazawa, K., & Nakagawa, Y. 1985, in *Protostars and Planets II*, ed. D. C. Black & M. S. Matthews, 1100–1153
- Hirano, T., Narita, N., Sato, B., Takahashi, Y. H., Masuda, K., Takeda, Y., Aoki, W., Tamura, M., & Suto, Y. 2012, *ApJ*, 759, L36, Planet-Planet Eclipse and the Rossiter-McLaughlin Effect of a Multiple Transiting System: Joint Analysis of the Subaru Spectroscopy and the Kepler Photometry
- Hirano, T., Narita, N., Shporer, A., Sato, B., Aoki, W., & Tamura, M. 2011, *PASJ*, 63, 531, A Possible Tilted Orbit of the Super-Neptune HAT-P-11b
- Howard, A. W. 2013, *Science*, 340, 572, Observed Properties of Extrasolar Planets
- Huber, D., Carter, J. A., Barbieri, M., Miglio, A., Deck, K. M., Fabrycky, D. C., Montet, B. T., Buchhave, L. A., Chaplin, W. J., Hekker, S., Montalbán, J., Sanchis-Ojeda, R., Basu, S., Bedding, T. R., Campante, T. L., Christensen-Dalsgaard, J., Elsworth, Y. P., Stello, D., Arentoft, T., Ford, E. B., Gilliland, R. L., Handberg, R., Howard, A. W., Isaacson, H., Johnson, J. A., Karoff, C., Kawaler, S. D., Kjeldsen, H., Latham, D. W., Lund, M. N., Lundkvist, M., Marcy, G. W., Metcalfe, T. S., Silva Aguirre, V., & Winn, J. N. 2013, *Science*, 342, 331, Stellar Spin-Orbit Misalignment in a Multiplanet System
- Hut, P. 1981, *A&A*, 99, 126, Tidal evolution in close binary systems
- Ida, S. & Lin, D. N. C. 2004, *ApJ*, 604, 388, Toward a Deterministic Model of Planetary Formation. I. A Desert in the Mass and Semimajor Axis Distributions of Extrasolar Planets
- Ikoma, M., Nakazawa, K., & Emori, H. 2000, *ApJ*, 537, 1013, Formation of Giant Planets: Dependences on Core Accretion Rate and Grain Opacity
- Kaula, W. M. 1964, *Reviews of Geophysics and Space Physics*, 2, 661, Tidal Dissipation by Solid Friction and the Resulting Orbital Evolution
- Klahr, H. & Kley, W. 2006, *A&A*, 445, 747, 3D-radiation hydro simulations of disk-planet interactions. I. Numerical algorithm and test cases
- Lai, D. 2012, *MNRAS*, 423, 486, Tidal dissipation in planet-hosting stars: damping of spin-orbit misalignment and survival of hot Jupiters
- Lin, D. N. C., Bodenheimer, P., & Richardson, D. C. 1996, *Nature*, 380, 606, Orbital migration of the planetary companion of 51 Pegasi to its present location
- Love, A. E. H. 1909, *Royal Society of London Proceedings Series A*, 82, 73, The Yielding of the Earth to Disturbing Forces
- Maeder, A. 1999, *A&A*, 347, 185, Stellar evolution with rotation IV: von Zeipel's theorem and anisotropic losses of mass and angular momentum

- . 2009, *Physics, Formation and Evolution of Rotating Stars*
- Mandel, K. & Agol, E. 2002, *ApJ*, 580, L171, Analytic Light Curves for Planetary Transit Searches
- Marcy, G. W. & Butler, R. P. 1996, *ApJ*, 464, L147, A Planetary Companion to 70 Virginis
- Mayor, M. & Queloz, D. 1995, *Nature*, 378, 355, A Jupiter-mass companion to a solar-type star
- McLaughlin, D. B. 1924, *ApJ*, 60, 22, Some results of a spectrographic study of the Algol system.
- Mignard, F. 1979, *Moon and Planets*, 20, 301, The evolution of the lunar orbit revisited. I
- Murray, C. D. & Correia, A. C. M. *Keplerian Orbits and Dynamics of Exoplanets*, ed. S. Seager, 15–23
- Murray, C. D. & Dermott, S. F. 1999, *Solar system dynamics*
- Nagasawa, M. & Ida, S. 2011, *ApJ*, 742, 72, Orbital Distributions of Close-in Planets and Distant Planets Formed by Scattering and Dynamical Tides
- Narita, N., Sato, B., Hirano, T., & Tamura, M. 2009, *PASJ*, 61, L35, First Evidence of a Retrograde Orbit of a Transiting Exoplanet HAT-P-7b
- Philippov, A. A. & Rafikov, R. R. 2013, *ApJ*, 768, 112, Analysis of Spin-Orbit Misalignment in the Eclipsing Binary DI Herculis
- Queloz, D., Eggenberger, A., Mayor, M., Perrier, C., Beuzit, J. L., Naef, D., Sivan, J. P., & Udry, S. 2000, *A&A*, 359, L13, Detection of a spectroscopic transit by the planet orbiting the star HD209458
- Rogers, T. M. & Lin, D. N. C. 2013, *ApJ*, 769, L10, On the Tidal Dissipation of Obliquity
- Rossiter, R. A. 1924, *ApJ*, 60, 15, On the detection of an effect of rotation during eclipse in the velocity of the brighter component of beta Lyrae, and on the constancy of velocity of this system.
- Siess, L., Dufour, E., & Forestini, M. 2000, *A&A*, 358, 593, An internet server for pre-main sequence tracks of low- and intermediate-mass stars
- Sing, D. K. 2010, *A&A*, 510, A21, Stellar limb-darkening coefficients for CoRot and Kepler
- Snellen, I. A. G., Brandl, B. R., de Kok, R. J., Brogi, M., Birkby, J., & Schwarz, H. 2014, *Nature*, 509, 63, Fast spin of the young extrasolar planet  $\beta$  Pictoris b

- Szabó, G. M., Pál, A., Derekas, A., Simon, A. E., Szalai, T., & Kiss, L. L. 2012, *MNRAS*, 421, L122, Spin-orbit resonance, transit duration variation and possible secular perturbations in KOI-13
- van Eyken, J. C., Ciardi, D. R., von Braun, K., Kane, S. R., Plavchan, P., Bender, C. F., Brown, T. M., Crepp, J. R., Fulton, B. J., Howard, A. W., Howell, S. B., Mahadevan, S., Marcy, G. W., Shporer, A., Szkody, P., Akeson, R. L., Beichman, C. A., Boden, A. F., Gelino, D. M., Hoard, D. W., Ramírez, S. V., Rebull, L. M., Stauffer, J. R., Bloom, J. S., Cenko, S. B., Kasliwal, M. M., Kulkarni, S. R., Law, N. M., Nugent, P. E., Ofek, E. O., Poznanski, D., Quimby, R. M., Walters, R., Grillmair, C. J., Laher, R., Levitan, D. B., Sesar, B., & Surace, J. A. 2012, *ApJ*, 755, 42, The PTF Orion Project: A Possible Planet Transiting a T-Tauri Star
- von Zeipel, H. 1924, *MNRAS*, 84, 665, The radiative equilibrium of a rotating system of gaseous masses
- Walkowicz, L. M. & Basri, G. S. 2013, *MNRAS*, 436, 1883, Rotation periods, variability properties and ages for Kepler exoplanet candidate host stars
- Winn, J. N. 2010, ArXiv e-prints, Transits and Occultations
- Winn, J. N., Fabrycky, D., Albrecht, S., & Johnson, J. A. 2010, *ApJ*, 718, L145, Hot Stars with Hot Jupiters Have High Obliquities
- Winn, J. N., Johnson, J. A., Albrecht, S., Howard, A. W., Marcy, G. W., Crossfield, I. J., & Holman, M. J. 2009, *ApJ*, 703, L99, HAT-P-7: A Retrograde or Polar Orbit, and a Third Body
- Winn, J. N., Noyes, R. W., Holman, M. J., Charbonneau, D., Ohta, Y., Taruya, A., Suto, Y., Narita, N., Turner, E. L., Johnson, J. A., Marcy, G. W., Butler, R. P., & Vogt, S. S. 2005, *ApJ*, 631, 1215, Measurement of Spin-Orbit Alignment in an Extrasolar Planetary System
- Wu, Y. & Murray, N. 2003, *ApJ*, 589, 605, Planet Migration and Binary Companions: The Case of HD 80606b
- Xue, Y., Suto, Y., Taruya, A., Hirano, T., Fujii, Y., & Masuda, K. 2014, *ApJ*, 784, 66, Tidal Evolution of the Spin-Orbit Angle in Exoplanetary Systems
- Zharkov, V. N. & Trubitsyn, V. P. 1974, *Icarus*, 21, 152, Determination of the equation of state of the molecular envelopes of Jupiter and Saturn from their gravitational moments
- Zhou, G. & Huang, C. X. 2013, *ApJ*, 776, L35, A Highly Inclined Orbit for the 110 Day Period M-dwarf Companion KOI-368.01
- Zhu, W., Huang, C. X., Zhou, G., & Lin, D. N. C. 2014, *ApJ*, 796, 67, Constraining the Oblateness of Kepler Planets